

---

Wayne State University Dissertations


---

January 2022

## Deconstructing Brown Adipocyte Neogenesis In Brown And White Adipose Tissue

Rayanne Burl  
*Wayne State University*

Follow this and additional works at: [https://digitalcommons.wayne.edu/oa\\_dissertations](https://digitalcommons.wayne.edu/oa_dissertations)

 Part of the [Cell Biology Commons](#), and the [Molecular Biology Commons](#)

---

### Recommended Citation

Burl, Rayanne, "Deconstructing Brown Adipocyte Neogenesis In Brown And White Adipose Tissue" (2022).  
*Wayne State University Dissertations*. 3663.  
[https://digitalcommons.wayne.edu/oa\\_dissertations/3663](https://digitalcommons.wayne.edu/oa_dissertations/3663)

This Open Access Dissertation is brought to you for free and open access by DigitalCommons@WayneState. It has been accepted for inclusion in Wayne State University Dissertations by an authorized administrator of DigitalCommons@WayneState.

**DECONSTRUCTING BROWN ADIPOCYTE NEOGENESIS IN BROWN AND WHITE  
ADIPOSE TISSUE**

by

**RAYANNE B. BURL**

**DISSERTATION**

Submitted to the Graduate School

of Wayne State University,

Detroit, Michigan

in partial fulfillment of the requirements

for the degree of

**DOCTOR OF PHILOSOPHY**

2022

**MAJOR: MOLECULAR GENETICS &  
GENOMICS**

Approved by:

---

Advisor

---

Date

---

---

---

**© COPYRIGHT BY**

**RAYANNE B. BURL**

**2022**

**All Rights Reserved**

## **DEDICATION**

I would like to dedicate this work to all current and future graduate students. You are my acquaintances, friends, and colleagues. I see you. I support you. And I understand if you recognize that this process isn't right for you. But if you decide to persevere, pull your strength from your friends and family. It worked for me.

I would also like to dedicate this to Lillian Marie Burl. Lily was a beautiful person, inside and out, and she will be greatly missed.

## ACKNOWLEDGEMENTS

It gives me great pleasure to acknowledge the support and guidance of many people during the course of my dissertation. First, I would like to thank my mentor, Dr. James Granneman, for his guidance throughout my dissertation work. He is truly a great scientist, and I hope emulate his drive and enthusiasm for research. Thank you to the members of my dissertation committee, Dr. Todd Leff, Dr. Carey Lumeng, and Dr. Roger Pique-Regi for their guidance and suggestions that helped me move this project forward. I would especially like to thank Dr. Pique-Regi for his help developing my computational skills. It was an honor to learn from someone who is so skilled and knowledgeable in an area I was just starting out in, and I'm excited to see where these skills will take me. Along with Dr. Pique-Regi, I would like to thank Dr. Francesca Luca and Adnan Alzazi for their assistance with all the sequencing involved in this work. I would also like to acknowledge my funding through my F31 fellowship from the NIDDK and the OVPR Genomics Voucher Program.

I would like to thank my colleague, Dr. Beth Rondini, for setting the example for hard work, technical skills, and lab organization. She took the time to thoroughly train me, and always had a typed protocol to share. I would also like to acknowledge Dr. Hong-Guang Wei, who joined the lab at a critical moment when I needed a histology expert, and was able to share her knowledge and friendship. Thank you to all the other current and former members of the Granneman Lab who I've worked with: Alex Yang, Emilio Mottillo, Anelia Petkova, Li Zhou, Ljiljana Mladenovic, Heidi Zhang, and Matt Sanders. I would also like to thank Dr. Nardhy Gomez-Lopez and Dr. Yi Xu for their assistance with our flow

cytometry studies, and Dr. Katherine Gurdziel and the Wayne State Genome Sciences Core for their work on library preparation and sequencing.

I would like to acknowledge my family, Ron Burl, Rhonda Burl, Ryan Burl, and Marjorie Carter for your love, encouragement, and understanding. In the past 7 years, we have gone through some difficult things as a family. However, we made it through and I wouldn't be here today without all of your support. To my partner, Dr. Nick Sweda, thank you for all the work you have put in to our relationship. It hasn't always been easy having an equally career-driven partner, but we've grown together and I'm excited to see where the future takes us. And to my additional family, Stephen Sweda, Cheryl Tonkovich, and Matt Sweda, I've been so lucky to have such a caring local support system that I could rely on.

Finally, to the amazing friends I've met these past seven years, I am so lucky to have all of you in my life. First, to the family I found in graduate school, Dr. Stephanie Gladysck, Dr. Hasini Kalpage, Dr. Emily Lowther, and Dr. Sophia Chaudhry, thank you. Without you, I probably would not have made it through my first semester. The PhD process can be arduous and disheartening, but being able to lean on such a brilliant, thoughtful, and strong group of women helped me through my most difficult moments. It was an honor to watch all of you earn your degrees. Thank you to Erica MacDonald, Maureen Roessel, and Ellen Lynch for the laughs and friendship. There is no group of friends I look more forward to seeing. Thank you to Mitch Marks and Tara Reid came into my life when I needed some fun, caring, compassionate people. We will remain friends forever. And thank you to all the other friends who made my time here in Detroit so special. I hope all of you know how much you mean to me. Thank you.

## TABLE OF CONTENTS

Dedication .....	ii
Acknowledgements .....	iii
List of Tables .....	x
List of Figures .....	xi
List of Abbreviations .....	xiv
Chapter 1. Introduction .....	1
1.1 Type 2 diabetes and adipose tissue .....	1
1.2 White and brown adipose tissue .....	2
1.3 Cellular plasticity of adipose tissue .....	4
1.4 Brown adipogenesis in adult adipose tissue .....	5
1.4.1 Brown adipogenesis in visceral WAT .....	5
1.4.2 Brown adipogenesis in subcutaneous WAT .....	6
1.4.3 Brown adipogenesis in BAT .....	6
1.5 Adipocyte progenitors .....	7
1.6 Beta-adrenergic signaling in adipose tissue .....	8
1.7 Adipose tissue immune cells .....	9
1.8. Hypothesis and aims of the project .....	10
Chapter 2. Methods and Materials .....	12
2.1 Experimental model and subject detail .....	12
2.2 Tissue processing and immunohistochemistry .....	15
2.3 Single-molecule fluorescence <i>in situ</i> hybridization .....	16
2.4 Microscopy and image analysis .....	17

2.5 Isolation of peritoneal macrophages and white blood cells from ITGAM-DTR mice and controls .....	18
2.6 RNA isolation and quantitative PCR (qPCR) .....	19
2.6.1 <i>Adrb1</i> KO iBAT RNA isolation and qPCR .....	19
2.6.2 <i>Ccr2<sup>gfp/gfp</sup></i> iBAT RNA isolation and qPCR .....	20
2.6.3 ITGAM-DTR RNA isolation and qPCR .....	21
2.6.4 Direct injection of liposomes, iBAT RNA isolation and qPCR .....	22
2.7 ITGAM-DTR genotyping and sequencing PCR product .....	23
2.8 Fluorescence-activated cell sorting (FACS) .....	24
2.8.1 FACS isolation and RNA library prep of PDGFRA+CD44+ cells from mouse eWAT .....	24
2.8.2 FACS analysis to test CD11b+ cell knockdown in ITGAM-DTR mice with DT injection .....	25
2.9 RNA-seq library preparation and sequencing .....	25
2.9.1 RNA-seq library preparation and sequencing of FACS-sorted eWAT PDGFRA+ cells .....	25
2.9.2 RNA-seq library preparation and sequencing of iBAT from cold exposure time course .....	26
2.10 Isolation of stromal vascular cell from mouse adipose tissue .....	27
2.10.1 Isolation of stromal vascular cells from mouse eWAT and iWAT .....	27
2.10.2 Isolation of stromal vascular cells from mouse iBAT .....	29
2.10.3 Protocol for comparing digestion methods of mouse iBAT .....	30
2.11 Magnetic activated cell sorting into lineage marker positive (Lin+) and lineage marker negative (Lin-) cell fractions .....	31
2.12 Single-cell RNA-sequencing .....	32
2.12.1 Single-cell RNA-sequencing of eWAT and iWAT cells .....	32



2.13.2 Single-cell RNA-sequencing of iBAT cells .....	34
2.13.3 Single-cell RNA-sequencing and analysis of iBAT libraries testing alternative digestion methods .....	36
2.14 Ligand-receptor Analysis .....	37
2.15 Analysis and integration of Shamsi, <i>et al.</i> data .....	38
2.16 Quantification and Statistical Analysis .....	38
2.17 Data and Software Availability .....	39
Chapter 3. Deconstructing brown adipogenesis induced by $\beta$ 3-adrenergic receptor activation in white adipose tissue .....	40
3.1 RNA-Seq analysis of FACS-isolated progenitors suggests a complex adipogenic trajectory .....	40
3.2 scRNA-seq deconvolves progenitor heterogeneity and defines an adipogenic trajectory .....	42
3.3 scRNA-seq analysis demonstrates dynamic regulation of macrophage populations and suggests functional interactions with activated progenitors .....	54
3.4 ADRB3 activation for three days produces minimal de novo adipogenesis from stromal cells in inguinal WAT .....	58
3.5 Similarities and differences between ASC of eWAT and iWAT .....	60
Chapter 4. Deconstructing cold-induced neogenesis in classic brown adipose tissue ...	63
4.1 RNA-seq analysis of mouse iBAT during cold exposure time course reveals activation of immune cells that correlates with proliferation .....	63
4.2 iBAT scRNA-seq of total stromal cells identifies multiple adipocyte stromal cell subtypes .....	66
4.3 iBAT scRNA-seq identifies cells undergoing cold-induced adipogenic differentiation .....	69
4.4 Localizing ASC subtypes and adipogenic niches within the tissue microenvironment .....	70
4.5 Mapping an adipogenic trajectory <i>in situ</i> .....	72

4.6 ASC proliferation/differentiation is triggered indirectly via adrenergic activation of BAs .....	75
4.7 Cold exposure recruits macrophages and dendritic cells in iBAT .....	79
4.8 Recruitment of cold-induced immune cells predicts the magnitude of progenitor proliferation and differentiation across experimental conditions .....	83
4.9 Macrophage and dendritic cells interact with proliferating ASCs in known sites of neogenesis .....	85
4.10 Adipogenic niches are dynamic .....	87
4.11 Investigating potential cell-cell communication in the adipogenic niche .....	90
Chapter 5. Effect of tissue digestion method on single-cell analysis .....	93
5.1 Introduction .....	93
5.2 Integration of iBAT scRNA-seq data with the Shamsi, <i>et al.</i> cold exposure iBAT single-cell data .....	95
5.3 iBAT digestion method alters proportions of cells profiled with scRNA-seq .....	100
Chapter 6. Manipulation of immune cell types in brown adipose tissue .....	104
6.1 Introduction .....	104
6.2 Ccr2 KO does not affect proliferation or immune cell recruitment .....	104
6.3 Diphtheria toxin receptor model system was ineffective in knocking down immune cell population <i>in vivo</i> .....	106
6.4 Direct injection of liposomes into mouse iBAT recruited GPNMB+ macrophages and dendritic cells .....	109
Chapter 7. Discussion .....	114
7.1 Single-cell analysis of eWAT and iWAT discussion .....	114
7.2 Deconstructing cold-induced iBAT neogenesis discussion .....	116
7.3 Effect of digestion method on iBAT single-cell analysis discussion .....	124
7.4 Manipulation of iBAT immune cells <i>in vivo</i> discussion .....	126

Chapter 8. Future Directions .....	129
References .....	132
Abstract .....	155
Autobiographical Statement .....	157

## LIST OF TABLES

Table 1. Analysis of $\beta$ -adrenergic receptor manipulation by scRNA-seq .....	77
---	----

## LIST OF FIGURES

Figure 1. Schematic diagram of sing-cell library generation and processing .....	28
Figure 2. RNA-seq analysis of FACS-isolated PDGFRA+ cells from eWAT of control and CL-treated mice .....	41
Figure 3. Single-Cell RNA-Seq Reveals <u>ASC</u> Heterogeneity in Mouse eWAT .....	43
Figure 4. scRNA-Seq of Mouse eWAT Maps an Adipogenic Differentiation Trajectory during CL Treatment .....	45
Figure 5. Pseudotime analysis of proliferating/differentiating cells .....	47
Figure 6. CL treatment upregulates expression of genes involved in cell migration, proliferation, and ECM remodeling in eWAT adipocyte stem cells .....	49
Figure 7. scRNA-Seq Analysis of Aggregated eWAT Lin+ and Lin- Cells from Control and CL-Treated Mice .....	51
Figure 8. Expression patterns of adipogenic/proliferation genes in ASC from aggregate Lin+ and Lin- fractions identifies proliferating and differentiating ASCs .....	52
Figure 9. Correspondence of DEGs identified by bulk RNA-sequencing of FACS sorted PDGFRA+CD44+ cells to scRNA-seq .....	53
Figure 10. scRNA-Seq Analysis of Lin+ eWAT Stromal Cells of Control and CL-Treated Mice .....	55
Figure 11. Expression of M2 macrophage markers in scRNA-seq .....	57
Figure 12. scRNA-Seq of ASCs from iWAT of Control and CL-Treated Mice .....	59
Figure 13. Comparison of ASCs from eWAT and iWAT .....	61
Figure 14. Whole tissue RNA-sequencing analysis reveals proliferation correlates with immune cell recruitment during cold exposure .....	64
Figure 15. scRNA-seq reveals ASC heterogeneity and maps adipogenic trajectories in mouse iBAT .....	65
Figure 16. scRNA-seq analysis of Lin- cells from iBAT of control and cold-exposed mice .....	67
Figure 17. <i>Pdgfra</i> + ASC subtypes occupy distinct areas of the tissue .....	71

Figure 18. smFISH maps adipogenic trajectories and supports ASC1 as the direct precursors of new BA .....73

Figure 19. Immunohistochemistry identified newly differentiating ASCs that are NNAT and PLIN1 positive .....74

Figure 20. *Adrb1* is dispensable for cold-induced brown adipocyte neogenesis .....76

Figure 21. Role of ADRB subtypes in cold-induced iBAT neogenesis .....78

Figure 22. scRNA-seq analysis of Lin+ immune cells from iBAT of control or cold-exposed mice .....80

Figure 23. Analysis gene expression markers from single-cell analysis of iBAT dendritic cells and lipid-handling macrophages .....81

Figure 24. Cold-induced iBAT neogenesis involves close interaction between immune cells and proliferating ASCs .....84

Figure 25. Macrophages surround cellular vacancies containing lipid remnants .....86

Figure 26. ASCs and immune cells comprise a dynamic cellular niche .....87

Figure 27. Flash-labeling of proliferating cells and proximity of MHCII+ dendritic cells ..89

Figure 28. scRNA-seq data reveal potential ligand-receptor pairs for ASC-immune cell crosstalk .....91

Figure 29. Analysis and subsetting of Shamsi, *et al.* mouse iBAT scRNA-seq data .....94

Figure 30. Integration of Burl, *et al.* Linpos iBAT scRNA-seq data and Shamsi, *et al.* immune cells .....96

Figure 31. Integration of Burl, *et al.* Linneg iBAT scRNA-seq data and Shamsi, *et al.* non-immune cells .....98

Figure 32. iBAT digestion method affects proportions of SVF cells profiled with scRNA-seq .....101

Figure 33. Different iBAT digestion methods capture similar proportions of immune cells .....102

Figure 34. Different iBAT digestion methods retain cold-activated ASCs and cells undergoing adipogenic differentiation .....103

Figure 35. *Ccr2* KO does not affect cold-induced immune cell recruitment or proliferation .....105

Figure 36. ITGAM-DTR mouse model was unsuccessful in knocking down CD11b+ cells .....107

Figure 37. Quantitative PCR demonstrates that liposome direct injection into mouse iBAT recruits immune cells .....110

Figure 38. Direct-injection of liposomes causes a foreign body reaction that recruits immune cells and induces proliferation .....112

Figure 39. Model summary of cold-induced iBAT neogenesis .....118

## LIST OF ABBREVIATIONS

ADRB1,  $\beta$ 1-adrenergic receptor

ADRB3,  $\beta$ 3-adrenergic receptor

ASC, adipose tissue stromal cells

BA, brown adipocyte

BAT, brown adipose tissue

Blym, B lymphocyte

cDC1, conventional dendritic cell type 1

CL, CL316,243

DEGs, differentially expressed genes

DEND, dendritic cell

Diff., differentiating cell

ECM, extracellular matrix

EDTA, ethylenediaminetetraacetic acid

EdU, 5-ethynyl-2'-deoxyuridine

eWAT, epididymal white adipose tissue



FACS, fluorescence-activated cell sorting

FB, fibroblast

FBS, fetal bovine serum

FC, fold-change

FF-BSA, fatty-acid free bovine serum albumin

GEMs, gel beads in emulsion

GO, gene ontology

HBSS, Hanks' balanced salt's solution

HEPES, 4-(2-hydroxyethyl)-1-piperazineethanesulfonic acid

iBAT, interscapular brown adipose tissue

iWAT, inguinal white adipose tissue

KO, knockout

Lin+, lineage marker positive

Lin-, lineage marker negative

MAC, macrophage

MACS, magnetic cell separation

moDC, monocyte-derived dendritic cell

NBF, neutral buffered formalin

NE, norepinephrine

NEUT, neutrophil

NKT, natural killer T-cell

NN, nearest neighbors

PBS, phosphate buffered saline

PC, principal component

PER, Primer Exchange Reaction

Pro., proliferating cell

Prolif/Diff, proliferating/differentiating

RBC, red blood cell

RET, reticulocyte

scRNA-seq, single-cell RNA sequencing

RT, room temperature

smFISH, single molecule fluorescence *in situ* hybridization

SVC, stromal vascular cell

SVF, stromal vascular fraction

t-SNE, t-Distributed Stochastic Neighbor Embedding

Tlym, T lymphocyte

WAT, white adipose tissue

WT, wild type

VEC, vascular endothelial cells

VSMC, vascular smooth muscle cells

## Chapter 1. Introduction

### 1.1 Type 2 diabetes and adipose tissue

The global prevalence of Type 2 diabetes (T2D) has increased drastically over the past thirty years [1, 2]. In 2016, approximately 8.6% of the United States population had T2D [1, 2]. This is compared to 2.8% in 1986. Diabetes is one of the top 10 causes of death globally [2]. The rise in T2D has been paralleled with a rise in obesity, which disrupts the metabolic, endocrine, and immune functions of adipose tissue [3]. The majority of individuals with T2D are obese, highlighting increased amounts of adipose tissue as an important risk factor for T2D. The link between obesity and diabetes is undeniable, and recent work demonstrates that systemic metabolic status can be improved by therapeutic adipose tissue remodeling [3-6].

Adipose tissue typically functions as the body's energy buffer, storing excess energy in the form of triglyceride and mobilizing energy as free fatty acids in times of energy demand. Fatty acids can be toxic, so their storage and release is tightly regulated by integrated endocrine and metabolic mechanisms [7-9]. The buffering capacity of adipose tissue can be exceeded with chronic overnutrition, which causes aberrant lipid accumulation in other tissues. This leads to impaired insulin production and insulin action [7-9]. Thus, increasing the ability of adipose tissue to store or oxidize excess lipid would be beneficial to whole body metabolism.

Cellular remodeling of adipose tissue has proven an effective way to mitigate these obesity-related diseases. Metabolic status can be improved therapeutically by increasing the anabolic functions of adipose tissue, as evidenced by the class of drug thiazolidinediones [10-13]. Thiazolidinediones are a class of FDA approved drugs that

were used for the management of T2D that work as ligands for the transcription factor peroxisome proliferator-activated receptor gamma (PPAR $\gamma$ ). PPAR $\gamma$  activation in adipose tissue leads to the transcription of genes involved in regulating cell metabolism and adipogenesis. This includes recruiting new adipocytes from progenitor cells, increasing the storage capacity of existing adipocytes, and improving the mixture of adipokines released from adipose tissue [10-13].

Adipose tissue remodeling through expanding populations of thermogenic adipocytes, such as brown and beige adipocytes, also improves metabolic status. Genetic and pharmacological activation of protein kinase A (PKA) signaling expands populations of brown/beige adipocytes, which exhibit elevated levels of thermogenesis and fat oxidation [14-18]. Recruiting brown/beige adipocytes in mammals has a beneficial effect on energy homeostasis and insulin sensitivity [19-22], although the molecular and cellular bases *in vivo* and their dynamics remain poorly understood. This work is focused on adipose tissue remodeling through recruiting catabolic adipocytes (brown/beige) in white and brown adipose tissue depots.

## **1.2 White and brown adipose tissue**

In mammals, two functionally and morphologically distinct types of adipose tissue exist: white and brown adipose tissue. The primary function of white adipose tissue (WAT) is to store excess calories in the form of triglycerides in lipid droplets, which can be mobilized during periods of fasting for use throughout the body [3, 23]. WAT is generally classified as either subcutaneous or visceral, based on the location of the depot. Visceral adipose tissue is associated with higher risk of metabolic disease, whereas subcutaneous adipose tissue seems to play a protective role [24-28]. WAT is comprised of unilocular

adipocytes, having one large lipid droplet with a peripheral nucleus and little cytoplasm [29-32].

In contrast, brown adipose tissue (BAT) is a specialized organ that is the dominant site of non-shivering thermogenesis in neonate mammals to regulate body temperature [4, 33, 34]. Because of its thermogenic function, BAT can be regulated by the thermoregulatory arm of the nervous system, and is therefore tied to innervation and release of norepinephrine (NE) [35-37]. The thermogenic function of brown adipose tissue is due to the protein uncoupling protein 1 (UCP1), which uncouples the electron transport chain to generate heat [38, 39]. UCP1 is highly expressed in thermogenic brown adipocytes (BAs), and is the characteristic marker for this cell type. BAs are multilocular, with many small lipid droplets, and have a high number of mitochondria, giving the tissue its characteristic brown color [29-32].

While essential for heat production in neonates, adult humans also have metabolically active BAT that can be measured by PET imaging [40, 41]. Importantly, adult BAT mass and function are associated with a healthier metabolic profile in both rodents and humans [42-44]. Although the direct mechanisms have not been fully elucidated, BAT abundance and activity is associated with higher energy expenditure, altered secretion of hormones, and reduced visceral fat mass [19, 37, 43, 45-48]. However, the mass of brown adipose tissue in humans is highly variable (most humans have < 50g), and the thermogenic activity, directly measured by O15 PET, is low [40, 41]. Thus, in order to expand the metabolic and hormonal effect of BAT for metabolic improvement in humans, it is necessary to identify the source of new brown adipocytes, and determine how they are

recruited and maintained in adult mammals so that these cell types might be expanded *in vivo*.

### **1.3 Cellular plasticity of adipose tissue**

Adipose tissue is a highly plastic organ, able to change cell size, morphology, and number in response to different environmental stimuli or biological processes. This is essential to managing energy homeostasis. For example, in an obesogenic environment, WAT can undergo hypertrophy (increase adipocyte size) or hyperplasia (increase adipocyte number) to increase its energy storing capacity. This can also be expanded using the previously mentioned PPAR $\gamma$  agonists [12]. In addition, WAT has the capacity to transition between white and brown phenotypes, changing the metabolism and function of the tissue [29-32]. Classic WAT depots can adopt a more brown-like phenotype under certain conditions, like cold exposure or  $\beta$ -adrenergic receptor stimulation. The  $\beta$ 3-adrenergic receptor is expressed primarily in adipose tissue in mature adipocytes, and treatment in mammals with the  $\beta$ 3-agonist CL316,243 (CL) causes WAT to adopt a brown-like composition: cells that are UCP1+, multilocular, with increased mitochondria [14, 30, 49-53]. Brown-like adipocytes in WAT are sometimes referred to as beige or brite (brown in white) adipocytes.

Because BAT is a thermogenic organ, the most potent physiological mechanism for expanding BAT *in vivo* is cold exposure, which stimulates sympathetic release of NE to promote expansion of the tissue [33, 37, 54-56]. Cold-induced neogenesis involves transient activation of stromal cell types that results in BA hyperplasia. Alternatively in BAT, multiple factors can cause BAT to “whiten”, adopting more WAT characteristics. These factors include aging, obesity, and high ambient temperature [57]. BA

differentiation has been studied extensively *in vitro*, using preadipocyte cell lines [58-61]. However, not much is known about signals that govern this process *in vivo*. It is the goal of my research to study how new BAs are formed *in vivo* by studying both WAT browning and BAT neogenesis.

## **1.4 Brown adipogenesis in adult adipose tissue**

As established, certain stimuli (cold or  $\beta$ 3-adrenergic activation) can lead to the appearance of new BAs in WAT and BAT. The origin of new BAs is a heavily investigated topic of research, and can differ by adipose tissue depot.

### **1.4.1 Brown adipogenesis in visceral WAT**

In visceral WAT, such as the epididymal WAT (eWAT) in male mice, ADRB3 activation by CL triggers *de novo* adipogenesis from progenitors that express the surface marker platelet-derived growth factor receptor alpha (PDGFRA) positive progenitor cells [50, 51]. This adipogenesis occurs rapidly, taking place 3-4 days after continuous CL infusion, and occurs in a defined tissue niche (i.e., a “crown-like structure”) which includes close interactions among immune cell types [50, 51]. ADRB3 activation triggers the death of mature white adipocytes, which in turn recruits phagocytic macrophage subpopulations to clear the dead/dying cells through the process of efferocytosis [50]. Recruited macrophages express high levels of osteopontin (OPN), which attracts PDGFRA+ progenitors to the site through its receptor CD44. Progenitors proliferate with the phagocytic macrophages at the site of efferocytosis (dead cell removal). Once the dead cell is cleared, the macrophages regress and a cluster of new brown adipocytes appears at the site where the dying cell once was [50]. This process is orchestrated by the sequential activation of multiple tissue subpopulations.



### 1.4.2 Brown adipogenesis in subcutaneous WAT

In subcutaneous WAT, such as inguinal WAT (iWAT), new BAs are derived from existing adipocytes that appear white under basal conditions, yet can adopt a brown phenotype through the process of transdifferentiation [52, 62]. Genetic tracing studies indicate the PDGFRA<sup>+</sup> cells are present in adult iWAT, but very few, if any, of new BAs induced by ADRB3 activation are derived from proliferation of cells expressing PDGFRA [51, 52].

### 1.4.3 Brown adipogenesis in BAT

Cold-induced BAT neogenesis involves an increase in adipose tissue mass that involves proliferation and is mediated by the sympathetic nervous system [63, 64]. Seminal fate mapping experiments by Bukowiecki using <sup>3</sup>H thymidine strongly indicated that new BAs arise from interstitial cells that are recruited in the first few days of cold stress [45, 55]. This work also established that neogenesis involves transient proliferation of capillary endothelial cells, although these cells were determined not to contribute to populations of new BAs. Using genetic tracing techniques and fluorescence activated cell sorting (FACS), our lab established several new concepts regarding interscapular BAT (iBAT) neogenesis. First, most, if not all, of new BAs induced by cold arise from *de novo* proliferation and differentiation of PDGFRA<sup>+</sup> progenitors [37]. This proliferation occurs transiently, after more than 2 days of cold exposure, and is concentrated within specific regions of the tissue [37, 54, 55, 64]. In addition, cold exposure also remodels the vasculature, recruits monocytes/macrophages, and triggers proliferation of uncharacterized population(s) of cells [37]. How critical these other cell types are to orchestrating BAT expansion and remodeling is presently unknown.

## 1.5 Adipocyte progenitors

*De novo* adipogenesis occurs in eWAT and iBAT from a pool of PDGFRA<sup>+</sup> adipocyte progenitors. PDGFRA<sup>+</sup> progenitors in adipose tissue are morphologically distinct, with multiple thin processes that extend into the microenvironment to contact other cell types [37, 51]. This suggests that these cells monitor the adipose tissue extracellular environment to sense stress or adipogenic stimuli in order to contribute to tissue remodeling and restoration. PDGFRA<sup>+</sup> cells are found in the adipose tissue parenchyma and in close association with tissue vasculature [37, 50, 51]. Recent lineage tracing studies confirmed that PDGFRA<sup>+</sup> cells that comprise the adventitia of the vasculature, and not endothelial or vascular smooth muscle cells, contribute significantly to adipogenesis in adult mice [65, 66]. PDGFRA<sup>+</sup> progenitors are bipotential, and can become BAs or white adipocytes depending on the stimulus [50, 51]. In eWAT, research suggests that proliferation occurs in a subset of PDGFRA<sup>+</sup> that also express the receptor CD44 [50]. CD44 is a well-known receptor for OPN, which is released in eWAT from adipose tissue macrophages to recruit progenitors to crown-like structures [50, 67].

While PDGFRA<sup>+</sup> cells undoubtedly contribute to adipogenesis, markers that define adipose tissue progenitor populations, and whether other stromal cell types (endothelial cells, vascular smooth muscle cells, *etc.*) can contribute to adipogenesis, remains highly debated. The genes *Pdgfra*, platelet-derived growth factor receptor beta (*Pdgfrb*), smooth muscle actin (*Acta2*), myosin heavy chain 11 (*Myh11*), and cadherin 5 (*Cdh5*) have all been used to tag and trace ASC differentiation *in vivo* [51, 68-72]. Whether these markers are selectively expressed in the progenitor population, or only partially overlap with progenitor cell types is not understood. To better understand the cell

types that express these markers, we will need to understand the full stromal complexity of mouse adipose tissue.

The use of smooth muscle lineage markers like *Acta2* and *Myh11* to suggest that vascular smooth muscle cell types may have the potential to dedifferentiate into adipocytes [68, 72, 73]. In fact, recent single-cell RNA-sequencing (scRNA-seq) analysis of cold-induced iBAT neogenesis claimed that populations of *Trpv+* vascular smooth muscle cells contribute to brown adipogenesis with cold exposure [73]. Studies from our lab have not observed these other cell types contributing to brown adipogenesis. However, we acknowledge the limitation of using a small set of markers to define and trace cell types, and recognize the need for a more comprehensive and unbiased approach to categorizing tissue cell types *in vivo*.

### **1.6 $\beta$ -adrenergic signaling in adipose tissue**

The  $\beta$ -adrenergic receptors are a family of G protein-coupled receptors involved in the stimulation of intracellular cAMP levels [74, 75].  $\beta$ -adrenergic receptors respond to NE released by the sympathetic nervous system. There are three subtypes:  $\beta$ 1-adrenergic receptors (ADRB1),  $\beta$ 2-adrenergic receptors (ADRB2),  $\beta$ 3-adrenergic receptors (ADRB3) [74, 75]. Specifically, ADRB1 and ADRB3 have been implicated in BAT cold-induced neogenesis and/or WAT browning [74-76].

In BAT, NE infusion induces *de novo* adipogenesis that is eliminated with global ADRB1 knockout in mice [37]. Surgical denervation also reduces cold-induced BAT neogenesis [37, 77]. Taken together, this suggests that NE released by local sympathetic innervation in BAT acts through ADRB1 in BAT to stimulate *de novo* brown adipogenesis. ADRB1 is expressed in multiple cell types in BAT, including the adipocytes, PDGFRA+

ASCs, CD31+ vascular cells, and immune cells. ADRB1 signaling stimulates proliferation of BAT SVCs *in vitro*, leading to the hypothesis that it is ADRB1 expressed on PDGFRA+ ASCs that mediates cold-induced proliferation [76, 78]. However, this has not been established in an *in vivo* system.

Expression of the ADRB3 is adipocyte-specific in adipose tissue, and ADRB3 stimulation with the agonist CL induces brown adipogenesis in WAT depots. As mentioned above, in eWAT, CL agonism of the ADRB3 triggers adipocyte death and clearance by macrophages, which simultaneously orchestrates progenitor differentiation. It is possible that a similar mechanism of adipocyte signaling and immune cell recruitment serves to promote brown adipogenesis in classic BAT as well.

### **1.7 Adipose tissue immune cells**

Adipose tissue immune cells are typically thought of in the context of obesity, where obese WAT has an increase in the M1 proinflammatory macrophages and a decrease in the M2 anti-inflammatory macrophage populations [79-81]. However, in this context of adipose tissue remodeling and not disease state, non-inflammatory immune cell types can play a role in facilitating tissue development, homeostasis, and repair [82-85].

Discussed above, ADRB3-stimulated brown adipogenesis in eWAT begins with white adipocyte efferocytosis by F4/80+ macrophages that subsequently recruit adipocyte progenitors with OPN [50, 51, 67]. Recruitment of CLS macrophages was associated with strong upregulation of M2 non-inflammatory markers, like *Arg1*, *Chi3l3*, and *Il10*, whereas proinflammatory markers remain unchanged or slightly reduced [50]. The number of F4/80+ macrophages in eWAT increased after the first day of CL treatment [50]. However, it is unclear whether this increase is due to recruitment from circulation or proliferation of

resident cells. Comparatively, CL treatment did not increase the number of F4/80+ macrophages in mouse iWAT, where no proliferation is also observed [50]. In iBAT, FACS analysis demonstrated that cold increased proliferation in a population of F4/80+ monocytes/macrophages as well [37].

Notably, in eWAT, F4/80+ macrophages contribute to adipogenesis during many diverse stimuli, and the exact phenotype of the recruited macrophage depends on the stimulus [50]. This highly specialized function of macrophages in response to different stimuli may mean that markers that categorize these cells in different tissue may not apply. These specialized phenotypes might mean that there are a diverse number of possible cell states beyond the classic macrophage M1 or M2 classification system.

We do not yet know the complete immune cell complexity of adipose tissue, or how immune cell type composition changes to respond to adipogenic stimuli. Because some of these immune cell types come from similar lineages (eg. macrophages and monocyte-derived dendritic cells), many of the classic markers may not definitively distinguish different cell types [86]. Unbiased scRNA-seq profiling would help characterize total stromal cell complexity, and help identify unique markers that define immune subtypes *in vivo*.

### **1.8 Hypothesis and aims of the project**

The organizing hypothesis of the research is that *de novo* brown adipogenesis requires a complex interaction of different adipose tissue stromal cell types, including subtypes of PDGFRA+ adipocyte progenitors and immune cells, and is orchestrated by specific ligand-receptor interactions. Preliminary findings and published data led to the following specific hypotheses: 1) PDGFRA+ adipocyte progenitors are heterogeneous,

and it is a specific subtype that give rise to new BAs in the presence of adipogenic stimuli. 2) ADRB1 present on PDGFRA+ adipocyte progenitors mediates cold-induced neogenesis in classic brown adipose tissue. 3) Adipose tissue macrophages play a role in extracellular matrix remodeling in all adipose depots, including recruiting other stromal cell types. 4) Cold-induced neogenesis in iBAT occurs in defined tissue niches with close interactions between immune cells and PDGFRA+ progenitors.

The goal of this PhD project is to fully characterize the stromal cell complexity of mouse adipose tissues and study how brown adipogenic stimuli (ADRB3 agonism and cold exposure) change the tissue composition and lead to the appearance of new brown adipocytes. These studies will also identify molecular mechanisms and cell types that drive brown adipogenesis. This primary analysis will be conducted using scRNA-seq, which can profile cell type heterogeneity in a comprehensive and unbiased fashion, and map cellular trajectories. However, we want to emphasize the importance of validation of scRNA-seq findings in the intact tissue.

Data generated from these experiments will improve the understanding of adipose tissue biology and contribute to the development of new therapies to combat T2D and obesity that include BA recruitment.

## Chapter 2. Materials and Methods

### 2.1 Experimental model and subject details

C57BL/6J (C57; stock no. 000664), B6.129S-*Pdgfra*<sup>tm1.1(cre/ERT2)Blh</sup>/J (*Pdgfra*-CreER<sup>T2</sup> mice; stock no. 032770), B6.Cg-Gt(ROSA)26Sor\_tm9(CAG-tdTomato)Hze/J (R26-LSL-tdTomato; stock no. 007909), FVB-Tg(ITGAM-DTR/EGFP)34Lan/J (ITGAM-DTR; stock no. 005515), and B6(C)-*Ccr2*<sup>tm1.1Cln</sup>/J (*Ccr2*<sup>gfp/gfp</sup>; stock no. 027619) mice were purchased from the Jackson Laboratory. Floxed *Adrb1* mice (*Adrb1*<sup>fl/fl</sup>) [87] were acquired from Dr. Jeffrey Zigman (The University of Texas Southwestern Medical Center). All mice were housed at 24°C +/- 2°C with a 12:12 light-dark cycle in an AALAC-approved animal facility at Wayne State University (Detroit, MI). Mice were fed a standard chow diet *ad libitum* (LabDiet 5L0D, PMI Nutrition International, Brentwood, MO). Animal protocols were approved by the Institutional Animal Care and Use Committee at Wayne State University. Animal protocols were approved by the Institutional Animal Care and Use Committee at Wayne State University. Mice were then euthanized by CO<sub>2</sub> asphyxiation and cervical dislocation. All mice were euthanized at 8-14 weeks of age. Animals were randomly assigned to treatment groups.

For cold exposure experiments, mice were housed in a rodent incubator (Powers Scientific, Inc.) set to 6°C for up to five days or maintained at colony room temperature as controls. In the incubators, mice were housed individually with no nesting materials in static cages. Mice were euthanized by CO<sub>2</sub> asphyxiation and cervical dislocation.

For continuous ADRB3 stimulation, mice were anesthetized using Avertin and subcutaneously implanted with micro-osmotic pumps (ALZET) containing the ADRB3 agonist CL316,243 (Sigma-Aldrich) which infused the animals at a rate of 0.75 nmol/hour

for three to four days as indicated in the text. Control mice for the eWAT and iWAT single-cell experiments underwent sham operation.

For 5-ethynyl-2'-deoxyuridine (EdU) labeling of proliferating cells, mice were injected with EdU (Invitrogen, 20 mg/kg, i.p.) prepared in sterile PBS. For flash labeling of proliferating ASCs, EdU was administered once on the third day of cold exposure, and animals were euthanized two hours later. For tracing differentiated adipocytes, EdU was administered on either day three of cold exposure, or on days three and four of cold exposure, and animals were euthanized on day five. Number of EdU injections is indicated in the figure.

Cre recombination in *Pdgfra-CreER<sup>T2</sup>/R26-LSL-tdTomato* mice was induced by administering tamoxifen dissolved in corn oil (Cayman Chemical, 100 mg/kg, oral gavage) once per day for 3-4 consecutive days. Cold exposure studies were started 1 week after the last dose of tamoxifen.

To knockout ADRB1 in PDGFRA+ ASCs *in vivo*, *Adrb1<sup>fl/fl</sup>* mice were crossed with *Pdgfra-CreER<sup>T2</sup>* mice to create mice homozygous for floxed *Adrb1* and heterozygous for *Pdgfra-CreER<sup>T2</sup>* (*Adrb1<sup>fl/fl</sup>; Pdgfra-CreER<sup>T2</sup><sup>+/-</sup>* mice). *Adrb1* was knocked out in PDGFRA+ cells by induction of *Pdgfra-CreER<sup>T2</sup>* by tamoxifen dissolved in sunflower oil (Cayman Chemical, 100 mg/kg, oral gavage) once per day for 5 consecutive days. Littermate controls without a *Pdgfra-CreER<sup>T2</sup>* allele (*Adrb1<sup>fl/fl</sup>; Pdgfra-CreER<sup>T2</sup><sup>-/-</sup>* mice) were used as controls, and also administered tamoxifen. Cold exposure studies were started 2-3 weeks after the last dose of tamoxifen.

For diphtheria toxin (DT; Sigma) injection in ITGAM-DTR mice, there were two experiments. Experiment 1: 2 mg/mL DT stock was diluted to 2.5 ug/mL and 5 ug/mL.



ITGAM-DTR<sup>+/-</sup> mice were injected i.p. with either sterile PBS, 2.5 ug/mL DT, or 5 ug/mL DT at a concentration of 10 uL/g of body weight. Two mice were injected per condition. Animals were euthanized 20 hours after i.p. injection and mouse whole blood was collected for flow cytometry by cardiac puncture. Experiment 2: ITGAM-DTR mice from Cohort 1 and Cohort 2 were tested for CD11b cell knockdown after DT injection with flow cytometry of mouse blood. DT was diluted to 2.5 ug/mL DT from a 2 mg/mL DT stock. Cohort 2 ITGAM-DTR mice were anesthetized with isoflurane and injected i.p. with sterile saline or 2.5 ug/mL DT, 1 uL per gram of body weight. Cohort 1 ITGAM-DTR mice were injected i.p. with sterile saline or 2.5 ug/mL DT, 1 uL per gram of body weight. One mouse was injected per condition, four mice total. Animals were euthanized 20 hours after i.p. injection and whole blood was collected for flow cytometry by cardiac puncture.

Two methods of liposome injection (Liposoma B.V.) into C57Bl/6j mice were used. Experiment 1: animals were housed in the cold (6C) or at room temperature. Mouse weight was recorded daily. On the second day of treatment, mice were injected i.p. with 150 uL of either 5 mg/mL control PBS-containing liposomes, or 5 mg/mL of clodronate-containing liposomes. Animals were euthanized by CO<sub>2</sub> asphyxiation and cervical dislocation on the fourth day of treatment. Experiment 2: Mouse weight was recorded daily. Mice were anesthetized using Avertin and a suprascapular incision was made to expose the subcutaneous interscapular brown adipose tissue (iBAT). iBAT was injected with either sterile PBS, PBS-containing liposomes, or clodronate-containing liposomes. 20 uL of sterile PBS, 5 mg/mL PBS-containing liposomes, or 5 mg/mL clodronate-containing liposomes was injected per pad. Following surgery, once mice were ambulatory and exhibiting normal behaviors (grooming/eating/drinking) (~1.5-2 hours),

mice were housed at room temperature or in the cold (6°C). After four days, mice were euthanized by CO<sub>2</sub> asphyxiation and cervical dislocation.

## **2.2 Tissue processing and immunohistochemistry**

Tissues were fixed with 4% paraformaldehyde overnight at 4°C, transferred through a sucrose gradient, embedded in O.C.T. compound, and cut into 20 µm-thick sections. Immunostaining was performed on fixed frozen tissue. Samples were pre-incubated with permeabilization buffer (0.3% TritonX 100 in PBS) for 30 minutes at RT and blocking buffer (5% serum corresponding to the species of the secondary antibody with 0.1% TritonX 100 in PBS) for 1 hour at RT, and then incubated with primary antibody diluted in blocking buffer overnight. Primary antibodies and dilutions used for immunohistochemistry in this study were the following: PDGFRA (goat, 1:70; R&D Systems); GPNMB (goat, 1:400; R&D Systems); I-A/I-E Alexa Fluor® 647 (MHCII) (rat, 1:100; Biolegend); mKi67 (rabbit, 1:125; Invitrogen); perilipin1 (PLIN1) (goat, 1:200; Everest Biotech); F4/80 (rat, 1:125; Bio-Rad); lens culinaris agglutinin, DyLight 649 (LCA) (1:150, Vector Laboratories); NNAT (rabbit, 1:400, abcam); isolectin GS-IB4, Alexa Fluor 568 conjugate (1:300; Invitrogen); PI16 (1:75; R&D Systems). After three washes, slides were incubated with the following secondary antibodies, diluted in blocking buffer for one hour at RT: donkey anti-rat Alexa Fluor® 647 (1:250; abcam); donkey anti-goat Alexa Fluor® 568 (1:250; Invitrogen); donkey anti-goat Alexa Fluor® 488 (1:250, Invitrogen); donkey anti-goat Alexa Fluor® 647 (1:250, Invitrogen); donkey anti-rabbit Alexa Fluor® 594 (1:250, Invitrogen); goat anti-rat Alexa Fluor® 594 (1:250, Invitrogen). HCS LipidTOX Deep Red Neutral Lipid Stain (1:500; Invitrogen) was used for lipid staining and added with secondary antibodies. For EdU detection, after antibody staining slides were stained

using the Click-iT® EdU Imaging Kit (Invitrogen) following the manufacturer's instructions. Samples were incubated with Click-iT® reaction cocktail for 30 minutes, covered. After washing, samples were counterstained with DAPI (1:5000; Sigma). Slides were coverslipped in ProLong™ Gold antifade reagent (Invitrogen) and examined by fluorescence microscopy. Staining where primary antibodies were omitted was used as nonspecific controls for immunohistochemistry.

### **2.3 Single molecule fluorescence *in situ* hybridization (smFISH)**

smFISH was conducted on fixed-frozen iBAT samples following the recently published SABER-FISH protocol [88], with some modifications. Briefly, gene specific probe sets, branch probes, the Clean.G oligo, and the Primer Exchange Reaction (PER) hairpin oligos were purchased from Invitrogen, and fluorescent-conjugated oligos were purchased from Integrated DNA Technologies or Sigma-Aldrich (St. Louis, MO). Primary probes for *Dcn*, *Top2a*, *Nnat*, *Bmper*, *Pi16*, *Gdf10*, *H2-Ab1* (MHCII), *Adrb1*, and *Gpnmb* were designed using the mm10 reference genome as described by Kishi *et al.* [88]. Primer sequences are presented in **Supplementary Table S1A**. Primary probes were concatenated to a length of ~500-750 nt and branch probes to ~500 nt in a PCR reaction containing Bst LF polymerase (640 U/mL; New England Biosciences), 300 µM each of dNTPs (dATP, dCTP, dTTP), and 10 mM MgSO<sub>4</sub>, as described previously by Kishi *et al.* (2019) in the Supplementary Protocols [88]. After synthesis, all probes were purified using MinElute PCR purification columns (Qiagen) prior to use.

iBAT tissue was excised and fixed in 10% neutral buffered formalin (NBF) for 5-7 hours at room temperature, then transferred to 30% sucrose in PBS (pH 7.4) overnight at 4°C (12-16 hours). Cryosections (20 µm) were affixed onto Superfrost plus charged slides

(Fisher Scientific) and sections preprocessed following the RNAscope technical note (TN 320534) up through the heat (antigen retrieval) step. The antigen retrieval buffer used was 10 mM citrate (pH 6.0). Sections were then lightly digested with pepsin (Digest-All 3, ThermoFisher) for 7 minutes at 40°C, rinsed in PBS (pH 7.4), and preincubated in hybridization wash buffer (40% formamide, 2X SSC pH 7 and 1% Tween-20) for 3-5 hours at 42°C. Primary probes were added at 1 µg final concentration and hybridized at 42°C for at least 16 hours. The following day, sections were washed in hybridization wash buffer and then incubated in branch hybridization solution (25% formamide, 2X SSC, 1% Tween-20, and 10% dextran sulfate) containing branch probes (100 nM) for 5 hours at 37°C. After washing in hybridization wash buffer (25% formamide), sections were incubated with fluorescent oligos (~500 nM each) for 2 hours at 37°C. Sections were then washed, stained with DAPI, and treated with TrueView (Vector labs) prior to mounting.

#### **2.4 Microscopy and image analysis**

Immunofluorescence microscopy was performed either using (1) an Olympus IX-81 microscope equipped with a spinning disc confocal unit and 10X, 20X, 40X (0.9NA) water immersion, and 60X (1.2NA) water immersion objectives, using standard excitation and emission filters (Semrock) for visualizing DAPI, FITC (Alexa Fluor 488), Cy3 (Alexa Fluor 568, 594), and Cy5 (Alexa Fluor 647, Dy-Light 649, LipidTOX), (2) a Keyence microscope (BZ-X810; Keyence; Itasca, IL) with a 40X (0.6NA) air objective; or (3) an Andor Dragonfly spinning disk confocal microscope (Andor; Belfast, UK) using 40X (1.1NA) water and 63X (1.4NA) oil objectives. Where stated, tissue autofluorescence was captured using a cyan fluorescent protein filter set (Chroma 31044V2). Raw data of single optical sections or confocal Z-stacks were processed using cellSens imaging software (Olympus).

Quantification of the distance between immune cell types (GPNMB+ MAC1 and MHCII+ dendritic cells) and tdTomato+EdU+ ASCs/adipocytes was performed on 20X single optical sections using the Measurement and ROI toolbar Arbitrary Line function in cellSens.

smFISH images acquired with the Dragonfly microscope were processed using Fusion software (v 2.3.0.44; Andor), and then analysis and quantification was performed with the Imaris Viewer x64 (v9.9.0) software using 3D view. For the *Bmper/Pi16/Nnat* analysis, images of 20 µm-thick sections from three individual cold-exposed mice were analyzed, totaling at least 90 *Nnat*<sup>+</sup> cells per animal. For each *Nnat*<sup>+</sup> cell, co-expression of *Bmper* or *Pi16* were recorded. For the *Adrb1* molecule analysis, images from two individual cold-exposed mice were analyzed per genotype (WT or *Adrb1* KO). *Nnat*<sup>+</sup> cells were identified, and the number of *Adrb1* molecules (puncta) in the same focal plane as *Nnat* expression was documented. For the neighbor analysis, images from three individual cold-exposed mice were analyzed, totaling at least 100 cells for analysis. Cells within a 20 µm diameter circle centered around the cell type of interest (*H2-Ab1*<sup>+</sup>, *Nnat*<sup>+</sup>, or *Dcn*<sup>+</sup>*Top2a*<sup>+</sup>) were documented. Analysis was performed by excluding non-classified cells within 20 µm.

## **2.5 Isolation of peritoneal macrophages and white blood cells from ITGAM-DTR mice and controls**

Scrub mice and ITGAM-DTR mice were euthanized. iBAT was extracted, interscapular WAT removed, and iBAT was placed into PBS on ice. Blood was collected by cardiac puncture and kept on ice. Peritoneal macrophages were collected by injecting 5 mL of 3% FF-BSA in PBS into the peritoneal cavity using a 27g needle and syringe [89]. The peritoneal cavity was massaged to dislodge any cells. PBS was collected with a 23g

needle and syringe and placed in a tube on ice [89]. Peritoneal cells were centrifuged at 1500 RPM at 4°C for 8 minutes and supernatant was removed. Five times the volume of RBC lysis buffer was added to mouse whole blood and incubated at RT for 10 minutes. Lysed blood sample were centrifuged at 500 *xg* at 4°C for 10 minutes and supernatant was removed.

## 2.6 RNA isolation and quantitative PCR (qPCR)

### 2.6.1 *Adrb1* KO iBAT RNA isolation and qPCR

Whole-tissue RNA was extracted from control or *Adrb1* KO mouse iBAT after being maintained at room temperature or exposed to cold for four days using TRIzol (Invitrogen). mRNA was reverse-transcribed using the High-Capacity cDNA Reverse Transcription Kit (ThermoFisher Scientific). 50 ng of cDNA was analyzed in a 20  $\mu$ L quantitative PCR reaction (DyNAmo HS SYBR Green qPCR Kit, ThermoFisher Scientific) with 500 nM of primers. Quantitative PCR was performed using the AriaMx Real-Time PCR System (Agilent Technologies). Expression data was normalized to the housekeeping gene ribosomal protein lateral stalk subunit P0 (*Rplp0*). *Rplp0* was amplified using the primers 5'-AGATTCGGGATATGCTGTTGGC-3' (forward) and 5'-TCGGGTCCTAGACCAGTGTTTC-3' (reverse). *Top2a* was amplified using primers 5'-GATGGTTTTACGGAGCCAGTTTT-3' (forward) and 5'-CACGTCAGAGGTTGAGCACT-3' (reverse). *Gpnmb* was amplified using primers 5'-CTATCCCTGGCAAAGACCCA-3' (forward) and 5'-GGCTTGACGCCTTGTGTTT-3' (reverse). *Trem2* was amplified using primers 5'-AGCACCTCCAGGCAGGTTT-3' (forward) and 5'-TTGATTCCTTGAAAGAGGAGGA-3' (reverse).

### 2.6.2 *Ccr2*<sup>gfp/gfp</sup> iBAT RNA isolation and qPCR

RNA isolation was performed by manually homogenizing flash frozen mouse iBAT and isolating RNA using the RNeasy® Lipid Tissue Mini Kit (Qiagen) following the manufacturer's instructions. Isolated RNA was quantified with the Nanodrop ND-1000 Spectrophotometer. RNA was reverse-transcribed using the High-Capacity cDNA Reverse Transcription Kit (ThermoFisher Scientific). 50 ng of cDNA was analyzed in a 20 uL quantitative PCR reaction (DyNAmo HS SYBR Green qPCR Kit, ThermoFisher Scientific) with 500 nM of primers. Quantitative PCR was performed using the AriaMx Real-Time PCR System (Agilent Technologies). Expression data was normalized to the housekeeping gene peptidylprolyl isomerase A (*Ppia*). *Ppia* was amplified using the primers 5'- GTGGTCTTTGGGAAGGTGAA-3' (forward) and 5'- TTACAGGACATTGCGAGCAG-3' (reverse). *Ccr2* was amplified using the primers 5'- GGAGCCATACCTGTAAATGCC-3' (forward) and 5'-GCCGTGGATGAACTGAGGTA-3' (reverse). *Ccl2* was amplified using the primers 5'-CCAATGAGTAGGCTGGAGAGC-3' (forward) and 5'-GAGCTTGGTGACAAAACTACAGC-3' (reverse). *Gpnmb* was amplified using primers 5'-CTATCCCTGGCAAAGACCCA-3' (forward) and 5'-GGCTTGACGCCTTGTGTTT-3' (reverse). *Trem2* was amplified using primers 5'-AGCACCTCCAGGCAGGTTT-3' (forward) and 5'-TTGATTCCTTGGAAAGAGGAGGA-3' (reverse). *mKi67* was amplified using primers 5'-CACCTGGTCACCATCAAGCG-3' (forward) and 5'-TCAATACTCCTTCCAACAGGCAGG-3' (reverse). *Irf8* was amplified using primers 5'-GATCGAACAGATCGACAGCA-3' (forward) and 5'-GCTGGTTCAGCTTTGTCTCC-3' (reverse).

### 2.6.3 ITGAM-DTR RNA isolation and qPCR

To test DTR expression in ITGAM-DTR mice, RNA was isolated from peritoneal macrophages, white blood cells, and mouse iBAT. RNA was extracted from isolated peritoneal macrophage and white blood cell samples using the Ambion Pure Link RNA Kit following the manufacturer's instructions. RNA was isolated from mouse iBAT using the same kit as follows: iBAT was cut into four pieces and added to 1 mL of Ambion Pure Link RNA Kit lysis buffer with 1% 2-mercaptoethanol. Sample was homogenized for 30 seconds using a rotor-stator homogenizer and centrifuged at 2,600  $g$  at RT for 5 minutes. Supernatant was transferred to tube, avoiding pelleted debris and top lipid layer. Equal volume of sterile 70% ethanol was added and RNA isolation proceeded following Ambion Pure Link RNA Kit instructions. Isolated RNA was quantified with the Nanodrop ND-1000 Spectrophotometer.

RNA was reverse-transcribed using the High-Capacity cDNA Reverse Transcription Kit (ThermoFisher Scientific). 50 ng of cDNA was analyzed in a 20  $\mu$ L quantitative PCR reaction (DyNAmo HS SYBR Green qPCR Kit, ThermoFisher Scientific) with 500 nM of primers. Quantitative PCR was performed using the AriaMx Real-Time PCR System (Agilent Technologies). Expression data was normalized to the housekeeping gene peptidylprolyl isomerase A (*Ppia*). *Ppia* was amplified using the primers 5'-GTGGTCTTTGGGAAGGTGAA-3' (forward) and 5'-TTACAGGACATTGCGAGCAG-3' (reverse). *Adgre1* was amplified using primers 5'-AGGAGTTTCATGCACCAAGG-3' (forward) and 5'-TGCATAGGAAACACAAAAATGG-3' (reverse). *DTR* was amplified using primers 5'-AAGATCCGCCACAACATCG-3' (forward) and 5'-GCAGCTCTAGGTTGGATTTCTG-3' (reverse) [90]. *Ucp1* was amplified using primers 5'-



CCTCTGCACTGGCACTACCT-3' (forward) and 5'-CAGGTTCTTGCGAACCTCAT-3' (reverse).

#### 2.6.4 Direct injection of liposomes, iBAT RNA isolation and qPCR

iBAT flash frozen tissue from the liposome direct injection experiments were used for RNA isolation and qPCR. RNA was extracted from mouse iBAT using the Ambion Pure Link RNA Kit as follows: iBAT was cut into four pieces and added to 1 mL of Ambion Pure Link RNA Kit lysis buffer with 1% 2-mercaptoethanol. Sample was homogenized for 30 seconds using a rotor-stator homogenizer and centrifuged at 2,600  $\times g$  at RT for 5 minutes. Supernatant was transferred to tube, avoiding pelleted debris and top lipid layer. Equal volume of sterile 70% ethanol was added and RNA isolation proceeded following Ambion Pure Link RNA Kit instructions. Isolated RNA was quantified with the Nanodrop ND-1000 Spectrophotometer.

RNA was reverse-transcribed using the High-Capacity cDNA Reverse Transcription Kit (ThermoFisher Scientific). 50 ng of cDNA was analyzed in a 20  $\mu$ L quantitative PCR reaction (DyNAmo HS SYBR Green qPCR Kit, ThermoFisher Scientific) with 500 nM of primers. Quantitative PCR was performed using the AriaMx Real-Time PCR System (Agilent Technologies). Expression data was normalized to the housekeeping gene ribosomal protein lateral stalk subunit P0 (*Rplp0*). *Rplp0* was amplified using the primers 5'-AGATTCGGGATATGCTGTTGGC-3' (forward) and 5'-TCGGGTCCTAGACCAGTGTTTC-3' (reverse). *Gpnmb* was amplified using primers 5'-CTATCCCTGGCAAAGACCCA-3' (forward) and 5'-GGCTTGTACGCCTTGTGTTT-3' (reverse). *Trem2* was amplified using primers 5'-AGCACCTCCAGGCAGGTTT-3' (forward) and 5'-TTGATTCCTTGGAAAGAGGAGGA-3' (reverse). *Spp1* was amplified

using primers 5'-TCCTTGCTTGGGTTTGCAGT-3' (forward) and 5'-CATGGTCGTAGTTAGTCCCTCA-3' (reverse). *Birc5* was amplified using primers 5'-ACCGAGAACGAGCCTGATTT-3' (forward) and 5'-ATGCTCCTCTATCGGGTTGTC-3' (reverse). *mKi67* was amplified using primers 5'-CACCTGGTCACCATCAAGCG-3' (forward) and 5'-TCAATACTCCTTCCAAACAGGCAGG-3' (reverse). *Top2a* was amplified using primers 5'-GATGGTTTTACGGAGCCAGTTTT-3' (forward) and 5'-CACGTCAGAGGTTGAGCACT-3' (reverse). *Irf8* was amplified using primers 5'-GATCGAACAGATCGACAGCA-3' (forward) and 5'-GCTGGTTCAGCTTTGTCTCC-3' (reverse). *Ucp1* was amplified using primers 5'-CCTCTGCACTGGCACTACCT-3' (forward) and 5'-CAGGTTCTTGCGAACCTCAT-3' (reverse).

## **2.7 ITGAM-DTR genotyping and sequencing PCR product**

DNA from ITGAM-DTR mouse ear tissue was isolated and amplified using the Extract-N-Amp Tissue PCR Kit (Sigma-Aldrich) using the recommended DTR primers (Jackson Labs Protocol 22579) and following the manufacturer's instructions. The *Dtr* transgene was amplified using the primers 5'-GGGACCATGAAGCTGCTGCCG-3' (forward) and 5'-TCAGTGGGAATTAGTCATGCC-3' (reverse) (product = 625 bp). Internal positive control primers were 5'-CAAATGTTGCTTGTCTGGTG-3' (forward) and 5'-GTCAGTCGAGTGCACAGTTT-3' (reverse) (product = 200 bp). DNA extracts were separated on a 1% agarose gel with 0.005% ethidium bromide. PCR products were visualized with the Azure c600 Imager (Azure Biosciences). For sequencing the DTR PCR product, DNA was extracted from the gel using the PCR Clean-up Gel Extraction Kit for DNA isolation (Macherey-Nagel) following the manufacturer's instructions. DNA was quantified on the Nanodrop ND-1000 Spectrophotometer and 20 ng was sent for

sequencing by GeneWiz. Sequence alignment was determined using the NCBI Basic Local Alignment Search Tool [91].

## **2.8 Fluorescence-activated cell sorting (FACS)**

### **2.8.1 FACS isolation and RNA library prep of PDGFRA<sup>+</sup>CD44<sup>+</sup> cells from mouse eWAT**

Isolated eWAT SVCs from control or 3 day CL-treated mice (3 mice per treatment) were pooled and resuspended in HBSS containing 1 mM EDTA (Boston BioProducts Inc.; Ashland, MA), 2.5 mM HEPES and 1% FBS at a final concentration of  $1 \times 10^7$  cells/mL. SVCs were pre-incubated with Fc block (anti-mouse-CD16/32; Biolegend; San Diego, CA; cat# 101302) ( $0.5 \text{ ug}/1 \times 10^6$  cells) for 10 min and then incubated with anti-mouse PDGFR $\alpha$ -PE (anti-CD140a; 1/200; Biolegend cat#135906) and anti-mouse CD44-FITC (1/100; Biolegend cat#103006) for 30 min [50, 51] at 4°C protected from light. Cells were washed twice with HBSS to remove unbound antibodies.

Cells were sorted using Sony SH800 Cell Sorter (Sony Biotechnology; San Jose, CA) using 488nm laser. Emission filters used were for PE: 561LP plus 585/30; and FITC: dichroic 561LP plus 525/50. All compensation was performed at the time of acquisition in SH800 software using compensation beads (Biolegend) for single color staining and SVCs for negative staining and fluorescence minus one controls.

SVC from control and CL-treated were sorted for each experiment and the experiment was repeated 4 independent times. Sorted PDGFRA<sup>+</sup>CD44<sup>-</sup> and PDGFRA<sup>+</sup>CD44<sup>+</sup> cells were collected in TRIzol (Ambion, Thermo Fisher Scientific), and total RNA was isolated using micro Direct-zol™ RNA Microprep kit (Zymo Research; Irvine, CA). RNA concentration and quality were measured using Nano-drop 2000 (Thermo Fisher

Scientific) and Bioanalyzer 2100 Eukaryote Total RNA Nano kit (Agilent; Santa Clara, CA). All samples had an RNA integrity number (RIN) greater than 7.

### **2.8.2 FACS analysis to test CD11b<sup>+</sup> cell knockdown in ITGAM-DTR mice with DT injection**

Cell suspension was stained using the Fixable Viability Stain 510 (BD Biosciences) prior to incubation with antibodies. Cells were washed and incubated with PE-CF594 Rat Anti-CD11b antibody (BD Biosciences) for 30 min in the dark at 4°C. After washing, RBCs were lysed using Lysing Solution (BD Biosciences). After washing, cells were resuspended in 0.5 mL of stain buffer and acquired using the BD LSRFortessa flow cytometer and FACSDiva 8.0 software. The analysis and figures were performed and created using FlowJo software v10 (FlowJo, Ashland, OR, USA).

### **2.9 RNA-seq library preparation and sequencing**

#### **2.9.1 RNA-seq library preparation and sequencing of FACS-sorted eWAT PDGFRA<sup>+</sup> cells**

RNA-seq libraries from FACS isolated PDGFRA<sup>+</sup> cells from eWAT of control and 3 day CL-treated mice were prepared using the QuantSeq forward 3'-mRNA-Seq Library Prep kit (Lexogen GmbH, Vienna, Austria) from 70 ng total RNA according to manufacturer instructions. Libraries quality and concentration were assessed using 2100 Bioanalyzer High Sensitivity DNA kit (Agilent; Santa Clara, CA) and KAPA SYBR Fast Universal qPCR Kit (Roche; Madison, WI), respectively, and then pooled at equal concentrations. Libraries were sequenced by GENEWIZ Inc (South Plainfield, NJ) using Illumina HiSeq system (Illumina; San Diego, CA) with a 1x50bp configuration, yielding ~5 million reads per sample.

RNA sequencing data from FACs sorted PDGFRA+, CD44+/- cells were demultiplexed and then further processed using the Bluebee genomics platform (Cambridge, MA). Differential gene expression analysis was conducted using DESeq2 in the DEApp program [92], with the filtering threshold set at a fold change (FC) >1.5 and the false discovery rate (FDR) adjusted p value <0.05. Normalized read counts (Log2 transformed) of the differentially expressed genes (PDGFRA+/CD44- vs PDGFRA+/CD44+; CON vs CL) were then extracted using the preprocess reads counts module in GenePattern v3.9.10 ([www.broadinstitute.org/genepattern](http://www.broadinstitute.org/genepattern)), and hierarchal clustering analysis performed in Heatmapper, as described [93].

### **2.9.2 RNA-seq library preparation and sequencing of iBAT from cold exposure time course**

RNA was isolated from mouse iBAT following the standard protocol for the Direct-zol RNA Miniprep kit (Zymo Research) and assessed for quality on the Agilent 2200 TapeStation (Agilent Technologies). Transcriptome profiles were generated using the QuantSeq 3'mRNA-Seq Library Prep Kit FWD for Illumina (Lexogen) with 250 ng of total RNA. Libraries were sequenced on an Illumina NovaSeq 6000 using a SP 100 cycle NovaSeq flow cell with read length configuration 76 bp with dual indexing: 12 bp for i7 and i5 indexing. Sequencing data was demultiplexed using Illumina's CASAVA 1.8.2 software.

Sequencing reads were aligned to the mouse genome with STAR-2.6.1d [94]. HTseq (v0.11.2) [95] was used to determine the read counts per gene based on Ensembl gene annotations from mouse Gencode release 38 (GRCm38.98). We sequenced a total of

~171.3 million reads, with an average of ~4.9 million reads per library. Raw count data was uploaded into iDEP [96], a web application for analysis of RNA-seq data. Data was transformed in iDEP (v0.95) using the rlog function. K-means clustering was performed on the top 2,000 DEGs with  $k = 4$  clusters. Analysis focused on the clusters of genes upregulated with cold exposure.

## **2.10 Isolation of stromal vascular cell from mouse adipose tissue**

### **2.10.1 Isolation of stromal vascular cells from mouse eWAT and iWAT**

Epididymal and inguinal white adipose tissues (WAT) were surgically removed after CL treatment and processed for stromal vascular cell (SVC) isolation (**Figure 1A**). Tissues of 4 mice were pooled for SVC isolation, as previously described [51]. Briefly, following dissection, eWAT and iWAT were washed with PBS, minced, and digested with Collagenase Type 2 (eWAT: 1 mg/mL; iWAT: 2 mg/mL; Worthington Biochemical Co.) in Hanks' balanced salt's solution (HBSS; Gibco; Sigma-Aldrich) containing sodium bicarbonate, 10 mM HEPES (pH 7.4, Gibco; Sigma-Aldrich) and 0.5% fatty acid free bovine serum albumin (FF-BSA; Gemini Bio-products, West Sacramento, CA) for 30 minutes at 37°C. Ethylenediaminetetraacetic acid (EDTA) was added to a final concentration 10 mM and the tissues were incubated for an additional 5 minutes to promote full dissociation of SVCs.

Dissociated cells were filtered through a cell strainer, washed with a PBS buffer containing 1 mM EDTA, 2.5 mM HEPES, and 10% heat-inactivated fetal bovine serum (FBS, Atlanta Biologicals Inc; Flowery Branch, GA) (FACS buffer), then centrifuged at 500 × g for 10 minutes at 4 °C. After removing the supernatant, pellets containing the stromal vascular fraction were incubated in red blood cell lysis buffer (containing sodium

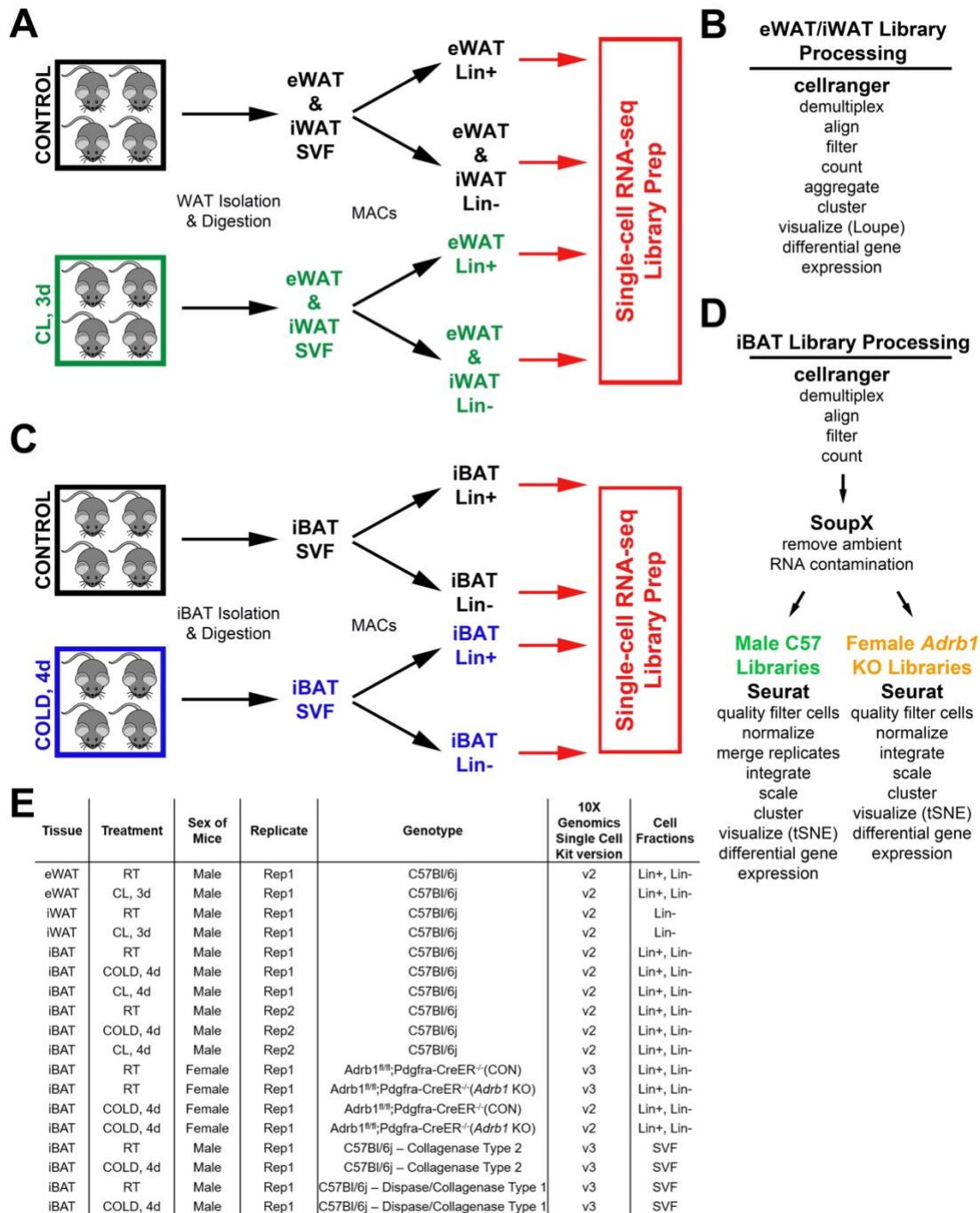


**Figure 1. Schematic diagram of single-cell library generation and processing (A)**

Schematic of eWAT/iWAT single-cell experiment from cohorts of control and CL-treated mice. Mouse eWAT and iWAT were harvested and digested into the stromal vascular fraction (SVF). These cells were separated into lineage marker positive (Lin+) and negative (Lin-) cell fractions with magnetic bead cell separation (MACS). Single-cell libraries were prepared from these cell fractions. (B) Method of demultiplexing and data analysis for the eWAT and iWAT scRNA-seq libraries. (C) Schematic of one iBAT single-cell experiment from cohorts of control and cold-exposed mice. (D) Method of demultiplexing and data analysis for the iBAT scRNA-seq libraries. Analysis of C57 and *Adrb1* KO libraries differed slightly due to method of library generation. (E) Summary of the single-cell libraries described.

ammonium chloride, and 0.5 M EDTA; pH 7.4) for 5 minutes at room temperature, then passed through a 100  $\mu$ m sterile cell strainer and collected by centrifugation at 500 $\times$ g for at 4°C for 10 minutes. Cellular debris was removed by gradient centrifugation in Iodixanol solution (52.2% and 50% Iodixanol; OptiPrep; Sigma-Aldrich; St. Louis, MO) overlaid with FACS buffer. Cells recovered in the FACS buffer layer were pelleted, washed, and resuspended in PBS containing 5% FF-BSA.

### **2.10.2 Isolation of stromal vascular cells from mouse iBAT**

For cold exposure and CL treatment experiments, male C57 mice were exposed to cold (6°C) or infused with CL for four days, or maintained as room temperature controls. For ADRB1 KO experiments, female *Adrb1<sup>fl/fl</sup>;Pdgfra-CreER<sup>T2+/-</sup>* mice and *Adrb1<sup>fl/fl</sup>;Pdgfra-CreER<sup>T2-/-</sup>* genotype controls, all treated with tamoxifen, were exposed to cold for four days or maintained at room temperature. Interscapular brown adipose tissues were surgically removed and processed for stromal vascular cell (SVC) isolation. Tissues of 3-4 mice were pooled after digestion for SVC isolation, similar to methods previously described [51, 97] (**Figure 1C**). Briefly, following dissection, iBAT pads were washed with PBS, minced, and digested with 2 mg/mL Collagenase Type 2 (Worthington Biochemical Co.) in Hanks' balanced salt's solution (HBSS; Sigma-Aldrich) containing 4 mM sodium bicarbonate, 10 mM HEPES (pH 7.4, Gibco; Sigma-Aldrich) and 0.5% fatty acid free bovine serum albumin (FF-BSA; Gemini Bioproducts, West Sacramento, CA) for 30 minutes at 37°C (**Figure 1C**). Ethylenediaminetetraacetic acid (EDTA) was added to a final concentration of 10 mM and samples were incubated for an additional 5 minutes to promote complete dissociation of SVCs.



Digested cell samples from the same treatment group were combined and filtered through 100  $\mu\text{m}$  and 40  $\mu\text{m}$  sterile cell strainers. The samples were washed with PBS buffer containing 1 mM EDTA, 2.5 mM HEPES, and 10% heat-inactivated fetal bovine serum (FBS, Atlanta Biologicals Inc) (FACS buffer) and centrifuged at 500 x  $g$  for 10 minutes at 4°C. After removing the supernatant, pelleted stromal vascular cells were incubated in red blood cell lysis buffer containing 14 mM sodium bicarbonate, 0.154 M ammonium chloride, and 0.1 mM EDTA for 5 minutes at room temperature, then passed through a 100  $\mu\text{m}$  sterile cell strainer. Cells were collected by centrifugation at 500 x  $g$  for 10 minutes at 4°C. Cellular debris was removed by density gradient centrifugation using Debris Removal Solution (Miltenyi Biotec). Cells recovered were resuspended in PBS containing 0.5% FF-BSA.

### **2.10.3 Protocol for comparing digestion methods of mouse iBAT**

Male C57 mice were exposed to cold (6°C) or maintained as room temperature controls. Interscapular brown adipose tissues were surgically removed, washed with PBS, interscapular white adipose tissue was removed, and iBAT was minced. Tissue was digested using one of two protocols. Protocol 1: identical method to those collected in our iBAT single-cell libraries. Minced tissue was digested with 2 mg/mL Collagenase Type 2 (Worthington Biochemical Co.) in Hanks' balanced salt's solution (HBSS; Sigma-Aldrich) containing 4 mM sodium bicarbonate, 10 mM HEPES (pH 7.4, Gibco; Sigma-Aldrich) and 0.5% fatty acid free bovine serum albumin (FF-BSA; Gemini Bioproducts, West Sacramento, CA). Samples were incubated for 30 minutes at 37°C in an incubator shaker at 280 RPM. During incubation, vigorously shake tubes by hand for 10 seconds every 10 minutes. Ethylenediaminetetraacetic acid (EDTA) was added to a final concentration of

10 mM, samples were shaken, and samples incubated for an additional 5 minutes to promote complete dissociation of SVCs. Protocol 2: similar to the method used in Shamsi, *et al.* [73]. Minced tissue was digested with 1.5 mg/mL Collagenase Type 1 (Worthington Biochemical Co.) and 2.5 U/mL Dispase II (Stem Cell Technologies) in a 2% fatty acid free bovine serum albumin (FF-BSA; Gemini Bioproducts, West Sacramento, CA) in HBSS (Sigma-Aldrich) buffer for 45 minutes in a 37°C water bath shaking at 150 RPM. Following this digestion, samples were vortexed for 10 seconds. Following these two tissue digestion protocols, all samples were similarly filtered, RBCs were lysed, and debris was removed using the same protocol described for mouse iBAT above to isolate stromal vascular cells, beginning where samples are combined and filtered through 100 µm and 40 µm sterile cell strainers. Note that the single-cell libraries from these experiments were from total SVF cells from each condition.

### **2.11 Magnetic activated cell sorting into lineage marker positive (Lin+) and lineage marker negative (Lin-) cell fractions**

For specified experiments, adipose tissue SVCs from BAT and WAT were separated into lineage-marker positive (Lin+) and lineage-marker negative (Lin-) cell fractions using magnetic bead cell separation (MACS) (**Figure 1A**). SVCs were labeled using the mouse Lineage Cell Depletion kit (Miltenyi Biotec) according to the manufacturer's instructions. This kit contains anti-CD5, anti-CD11b, anti-CD45R (B220), anti-Gr-1 (Ly-6G/C), anti-7-4, and anti-Ter-119 antibodies. Labeled samples were passed onto MS columns (Miltenyi Biotec) on the OctoMACS separator (Miltenyi Biotec); the flow through was collected as the Lin- cell fraction and bound Lin+ cells were eluted from the column. Samples were

centrifuged at 500 x g for 10 minutes at 4°C and pelleted cells were resuspended in PBS with 0.04% FF-BSA. Cells were counted and diluted to a concentration of 1,000 cells/uL.

## 2.12 Single-cell RNA-sequencing and analysis

### 2.12.1 Single-cell RNA-sequencing and analysis of eWAT and iWAT cells

Following magnetic cell sorting, single cell RNA libraries for Lin- eWAT and iWAT, along with Lin+ eWAT were loaded onto the Single Cell 3' Chip. Approximately 10,000 cells were loaded per channel for an expected recovery of ~6,000 cells. The loaded Single Cell 3' Chip was placed on a 10X Genomics Chromium™ Controller Instrument (10X Genomics, Pleasanton, CA, USA) to generate single cell gel beads in emulsion (GEMs). Single cell RNA-seq libraries were prepared using the Chromium Single Cell 3' Library & Cell Bead Kit (Cat. No. 120237, 120236, 120262; 10X Genomics) according to the manufacturer's protocol. Libraries were sequenced with an Illumina NextSeq500 using high output 75-cycle kits with the following read length configuration: 26 bp read1, 14bp I7index, 8bp I5 index and 58 bp read2.

The Cell Ranger™ Single Cell Software Suite v.2.0.1 was used to perform sample demultiplexing, alignment, filtering, and UMI counting (<https://support.10xgenomics.com/single-cell-gene-expression/software/pipelines/latest/what-is-cell-ranger>) (**Figure 1B**). Sham surgery and CL treatment data for each respective subpopulation were aggregated for direct comparison of single cell transcriptomes (**Figure 1B**). Clustering and gene expression were visualized with 10X Genomics Loupe™ Cell Browser v.1.0.1 (<https://support.10xgenomics.com/single-cell-gene-expression/software/visualization/latest/what-is-loupe-cell-browser>).

The complete spreadsheet of the sequencing metrics is presented in **Supplementary Table S1B**. A total of 33,663 single cells consisting of the Lineage+ and Lineage-cell subpopulations were captured, with the number of cells recovered per channel ranging from 3,472 to 8,131. The mean reads per cell varied from 15,154 and 39,037 with median Unique Molecular Indexes of 2,678 to 5,545 per cell.

Cell Ranger™ software (10X Genomics) was used to identify cluster-specific gene expression. Cell Ranger™ tests whether the in-cluster mean gene expression per cell differs from the out-of-cluster mean for each gene and each cluster. A negative binomial exact test is employed to find differentially expressed genes between clusters (Robinson and Smyth, 2008; Yu et al., 2013). Unless we indicate which two groups of cells are compared, the analysis is run on one cluster versus all other cells. The output is a list of genes that are differentially expressed where p-values are adjusted to account for the number of hypotheses (i.e. genes) being tested using Benjamini-Hochberg procedure. To produce violin plots of the mean and variance of the mean and variance of gene expression density, cluster identities and filtered gene matrices generated by Cell Ranger™ were used as input into the open-source R toolkit Seurat (<http://satijalab.org/seurat/>) (Satija et al., 2015). Cluster identities for each cell as defined by K-means clustering in Cell Ranger™ were set as the identities in the Seurat object. Violin plots for the given genes were generated using the Seurat toolkit VlnPlot function. Gene ontologies of DEGs were assessed using the PANTHER Overrepresentation Test (Gene Ontology Consortium, <http://www.geneontology.org/>), with the reported p-values corrected by the Bonferroni adjustment for multiple comparisons.

For independent clustering and pseudotime analysis, using the cluster identities defined by K-means clustering in Cell Ranger™, clusters Diff. ASC and Pro. ASC from the eWAT Lin- data were subset and input into Seurat for clustering and pseudotime analysis. After quality filtering cells and log normalization of reads, principal component analysis, shared nearest neighbor clustering, and t-SNE projection were performed. Plotting the first two principal components revealed that -[PC1] could be used as a surrogate for pseudotime. Using a standard linear model (i.e., Pearson correlation), normalized gene expression for all genes was correlated with pseudotime. Finally, p-values were adjusted using the Benjamini-Hochberg procedure.

### **2.13.2 Single-cell RNA-sequencing and analysis of iBAT libraries from RT, COLD, CL, and *Adrb1* KO libraries**

Single-cell libraries for all samples were prepared using the 10X Genomics Chromium Single Cell 3' Reagent Kit v2, apart from *Adrb1* KO and WT RT libraries which were prepared with Reagent Kit v3 (**Figure 1D**). Following MACS, single-cell suspensions were loaded onto the Single Cell Chip A. An estimated 10,000 cells were loaded per lane for an expected recovery of ~6,000 cells per library. The assembled chip was placed on a 10X Genomics Chromium™ Controller Instrument (10X Genomics) to generate single-cell gel beads in emulsion (GEMs). Single-cell RNA-seq libraries were prepared according to the manufacturer's instructions. Libraries were quantified using the Kappa PCR kit (Kappa Biosystems) and sequenced with the Illumina NextSeq500 using high output 75-cycle kits with the following read length configuration: v2 libraries 26 bp read1, 8 bp I7 index, and 58 bp read2, v3 libraries 28 bp read1, 8 bp I7 index, and 56 bp read2.

10X Genomics Cell Ranger (v3.0.1) was used to perform sample demultiplexing, alignment, filtering, and UMI counting (**Figure 1D**). Sequencing metrics is presented in **Supplementary Table S1B**. Count files were processed using SoupX (v1.0.1) [98], an R package for the estimation and removal of cell-free mRNA contamination in single-cell data (**Figure 1D**). For SoupX library cleanup, *Fabp4* and *Car3* were used as the non-expressed genes, as we expect the largest contribution of contamination to come from damaged mature BAs that have been excluded from these libraries, and `clusters=FALSE`. Corrected count libraries were input into the R program Seurat (v3.1.5) [99] and libraries were quality filtered (Lin+: `percent.mt < 10 & nCount_RNA < 15000 & nFeature_RNA < 4000`; Lin-: `percent.mt < 10 & nCount_RNA < 15000 & nFeature_RNA > 100`) (**Figure 1D**). For the C57 RT, COLD, and CL libraries, after normalization, libraries from the same replicate experiment were merged (i.e. `Replicate1_Lin-_RT + Replicate1_Lin-_COLD = Replicate1_merge`). The top 2,000 variable genes were identified for each merged object, and objects from similar cell fractions (Lin+ or Lin-) were integrated to align common features of the dataset. For the ADRB1 WT and KO libraries, because the libraries for different treatments were collected on different days and with different version of the 10X kit, we integrated all of the libraries in Seurat to correct for these effects and perform comparative scRNA-seq across the libraries. Therefore, after normalization we identified the top 2,000 variable genes were identified for each library and all libraries were integrated. For all integrated objects, we performed linear dimensional reduction, cell clustering, and data visualization using t-distributed stochastic neighbor embedding (t-SNE). Differentially expressed genes that define each cluster were identified using a Wilcoxon Rank Sum test in Seurat with the following parameters: `min.pct = 0.20`,

logfc.threshold = 0.2, only.pos = TRUE (**Figure 1D**). These markers were used to assign cell type identity. Gene Ontology (GO) analysis of DEGs and p-values were produced by the The Gene Ontology Consortium [100, 101]. Volcano plots were prepared from DEGs calculated by distinguishing ASCs from control libraries with ASCs from cold libraries (*i.e.* ASC2\_controls vs. ASC2\_cold). Colored points and quantification displayed on the plot are the number of genes with an adjusted p-value less than 0.05 and the absolute value of the fold change greater than 0.5.

### **2.13.3 Single-cell RNA-sequencing and analysis of iBAT libraries testing alternative digestion methods**

Single-cell libraries for the four SVF samples testing alternative digestion methods were prepared using the 10X Genomics Chromium Single Cell 3' Reagent Kit v3 (**Figure 1E**). Single-cell SVF suspensions were loaded onto the Single Cell Chip G. An estimated 20,000 cells were loaded per lane. The assembled chip was placed on a 10X Genomics Chromium™ Controller Instrument (10X Genomics) to generate single-cell gel beads in emulsion (GEMs). Single-cell RNA-seq libraries were prepared according to the manufacturer's instructions. Libraries were quantified using the Kappa PCR kit (Kappa Biosystems). Libraries were sequenced on an Illumina NovaSeq 6000 using a SP 100 cycle NovaSeq flow cell. Sequencing data was demultiplexed using Illumina's CASAVA 1.8.2 software.

10X Genomics Cell Ranger (v3.0.1) was used to perform sample demultiplexing, alignment, filtering, and UMI counting (**Figure 1D**). Sequencing metrics is presented in **Supplementary Table S1B**. Count files were processed using SoupX (v1.0.1) [98], using *Fabp4* and *Car3* as the non-expressed genes and clusters=FALSE. Corrected count

libraries were input into the R program Seurat (v3.1.5) [99] and libraries were quality filtered (percent.mt < 10 & nFeature\_RNA < 5000 & nCount\_RNA < 20000) (**Figure 1D**). After normalization, libraries from the same method were merged (i.e. CollagenseType2\_RT + CollagenaseType2\_COLD = CollagenseType2\_merge). The top 2,000 variable genes were identified for each merged object, and objects were integrated to align common features of the dataset. On the integrated object, we performed linear dimensional reduction, cell clustering, and data visualization using t-SNE. Differentially expressed genes that define each cluster were identified using a Wilcoxon Rank Sum test in Seurat with the following parameters: min.pct = 0.20, logfc.threshold = 0.2, only.pos = TRUE. These markers were used to assign cell type identity.

#### **2.14 Ligand-Receptor Analysis**

To identify potential ligand-receptor pairs in our single-cell dataset, we used the computational programs CellPhoneDB (v2.1.3) [102] and NicheNet (v0.1.0) [103]. CellPhoneDB is a curated repository of ligands and receptors that interrogates single-cell data for expression of these pairs. The NicheNet repository utilizes a model that incorporates intracellular signaling to prioritize pairs. In addition to these computational programs, we generated lists of genes expressed in each cell type and cross-referenced them with two databases: the NicheNet ligand-receptor database and the mouse ligand and receptor database compiled in Skelly, *et al.* [104]. The results from each method were compiled into a master list of potential ligand-receptor pairs. Finally, every ligand and receptor were manually plotted in our single-cell dataset to remove those with expression not specific to the MAC/DEND cells (ligands) and the ASC1\_cold-activated cells (receptors).



### 2.15 Analysis and integration of Shamsi, *et al.* data

.fastq files from Shamsi, et al. were downloaded from the Sequence Read Archive that was linked to the data deposited at the Gene Expression Omnibus (GSE160585) [73]. Reads were aligned and counted using cellranger (v3.0.1) before processing with SoupX (v1.0.1) [98] using the same parameters used for our iBAT single-cell libraries. For SoupX library cleanup, *Fabp4* and *Car3* were used as the non-expressed genes, as we expect the largest contribution of contamination to come from damaged mature BAs that have been excluded from these libraries, and clusters=FALSE. The 16 corrected count libraries were input into the R program Seurat (v3.1.5) [99] and libraries were quality filtered (percent.mt < 10 & nCount\_RNA < 15000 & nFeature\_RNA < 4000). Libraries were merged and visualized using t-SNE with 30 dimensions at a resolution of 0.3. After analyzing cluster DEGs, clusters corresponding to RBCs were removed and the data was reclustered. Cells were divided into immune cell clusters and non-immune cell clusters based on cluster DEGs and the expression of *Cd52* and *Ptprc*. Once cell types in the data were separated, these cells could be integrated with our iBAT single-cell Lin+ and Lin- data.

### 2.16 Quantification and Statistical Analysis

Statistical analyses were performed using GraphPad Prism v9.3.1 software (GraphPad Software, San Diego, CA, USA), R (v4.0.3) [105] and RStudio [106], or an online Chi-square Calculator [107]. Data are presented as mean  $\pm$  SD or mean  $\pm$  SEM as indicated in the figure legend. Comparison among groups was performed using a 2-way ANOVA on log transformed data. Pearson correlation coefficient was calculated in R using cor() function and reported p-values were calculated using the cor.test() function.

## **2.17 Data and Software Availability**

FASTQ files from the eWAT and iWAT scRNA-seq libraries are available at the Sequence Read Archive (SRA; <https://www.ncbi.nlm.nih.gov/sra/>) (SRA: SRP145475). FASTQ files and count matrices are available at the GEO Scripts for all data processing are available through GitHub (<https://github.com/RBBurl1227>).

## Chapter 3. Deconstructing adipogenesis induced by $\beta$ -adrenergic receptor activation with single-cell expression profiling

### 3.1 RNA-Seq analysis of FACS-isolated progenitors suggests a complex adipogenic trajectory

CL treatment induces proliferation of ASCs that differentiate into BAs in eWAT, and previous work suggested that the expression of the surface marker CD44 could be used to identify ASCs undergoing adipogenic differentiation [50, 108, 109]. To gain greater insight into the activation process, we analyzed the gene expression pattern of PDGFRA<sup>+</sup> cells from control (CON) and CL-treated mice that were positive or negative for CD44 (**Figure 2 and Supplementary Table S2A-E**). In controls, 4.2% of PDGFRA<sup>+</sup> cells expressed CD44 (PDGFRA<sup>+</sup>CD44<sup>+</sup>), and these cells exhibited upregulated expression of cell cycle genes (*Prc1*, *Cdca8*, *Plk1*; fold change (FC) > 3.7, adjusted p < 0.00002), as well as genes involved in early adipogenic differentiation (*Cebpa*, FC = 2.5, adjusted p < 0.000005) compared to PDGFRA<sup>+</sup>CD44<sup>-</sup> cells (**Supplementary Table S2D**). CL increased the percentage of PDGFRA<sup>+</sup>CD44<sup>+</sup> cells by ~4-fold (t-test, p < 0.01, n = 4 independent experiments) (**Figure 2A**), and further upregulated genes associated with cell migration, mitotic cytokinesis, extracellular matrix (ECM) remodeling, and adipogenic differentiation compared to control quiescent PDGFRA<sup>+</sup>CD44<sup>-</sup> cells (**Supplementary Table S2E**). These results confirm that CD44 expression enriches for newly-recruited ASCs; however, the gene expression pattern suggested that the PDGFRA<sup>+</sup>CD44<sup>+</sup> subpopulation contained a complex mixture of cells undergoing migration, proliferation, and differentiation. Furthermore, it was clear that bulk sequencing of FACS-isolated

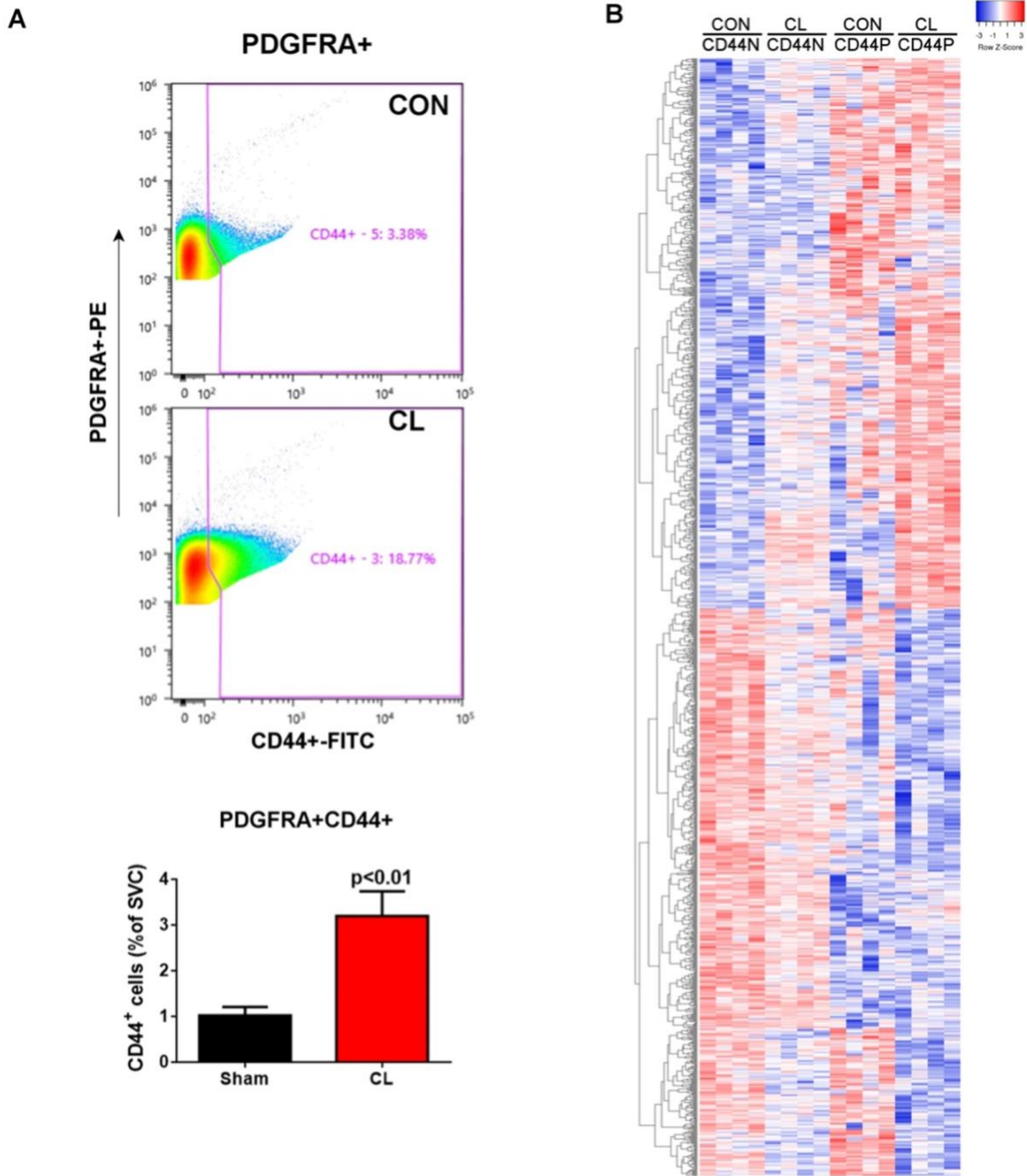


**Figure 2. RNA-seq analysis of FACS-isolated PDGFRA<sup>+</sup> cells from eWAT of control and CL-treatment mice** (A) Upper panel: representative plot of fluorescence-activated cell sorting analysis of stromal vascular cells (SVC) showing PDGFRA<sup>+</sup> cells sorted as CD44<sup>+</sup> and CD44<sup>-</sup> in control (CON) and CL-treated mice. Lower panel: Average data from 4 independent experiments. (B) Pearson complete linkage hierarchical clustering analysis of differentially expressed genes among PDGFRA<sup>+</sup>CD44<sup>-</sup> (CD44P) and PDGFRA<sup>+</sup>CD44<sup>-</sup> (CD44N) cells in CON and CL-treated mice. Colors in the heatmap represent row Z-score calculated from normalized transcript reads (Log<sub>2</sub> transformed).

subpopulations was unlikely to further deconvolve this interesting heterogeneity.

### **3.2 scRNA-seq deconvolves progenitor heterogeneity and defines an adipogenic trajectory**

In order to address stromal cell complexity and begin to unravel adipogenic trajectories *in vivo*, we performed scRNA-seq analysis of stromal cells isolated from eWAT of sham controls and mice infused with CL for 3 days, a time of maximal proliferation and early differentiation [50, 109]. Stromal cells were isolated and fractionated into lineage marker positive (Lin+) cells (mostly immune cells) and all other stromal cells (Lin-) using magnetic bead cell sorting (MACS). Separate single-cell libraries were prepared from control and CL-treated mice for each cell fraction (Lin+ or Lin-) and sequenced. We adopted this cell fractionation and sequencing strategy to demonstrate that single-cell profiles corresponded to the expected profiles of physically isolated cells and to gain greater depth of coverage for detecting rare cell types. Thus, 100% of single cells expressing *Adgre1* (the gene encoding the macrophage antigen F4/80) were found in the eWAT Lin+ fraction, whereas more than 96% of cells expressing the ASC marker *Pdgfra* were found in the Lin- fraction.

Our general analytic approach was to aggregate single-cell libraries from Lin+ and Lin- cells separately across experimental conditions and visualize the relationships using t-distributed stochastic neighbor embedding (t-SNE) plots. Aggregated and normalized data were subjected to K-means or graph-based clustering to identify cell types/states, which were projected onto the t-SNE plots using the 10X Genomics software package. K-means clustering of scRNA-seq data from eWAT Lin- cells from control and CL-treated

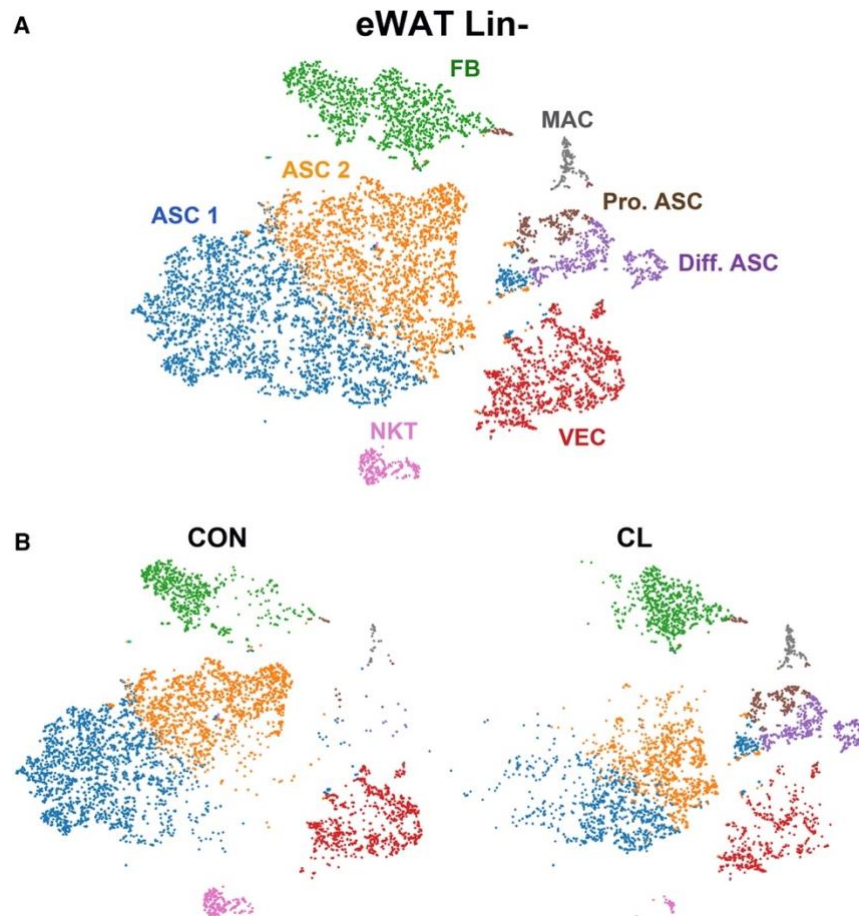


**Figure 3. Single-Cell RNA-Seq Reveals ASC Heterogeneity in Mouse eWAT** (A) t-SNE plot of 9,915 lineage-negative (Lin<sup>-</sup>) stromal vascular cells from eWAT of control mice and mice treated with CL for 3 days. K-means clustering applied to the t-SNE plot identified eight major cell types/states (the table of significant DEGs used to define these clusters is presented in Supplementary Table S3A). Clusters are highlighted in different colors. ASC, adipocyte stem cells; MAC, macrophages; VEC, vascular endothelial cells; NKT, natural killer T cells; FB, fibroblasts; Pro. ASC, proliferating adipocyte stem cells; Diff. ASC, differentiating adipocyte stem cells. Cell counts by cluster: ASC 1 = 3,185 (32%), ASC 2 = 2,654 (27%), FB 3 = 1,443 (15%), VEC 4 = 1,320 (13%), Diff. ASC 5 = 530 (5%), Pro. ASC 6 = 324 (3%), NKT 7 = 274 (3%), MAC 8 = 183 (2%). (B) t-SNE plot of K-means clusters from (A) split into the cells from control (CON) and CL-treated mice (CL).

mice identified eight major clusters varying from ~200 to 3200 cells per cluster (**Figure 3A**). A list of differentially-expressed genes (DEGs) that define the clusters are presented in **Supplementary Table S3A**. Analysis of DEGs identified four major clusters of ASCs (i.e., expressing *Pdgfra* and *Ly6a* or early adipocyte makers; clusters ASC 1, ASC 2, Diff. ASC, Pro. ASC), fibroblasts (FB), a population of vascular endothelial cells (VEC) and small populations (each < 3% of total) of natural killer T cells (NKT) and macrophages

(MAC) that likely escaped capture by the Lin+ MACS beads. Two major clusters of ASCs (ASC 1 and ASC 2; representing 32% and 27%, respectively) could be distinguished by overexpression of genes corresponding to regeneration (GO:0031099,  $p = 4.26E-5$ ), positive regulation of secretion by cell (GO:1903532,  $p = 2.06E-2$ ) and positive regulation by migration (GO:0030335,  $p = 3.63E-4$ ) in cluster ASC 1, and extracellular exosome (GO:0070062,  $p = 3.52E-4$ ) in cluster ASC 2.

Segregation of the aggregated t-SNE plot according to treatment condition (**Figure 3B**) demonstrated that CL treatment shifted the expression profiles of the major ASC subtypes (ASC 1 and ASC 2) and induced the appearance of two new clusters (Diff. ASC and Pro. ASC). Within cluster ASC 1, CL treatment altered expression of genes related to proteinaceous extracellular matrix (GO:0005578,  $p = 6.6E-7$ ), whereas in ASC 2, CL treatment strongly upregulated genes ( $> 2$ -fold,  $p < 1E-4$ ) involved in cell motility (GO:2000145,  $p = 5E-5$ ), migration (GO:0030334,  $7.5E-5$ ), and epithelial cell proliferation (GO:0050678,  $p = 7.7E-5$ ). As mentioned, ASC 1 and ASC 2 had an overall profile that likely represents different states of a similar cell type (i.e., ASC). In this regard, it is interesting to note that nearly all (20/24) of the genes that were significantly upregulated by CL in cluster ASC 1 were also upregulated in cluster ASC 2 (**Table S2B**).

The cells in cluster Pro. ASC exhibited very strong induction ( $>60$ -fold) of genes that positively regulate cell cycle, leaving no doubt that the cells were actively proliferating, whereas cluster Diff. ASC was highly enriched in expression of genes involved in early adipogenesis, including CAAT enhancer binding protein alpha (*Cebpa*), carbonic anhydrase 3 (*Car3*), acylglycerol-3-phosphate O-acyltransferase 2 (*Agpat2*), diacylglycerol acyltransferase 2 (*Dgat2*), perilipin 1 (*Plin1*), and adiponectin (*Adipoq*)

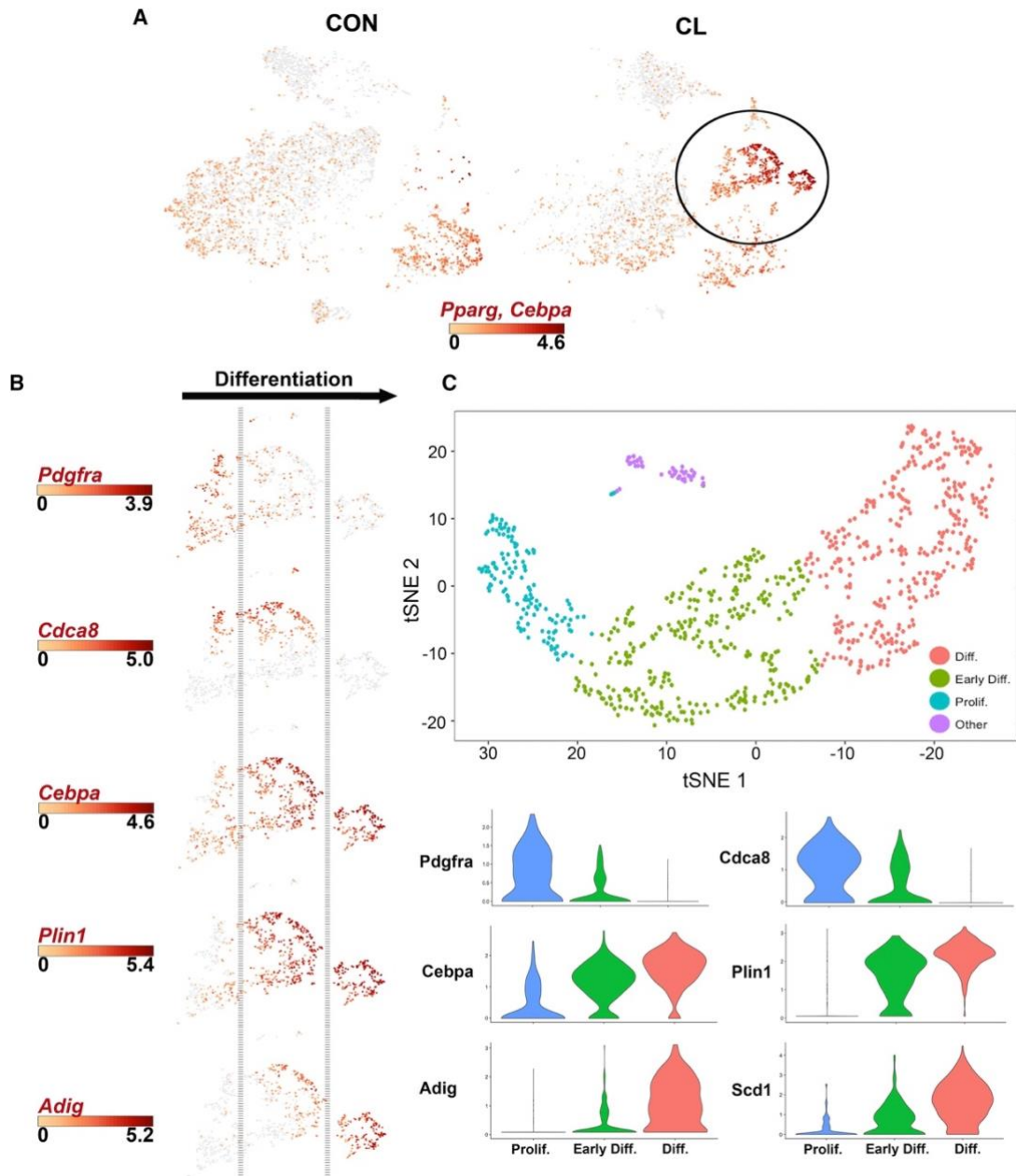


**Figure 4. scRNA-seq of Mouse eWAT Maps an Adipogenic Differentiation Trajectory during CL Treatment** (A) Gene expression profiles of master regulators of adipogenesis, *Pparg* and *Cebpa*, in eWAT Lin<sup>-</sup> cells from CON- and CL-treated mice. Circled are clusters Diff. ASC and Pro. ASC, which appear following CL treatment and are examined further in (B) and (C). Scale bar represents the log<sub>2</sub> values of combined max gene expression. (B) Expression profiles of genes known to be involved in adipogenesis reveals a differentiation trajectory. Expression scale bars show log<sub>2</sub> values of max gene expression. (C) t-SNE plot and shared nearest neighbor clustering of Diff. ASC and Pro. ASC clusters from Figure 3A using Seurat. Independent clustering of these cells in Seurat ordered cells along a differentiation trajectory that could be defined by expression of genes in (B). Violin plots showing the mean and variance expression density in Prolif., Early Diff., and Diff. clusters for the following genes: *Pdgfra*, *Cdca8*, *Cebpa*, *Plin1*, *Adig*, and *Scd1*. Gene expression profiles corroborate the differentiation trajectory defined in (B). The complete list of DEGs that define these clusters is presented in Supplementary Table S3C.



(**Supplementary Table S3A**). Together, the clusters Diff. ASC and Pro. ASC contained ~10% of total putative ASC (the sum of clusters ASC 1, ASC 2, Diff. ASC and Pro. ASC) from CL-treated mice, and fewer than 0.6% of ASC from control mice.

CL treatment induces a burst of adipogenesis that peaks on the third day of treatment [110]. Thus, following 3 days of CL treatment, we expected to observe ASCs in different stages of adipogenesis within clusters Diff. ASC and Pro. ASC from which a differentiation trajectory might be mapped. Expression of the adipogenic master regulators *Cebpa* and peroxisome proliferator activated receptor gamma (*Pparg*) was upregulated in these clusters (circled in **Figure 4A**) and paralleled expression of adipocyte genes (expanded in **Figure 4B**). Within this overall pathway, we observed cells that expressed *Pdgfra* and were actively dividing (*Cdca8*), yet had relatively low levels of *Cebpa* and virtually no expression of adipocyte differentiation markers *Plin1* and adipogenin (*Adig*) (**Figure 4B**). Next, we identified actively dividing cells in which *Pdgfra* was suppressed, while *Cebpa* and *Plin1* were upregulated, but levels of *Adig* remained relatively low. Lastly, we observed cells in which both *Pdgfra* and *Cdca8* were silenced, and *Cebpa*, *Plin1* and *Adig* were strongly upregulated. Importantly, the trajectory of proliferation and differentiation deduced from a single time point (3 days) is entirely consistent with that determined from extensive time course analyses with genetic tracers [50, 110].

To investigate the putative adipogenic trajectory further, we performed shared nearest neighbor clustering of proliferating and differentiating cells (Diff. ASC + Pro. ASC from **Figure 3A**) using the single cell R tool kit Seurat [111]. This analysis identified three major clusters that could be mapped to a differentiation trajectory of stem cell proliferation,

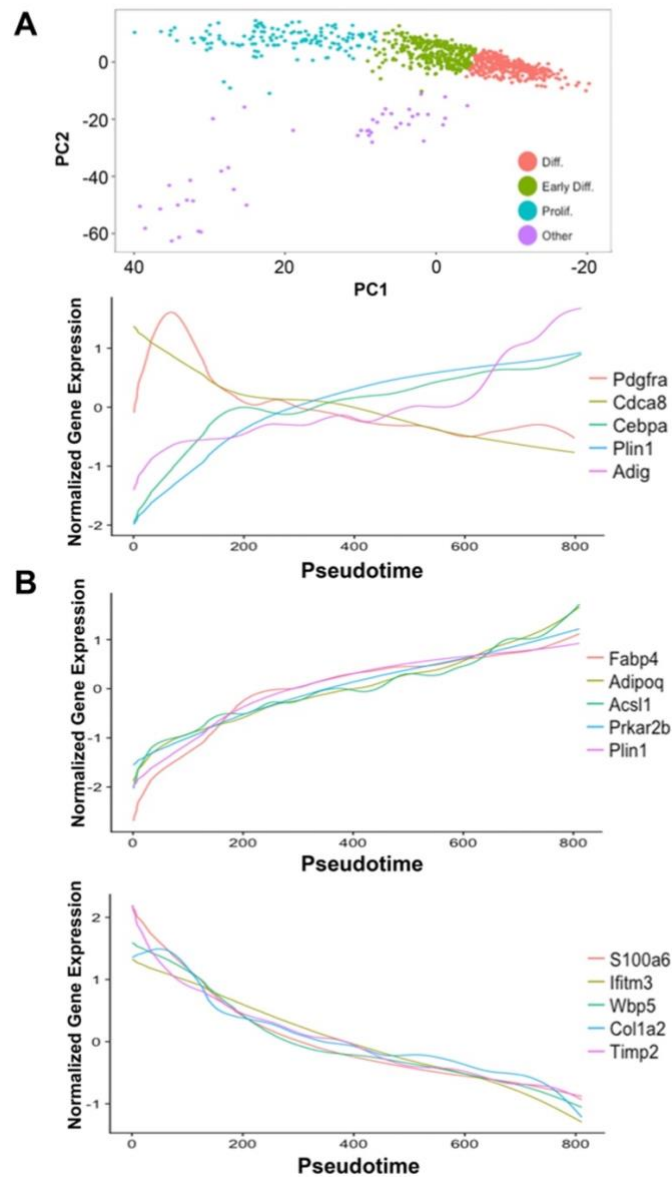


**Figure 5. Pseudotime analysis of proliferating/differentiating cells** Related to Figure 4C. (A) PCA plot of the first two principal components reveals that principal component 1 (PC1) orders cells along the differentiation trajectory, and can therefore be used as a surrogate for ordering cells in pseudotime. Plotting pseudotime versus normalized gene expression for the genes in Figure 4B follows an expected pattern for adipocyte differentiation. These genes were significantly correlated with pseudotime analysis: *Pdgfra* ( $r = -0.46$ ), *Cdca8* ( $r = -0.53$ ), *Cebpa* ( $r = 0.57$ ), *Plin1* ( $r = 0.74$ ), and *Adig* ( $r = 0.62$ ). (B) Genes whose expression was correlated with pseudotime using a Pearson correlation were determined. Shown are the top 5 positively and negatively correlated genes from this analysis. Positively correlated: *Fabp4* ( $r = 0.79$ ), *Adipoq* ( $r = 0.79$ ), *Acsl1* ( $r = 0.74$ ), *Prkar2b* ( $r = 0.74$ ), and *Plin1* ( $r = 0.74$ ). Negatively correlated: *S100a6* ( $r = -0.72$ ), *Ifitm3* ( $r = -0.72$ ), *Wbp5* ( $r = -0.68$ ), *Col1a2* ( $r = -0.66$ ), and *Timp2* ( $r = -0.66$ ). All genes significantly correlated with the pseudotime analysis are presented in Supplementary Table S3D.

early adipogenic differentiation, and late differentiation (**Figure 4C and Table S2C**). We used the first principal component (PC1) of these expression data as a surrogate for pseudotime to order cells along the differentiation trajectory (**Figure 5A**). Plotting the expression of representative adipogenesis genes against pseudotime revealed a clear differentiation trajectory (**Figure 5A**). To expand this analysis, we correlated normalized gene expression of the single cells with the pseudotime trajectory and identified 241 genes that significantly covaried ( $r^2 > 0.2$ ,  $p < 10E-20$ ) with the proposed differentiation trajectory (**Figure 5B and Table S2D**). Examples of genes that correlated positively with the adipogenic trajectory include adipogenic master regulators (*Cepba*, *Pparg*), and those involved in lipid synthesis (*Fabp4*, *Acs11*, *Lpin1*), electron transport (*Atp5b*, *Cox8a*, *Ndufab1*) and signal transduction (*Pkar2b*, *Mrap*, *Reep6*). Genes that were suppressed during differentiation included proliferation genes (*Mki67*, *Cenpf*), certain ECM genes (*Timp2*, *Col1a1*, *S100A6*) and ASC markers (*CD34*, *Dcn*, *Pdgfra*).

Single-cell expression profiling supports the concept that ASCs can exist in various metastable states that can be perturbed toward adipogenic or nonadipogenic fates [110, 112, 113]. From this perspective, a single type of progenitor is unlikely to exist, as most cells have adipogenic potential that is realized by the proper set of local cues. Consistent with this notion, we identified a subpopulation of ASCs within cluster ASC 1 having an expression profile that overlapped with cells adipogenic clusters (Diff. ASC and Pro. ASC). This population of stromal cells, which expanded following CL treatment, upregulated genes such as *Cxcl12*, *Igf1*, *Adam12* and *Sfrp1* that are involved in cell migration [114, 115], proliferation [116], ECM remodeling [117], and induction of adipogenesis [118, 119], respectively (**Figure 6A**). An interesting feature of the total

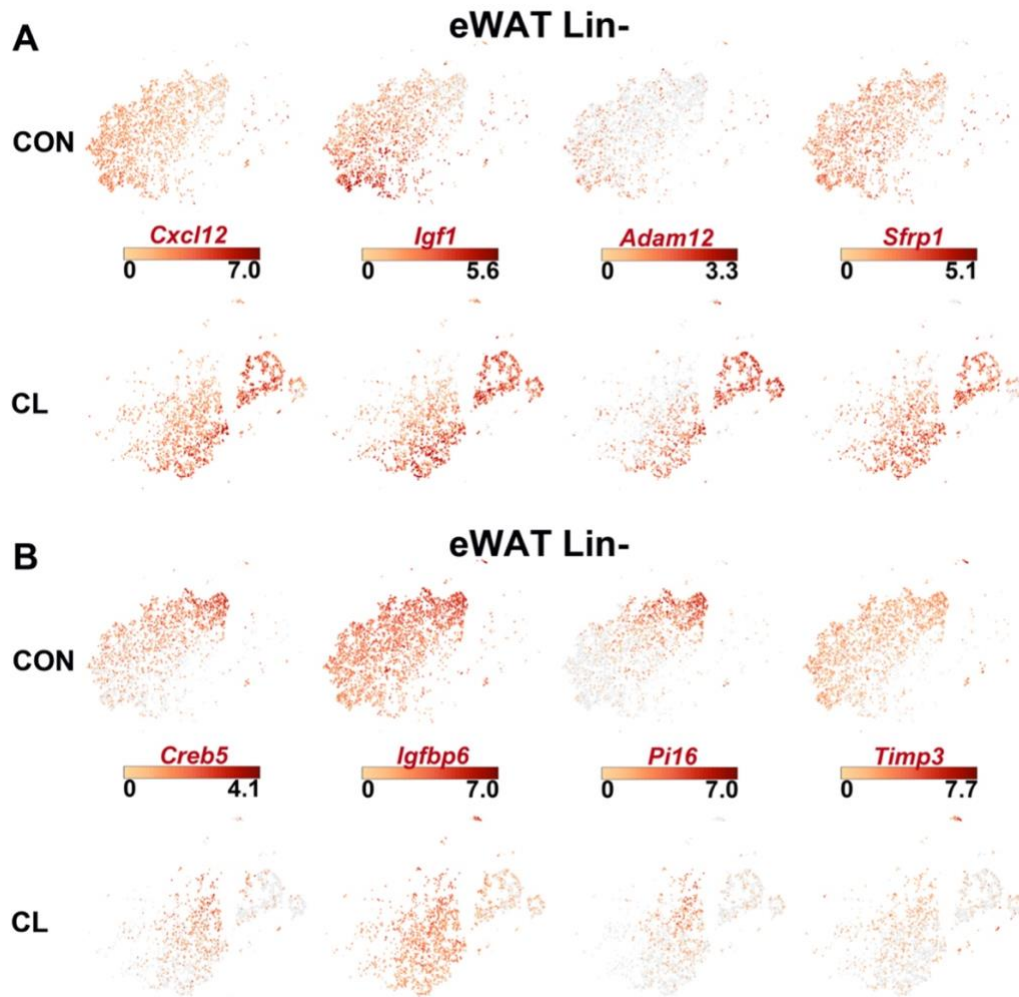


**Figure 6. CL treatment upregulates expression of genes involved in cell migration, proliferation, and ECM remodeling in eWAT adipocyte stem cells** Related to Figures 3 and 4. t-SNE plots show the ASC populations defined in Figure 3A, segregated by treatment condition. (A) CL upregulates expression of *Cxcl12*, *Igf1*, *Adam12*, and *Sfrp1* and (B) downregulates expression of *Creb5*, *Igfbp6*, *Pi16*, and *Timp3*. Expression scale bars show Log<sub>2</sub> values of max gene expression.

adipogenic trajectory is the pronounced upregulation of genes involved in migration and ECM remodeling and down regulation of certain ECM protease inhibitors. For example, CL treatment sharply downregulated expression of the protease inhibitors *Pi16* and *Timp3*, which were not expressed in cells undergoing division and differentiation (Figure 6B). The reciprocal expression of extracellular activators and inhibitors (e.g.,

*Igf1/Igfbp6* and *Adam12/Timp3*) suggest functional interactions in the adipogenic microenvironment. In this regard, it is known that induction of adipogenesis in cell culture models involves dramatic alterations in ECM proteins and cell shape, which are necessary and sometimes sufficient to drive the adipogenic program [117, 120, 121]. The expression of certain genes, including *Pdgfra* [110], *Pdgfrb* [122], smooth muscle actin (*Acta2*) [123] and VE-cadherin (*Cdh5*) [124], has been used to tag and trace ASC differentiation *in vivo*. It was therefore of interest to compare the expression pattern of these genes with the adipogenic trajectories defined above. To include all of stromal cell types in eWAT, we aggregated Lin<sup>+</sup> and Lin<sup>-</sup> cell fractions from control and CL-treated mice (17,640 cells), generated a t-SNE plot, and performed K-means clustering analysis (**Figure 7 and Supplementary Table S3E**). As observed with the Lin<sup>-</sup> pool, cells expressing *Pdgfra* strongly contributed to adipogenic trajectories (e.g., *Plin1*, *Dgat2*, *Adrb3*, *Ucp1*). Furthermore, the t-SNE plot that includes all stromal cells clearly identified an adipogenic trajectory involving proliferation and differentiation (**Figure 8**). *Pdgfrb* was co-expressed with *Pdgfra* in ASC, as well as in a population of VEC (**Figure 7**). *Cdh5* and *Acta2* were heavily expressed in VEC and VSMC, respectively, as expected. However, unlike *Pdgfra*, the transcription profiles of cells expressing *Cdh5* or *Acta2* were largely, if not completely, unrelated to cells undergoing CL-induced adipogenesis. These data do not exclude adipogenic recruitment from other cell types under different conditions (e.g., development), and suggest that single-cell approaches might be useful in defining the range of cell types that contribute to tissue plasticity under various conditions.

Overall, data from bulk RNA-sequencing of FACS-sorted PDFGRA<sup>+</sup> cells were

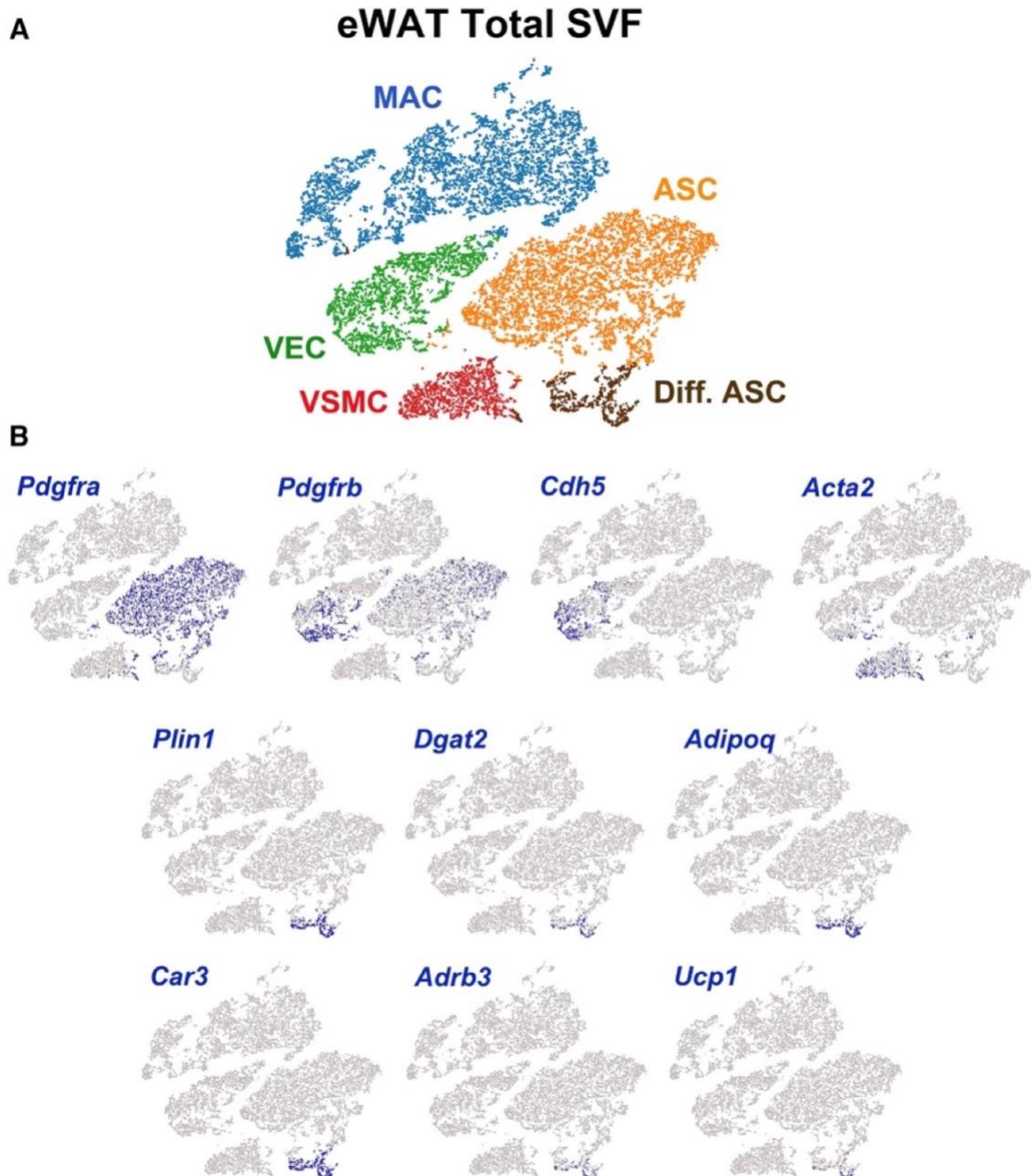


**Figure 7. scRNA-Seq Analysis of Aggregated eWAT Lin<sup>+</sup> and Lin<sup>-</sup> Cells from Control and CL-Treated Mice** t-SNE plots represent the total population of stromal vascular cells from eWAT. (A) A total of 17,640 cells from Lin<sup>+</sup> and Lin<sup>-</sup> libraries of CON and CL-treated mice were clustered by K-means (five clusters) and projected onto a t-SNE plot to define general cell types. MAC, macrophages; VEC, vascular endothelial cells; VSMC, vascular smooth muscle cells; ASC, adipocyte stem cells; Diff. ASC, differentiating adipocyte stem cells. Cell types were identified by the DEGs in each cluster (Supplementary Table S3E). Cell counts by cluster: MAC = 6,600 (37%), VEC = 2,675 (15%), VSMC = 1,489 (8%), ASC = 6,011 (34%), Dif. ASC = 865 (5%). (B) The dataset was queried for cells expressing selected ASC marker genes, as well as cells expressing early and late markers of adipocytes. Highlighted cells express the given gene above the following thresholds: *Pdgfra* > 1; *Pdgfrb* > 1; *Cdh5* > 3; *Acta2* > 2; *Plin1* > 3; *Dgat2* > 3; *Adipoq* > 4; *Car3* > 7; *Adrb3* > 2; *Ucp1* > 1. Expression values are log<sub>2</sub> values of max gene expression.

highly consistent with data culled from single PDGFRA+ cells (**Figure 9** and **Supplementary Tables S2 and S3A**). Thus, CL treatment sharply upregulated ECM proteases, downregulated protease inhibitors, and induced early adipogenic genes.

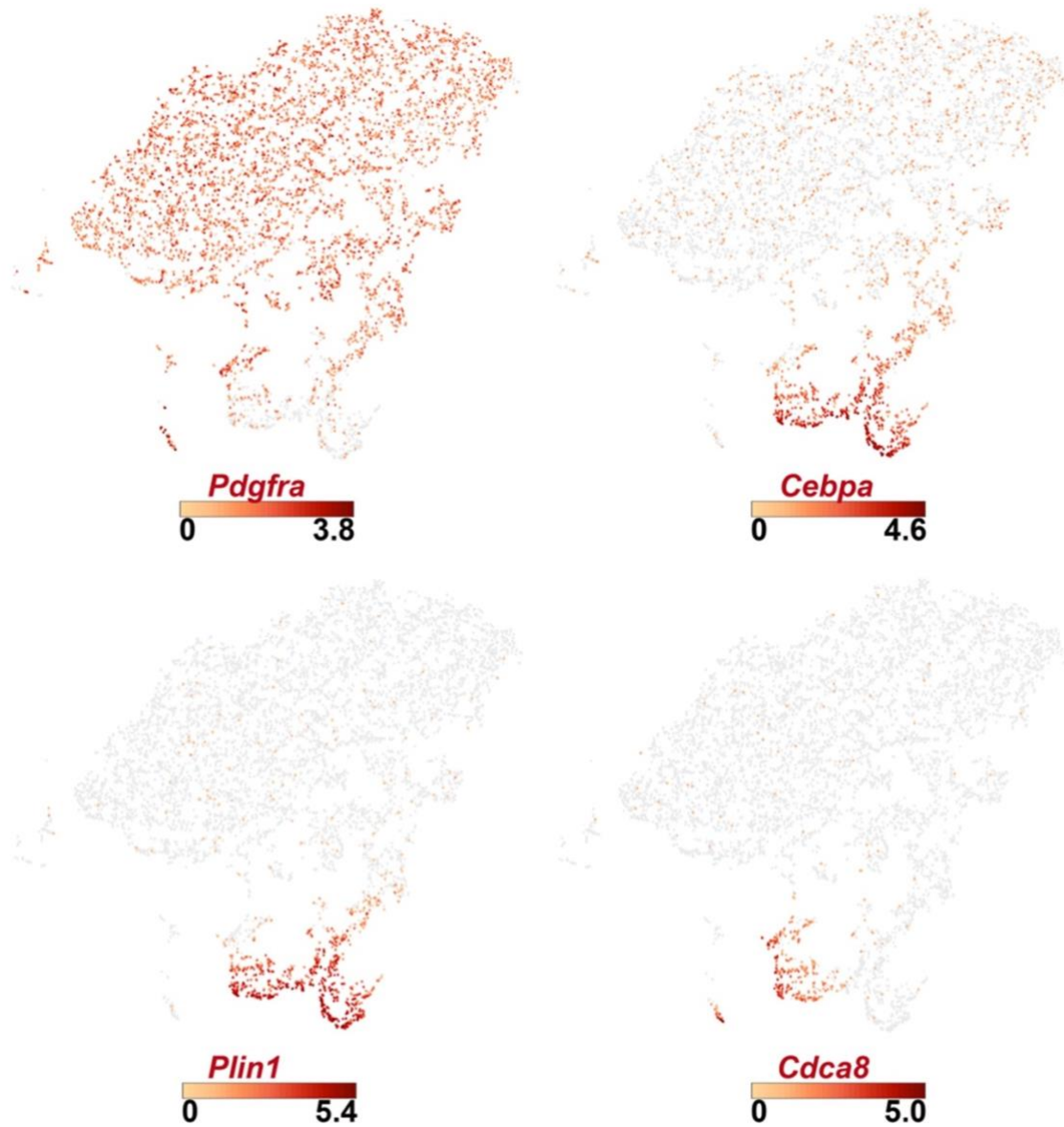


**Figure 8. Expression patterns of adipogenic/proliferation genes in ASC from aggregate Lin+ and Lin- fractions identifies proliferating and differentiating ASCs** Related to Figure 7. t-SNE plot of clusters ASC and Diff. ASC from Figure 3A. Expression of *Pdgfra* defines ASC. Expression of *Cebpa* and *Plin1* map to population defined in Figure 3A as differentiating ASC. *Cdca8* defines actively proliferating ASC. Expression scale bars represent Log<sub>2</sub> values of max gene expression.

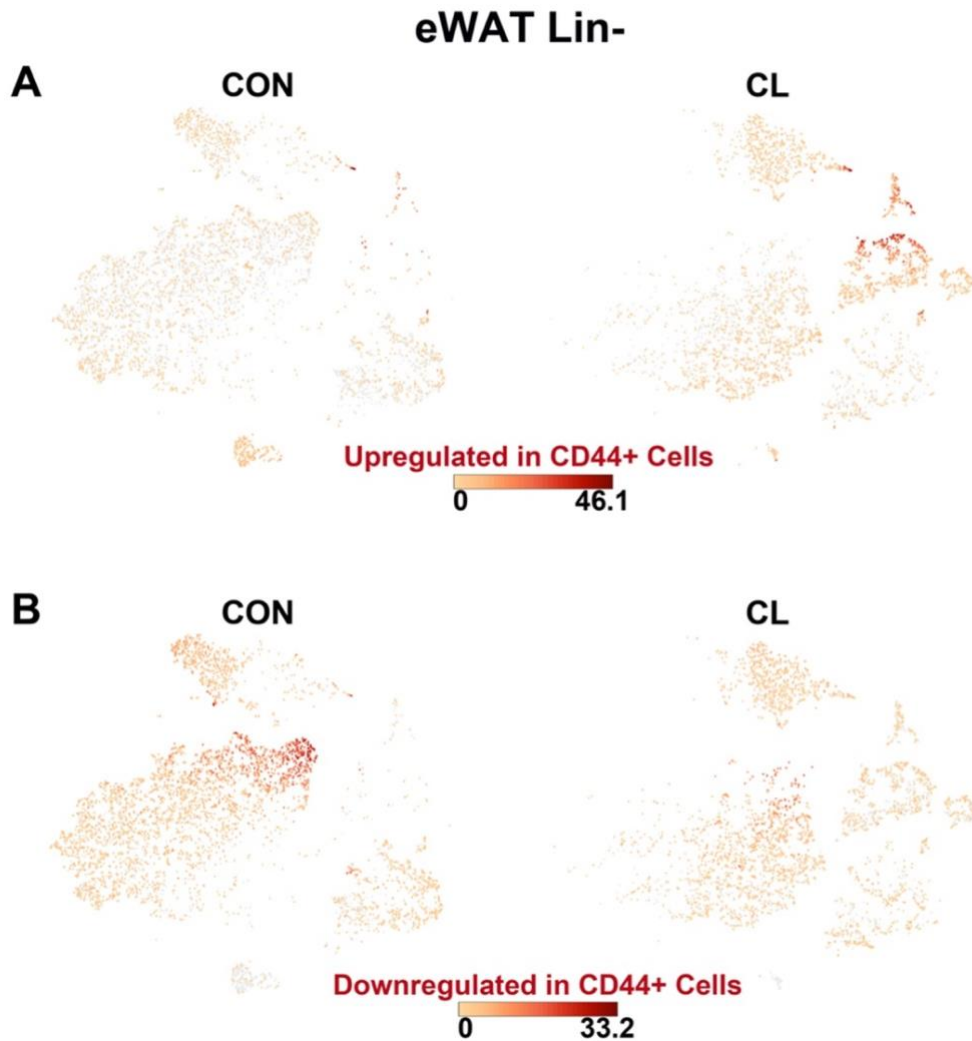


**Figure 9. Correspondence of DEGs identified by bulk RNA-sequencing of FACS sorted PDGFRA+CD44+ cells to scRNA-seq** Related to Figures 2 and 3. Lists of the top 25 upregulated or downregulated genes identified from bulk RNA sequencing of PDGFRA+CD44+ cells compared to PDGFRA+CD44- cells were used as input into the 10X Genomics Loupe program. Shown are the t-SNE plots of the eWAT Lin- cell fraction segregated by treatment (CON or CL), also shown in Figure 3B. Color intensities represent the sum of the Log2 expression values for the input gene list. (A) Differentially upregulated genes in PDGFRA+CD44+ cells are enriched with CL treatment and expressed in cells undergoing active adipogenesis. (B) Differentially downregulated genes in PDGFRA+CD44+ cells are reduced in adipogenic clusters that were induced by CL.

Furthermore, the top upregulated DEGs in the PDGFRA+CD44+ bulk RNA-seq were enriched in the adipogenic clusters defined by scRNA-seq (**Figure 9A and Supplementary Tables S2 and S3A**), providing cross validation of the single-cell approach. Importantly, scRNA-seq provided far higher resolution of the adipogenic



trajectory. For example, scRNA-seq detected 19 cell proliferation genes whose expression was enriched an average of 27-fold in cluster Pro. ASC (**Supplementary Table S3A**). In contrast, fewer than half of these genes were found to be significantly upregulated in FACS-isolated PDGFRA<sup>+</sup>CD44<sup>+</sup>, with an average increase of less than 5-fold (**Supplementary Tables S2 and S3A**). Similarly, scRNA-seq identified numerous adipogenesis-related genes (e.g., *Adig*, *Lipe*, *Agpat2*, *Dgat1* and *Dgat2*) that were not detected as being differentially expressed in bulk RNA-seq. The inability to detect late differentiation markers in the FACS-based approach may reflect the fact that PDGFRA expression is lost as ASC differentiate [110]. Thus, since scRNA-seq is unbiased with respect to surface marker expression, it allows detection of the full range of ASC activation and differentiation. For example, scRNA-seq allowed the clear demonstration that ASC can upregulate the adipocyte gene program while proliferating and that proliferation and differentiation are not mutually exclusive [110, 125, 126]. In general, although bulk RNA-seq identified more genes (i.e., greater depth), it was far less sensitive to differential expression in critical subpopulations and incapable of mapping differentiation trajectories.

### **3.3 scRNA-seq analysis demonstrates dynamic regulation of macrophage populations and suggests functional interactions with activated progenitors**

As mentioned above, ADRB3-induced *de novo* adipogenesis requires the clearance of dead white adipocytes by tissue macrophages, which recruit ASC to the site of efferocytosis and guide their proliferation and differentiation into new BA [50]. To gain further insights into the immune cells involved, we performed scRNA-seq of Lin<sup>+</sup> cells isolated from eWAT of control and CL-treated mice. scRNA-seq identified prominent

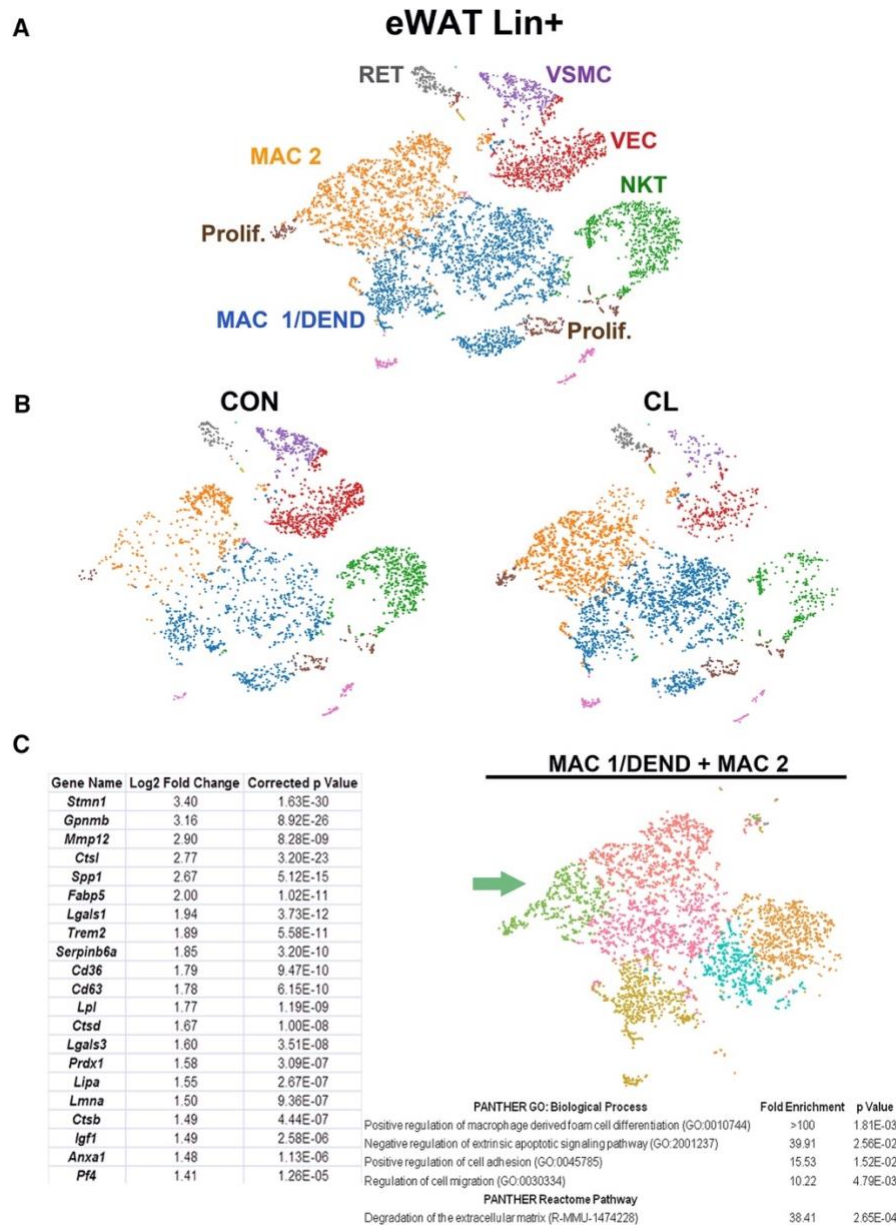


**Figure 10. scRNA-Seq Analysis of Lin+ eWAT Stromal Cells of Control and CL-Treated Mice** (A) t-SNE plot of 7,725 lineage marker-positive (Lin+) cells isolated from eWAT of control and CL-treated mice. K-means clustering applied to the t-SNE identified eight major cell types/states: RET, reticulocytes; VSMC, vascular smooth muscle cells; VEC, vascular endothelial cells; NKT, natural killer T cells; MAC, macrophages; DEND, dendritic cells; Prolif., cells undergoing active proliferation. Cell types/states were determined by DEGs within each cluster, the complete list of which is presented in Supplementary Table S3F. Cell counts by cluster: MAC 1/DEND = 2,725 (35%), MAC 2 = 1,781 (23%), NKT = 1,018 (13%), VEC = 976 (13%), VSMC = 384 (5%), Prolif. = 376 (5%), RET = 200 (3%). (B) t-SNE plot of K-means clusters segregated by treatment (CON or CL). CL treatment increased the relative abundance of macrophages. (C) An alternative method of clustering, graph-based clustering, was applied to the t-SNE plot of Lin+ cells and identified six macrophage clusters. Gene expression comparisons were made among the clusters. Shown are DEGs and corresponding gene ontologies (GO) of the subcluster of macrophages in green that were associated with proliferation.

clusters of macrophages/dendritic cells (MAC 1/DEND and MAC 2), natural killer T cells (NKT), vascular endothelial cells (VEC), vascular smooth muscle cells (VSMC), and a small population (< 3%) of reticulocytes (**Figure 10A and Supplementary Table S3F**). K-means clustering also identified small clusters of proliferating (Prolif.) cells that were closely associated with clusters of NKT cells and macrophage/dendritic cells. As expected, CL increased the number of macrophages in clusters MAC 1/DEND and MAC 2 by 1.9- and 2.7-fold, respectively (chi square,  $p < 0.00001$ ) (**Figure 10B**). CL treatment significantly reduced the number of NKT cells (chi square,  $p < 0.00001$ ), without significantly shifting their transcriptional profile (**Figure 10B and Supplementary Table S3F**).

Previous analysis of whole tissue mRNA indicated that ADRB3 stimulation increases expression of M2 markers such as *Chil3*, *Clec10a*, and *Arg1* [50, 127]. Surprisingly, scRNA-seq indicated that these markers often segregate into different subpopulations, suggesting a spectrum of activation states (**Figure 11**) that defy simple classification into M2 or M1 phenotypes [128]. Published histological analysis of ADRB3-induced remodeling demonstrated that ASC are recruited to the site of macrophage-mediated efferocytosis [50]. Furthermore, the macrophages involved in clearing dead fat cells resemble foam cells [129, 130], proliferate within the ‘crown-like structure’, express high levels of osteopontin (*Spp1*; a chemoattractant for ASC), and likely upregulate genes involved lipid uptake and metabolism [50, 108, 110, 131]. Graph-based clustering of the macrophage populations MAC 1/DEND and MAC 2 identified a subpopulation (**Figure 10C, green**) that likely resides in the adipogenic niche. Consistent with previous histological and FACS analyses [50, 108-110], expression of *Spp1* was greatly enriched

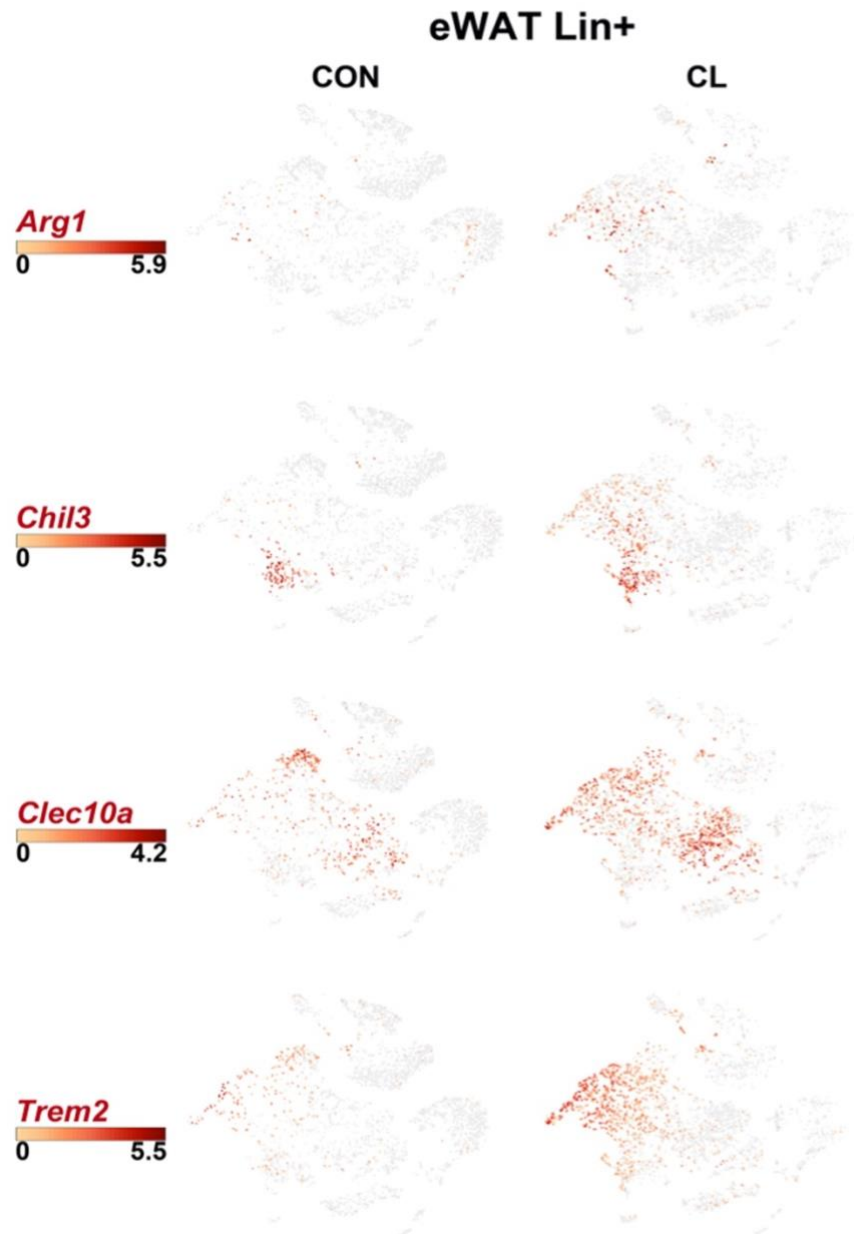


**Figure 11. Expression of M2 macrophage markers in scRNA-seq** Related to Figure 10. Distribution of M2 markers, previously shown to be upregulated by CL, on the t-SNE plot of eWAT Lin+ cells from Figure 10. Scale bars represent Log<sub>2</sub> values of maximum gene expression.

in this green cluster (table, **Figure 10C**), and this cluster also contains cells identified in panel A as proliferating, indicating that local proliferation contributes to this population. Compared to other macrophage subpopulations, these cells upregulated expression of

genes involved in lipid uptake and metabolism (*Cd36*, *Fabp5*, *Lpl*, *Lipa*), and ECM remodeling and proteolysis (*Mmp12*, *Ctsl*, *Ctsd*) that might be involved in the removal of dead fat cells, and in providing arriving ASC with growth factors (e.g., IGF1 [132] and lipid-derived signaling molecules [108]) (**Figure 10C**). Consistently, the genes that were overexpressed in this subpopulation are significantly associated with the biological processes of migration, adhesion, and macrophage foam cell differentiation (**Figure 10C**). Overall, scRNA expression profiles provide new insights into the adipogenic niche, and suggests that synergistic and highly localized remodeling of ECM drives cell migration, proliferation, and generation of protein and lipid mediators that guide ASC differentiation.

### **3.4 ADRB3 activation for three days produces minimal de novo adipogenesis from stromal cells in inguinal WAT**

ADRB3 activation also induces the appearance of BA in subcutaneous inguinal WAT (iWAT). Genetic tracing experiments performed in our lab indicate that few, if any, of these cells are derived from cell proliferation or from cells expressing PDGFRA. Furthermore, results from our lab and others [37, 52, 133, 134] indicate that a substantial number of BA in iWAT can be derived from existing fat cells that appear white under basal conditions, yet can adopt a brown phenotype following ADRB3 stimulation.

scRNA-seq analysis of Lin<sup>-</sup> cells from iWAT from control and CL-treated mice identified two major clusters of ASCs (i.e., cells expressing *Pdgfra* and *Ly6a/Sca1*) (**Figure 12A and Supplementary Table S4**) that could be readily distinguished by DEGs involved in ECM production and proteolysis (**Figure 12B**). Interestingly, these clusters also differentially expressed the adipogenesis markers caveolin-1 (*Cav1*) and G0/G1

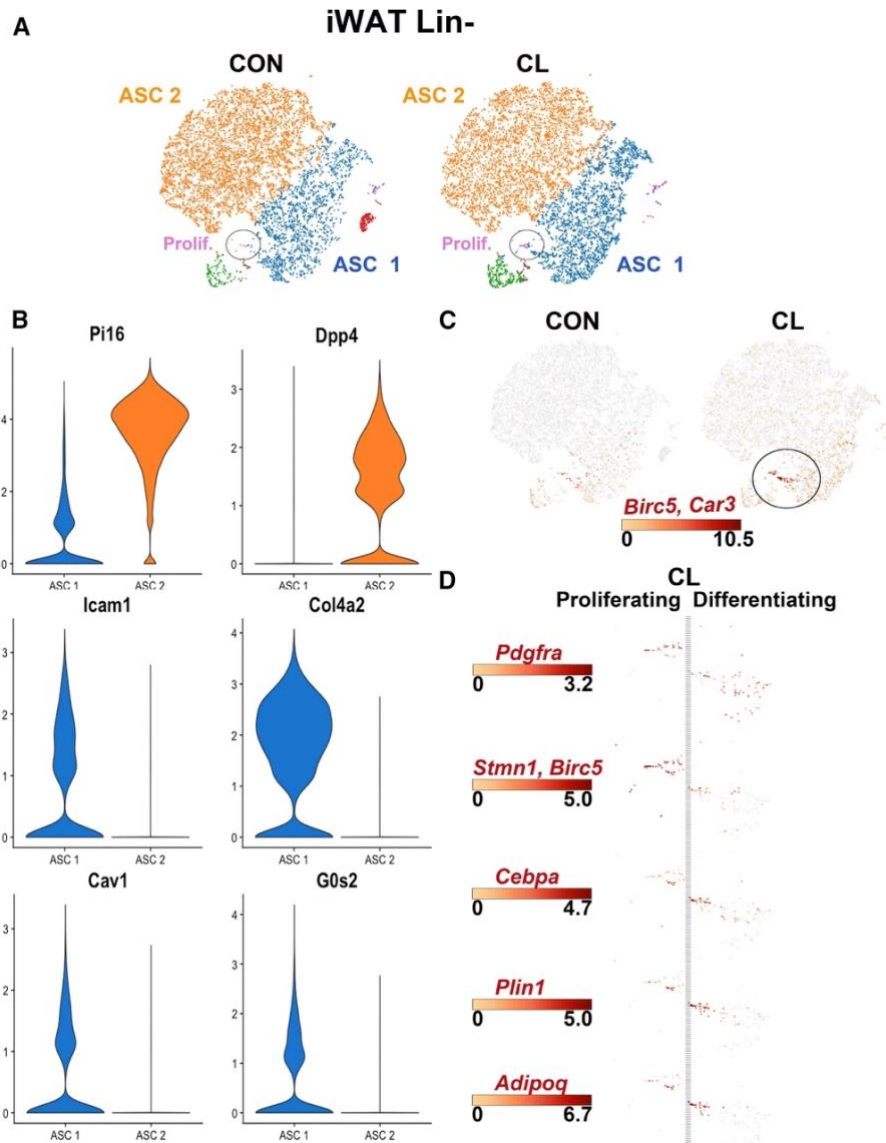


**Figure 12. scRNA-Seq of ASCs from iWAT of Control and CL-Treated Mice** (A) t-SNE plots of a combined 16,023 cells isolated from inguinal white adipose tissue (iWAT) of control and mice treated with CL for 3 days. K-means clustering defined seven main clusters, which are segregated by treatment condition (CON or CL). Clusters ASC 1 and ASC 2 comprise the majority of the cell types and are distinguished from each other by differential expression of genes associated with ECM production and turnover (the list of cluster-defining DEGs is given in Supplementary Table S4). Circled are cells belonging to the cluster, Prolif., which are cells undergoing active proliferation and are examined further in (C) and (D). ASC, adipocyte stem cells. Cell counts by cluster: ASC 1 = 5,198 (32%), ASC 2 = 9,700 (61%), Prolif. = 66 (0.4%). (B) Violin plots showing the mean and variance expression density of the following genes in iWAT ASC 1 and ASC 2: *Pi16*, *Dpp4*, *Icam1*, and *Col4a2*. Expression profiles of *Pi16* and *Dpp4*, and *Icam1* and *Col4a2* show a striking demarcation of clusters ASC 1 and ASC 2. Differential expression of *Cav1* and *G0s2* suggests that cluster ASC 1 is more poised for adipogenesis. (C) Expression profiles of *Birc5* (proliferation) and *Car3* (adipogenesis) identified very few cells within an adipogenic trajectory. (D) Expression profiles of genes involved in adipocyte proliferation and differentiation. Scale bars denote maximum log<sub>2</sub> expression values for each gene.

switch 2 (*G0s2*) (**Figure 12B**), suggesting that ASC 1 is more poised for adipogenic differentiation. Compared to eWAT, CL treatment upregulated relatively few genes in either ASC 1 or 2, consistent with negligible recruitment from ASC. However, K-means clustering identified a small population of proliferating cells (labeled Prolif. and circled in **Figure 12A and Supplementary Table S4**) whose numbers were significantly increased by CL treatment (52 vs 8; chi square,  $p < 0.0001$ ). Examination of gene expression profiles in this region identified cells from CL-treated mice with overlapping expression of markers of proliferation (*Birc5*) and early adipogenesis (*Car3*) (circled in **Figure 12C**), indicating an adipogenic trajectory involving proliferation and upregulation of *Cebpa*, *Plin1*, and *Adipoq* (**Figure 12D**). These cells also exhibited upregulation of *Pparg*, fatty acid binding protein 4 (*Fabp4*), *Fabp5* and *G0s2*, which were also strongly induced in differentiating ASC in eWAT. Overall, proliferating/differentiating ASCs in iWAT represented about 0.4% and 1.5% of total ASC from control and CL-treated mice, respectively. Interestingly, the overall pattern of gene expression in these proliferating/differentiating cells was most similar to cluster ASC 1 and distinct from those in cluster ASC 2, consistent with the concept that distinct populations of ASC are differentially poised to enter the adipogenic pathway. These data demonstrate the power of scRNA to identify very small numbers of proliferating/differentiating cells that might be missed in bulk RNA profiling and histological analysis.

### **3.5 Similarities and differences between ASC of eWAT and iWAT**

To directly compare the transcriptional profiles of ASC populations in eWAT and iWAT, control scRNA-seq libraries from both depots were aggregated. Control ASC from eWAT and iWAT fell into two major clusters (ASC 1 and ASC 2) following K-means

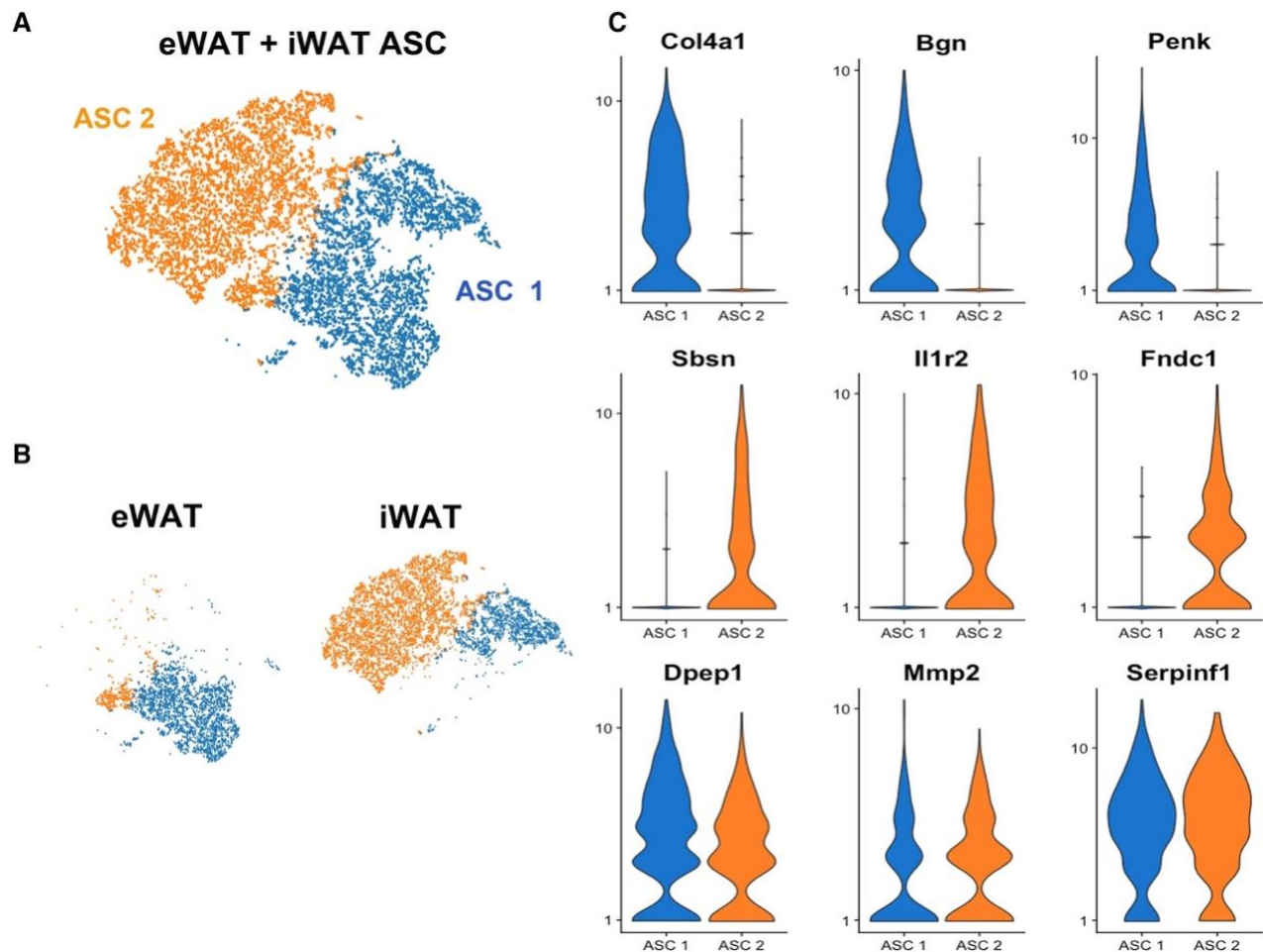


**Figure 13. Comparison of ASCs from eWAT and iWAT** (A) t-SNE plot of combined Lin<sup>-</sup> cells from eWAT and iWAT of control mice, showing only the adipocyte stem cells. K-means clustering identified two main clusters labeled ASC 1 and ASC 2. ASC, adipocyte stem cells. Cell counts by cluster: ASC 1 = 5,058 (45%), ASC 2 = 6,071 (55%). (B) Segregating libraries by depot indicates distinct expression profiles of ASCs from iWAT and eWAT. (C) Violin plots showing the mean and variance of gene expression in ASC 1 and ASC 2 for *Col4a1*, *Bgn*, *Penk*, *Sbsn*, *Il1r2*, *Fndc1*, *Dpep1*, *Mmp2*, and *Serpinf1*. Gene expression profiles illustrate differences and similarities between depots and among ASC subpopulations. Expression of *Col4a1*, *Bgn*, and *Penk* have higher expression in ASCs from eWAT, while *Sbsn*, *Il1r2*, and *Fndc1* are expressed in ASCs from iWAT. However, some genes, such as *Dpep1*, *Mmp2*, and *Serpinf1*, are expressed in all ASCs. The complete list of DEGs that define ASC 1 and ASC 2 is presented in Supplementary Table S5.

clustering (**Figure 13A and Supplementary Table S5**). By splitting these clusters according to depot, it becomes clear that the pattern of gene expression reflects the source of ASC (**Figure 13B**). Results of K-means clustering indicates that the vast majority of ACS from eWAT have transcriptional profiles more similar to ASC 1 than ASC

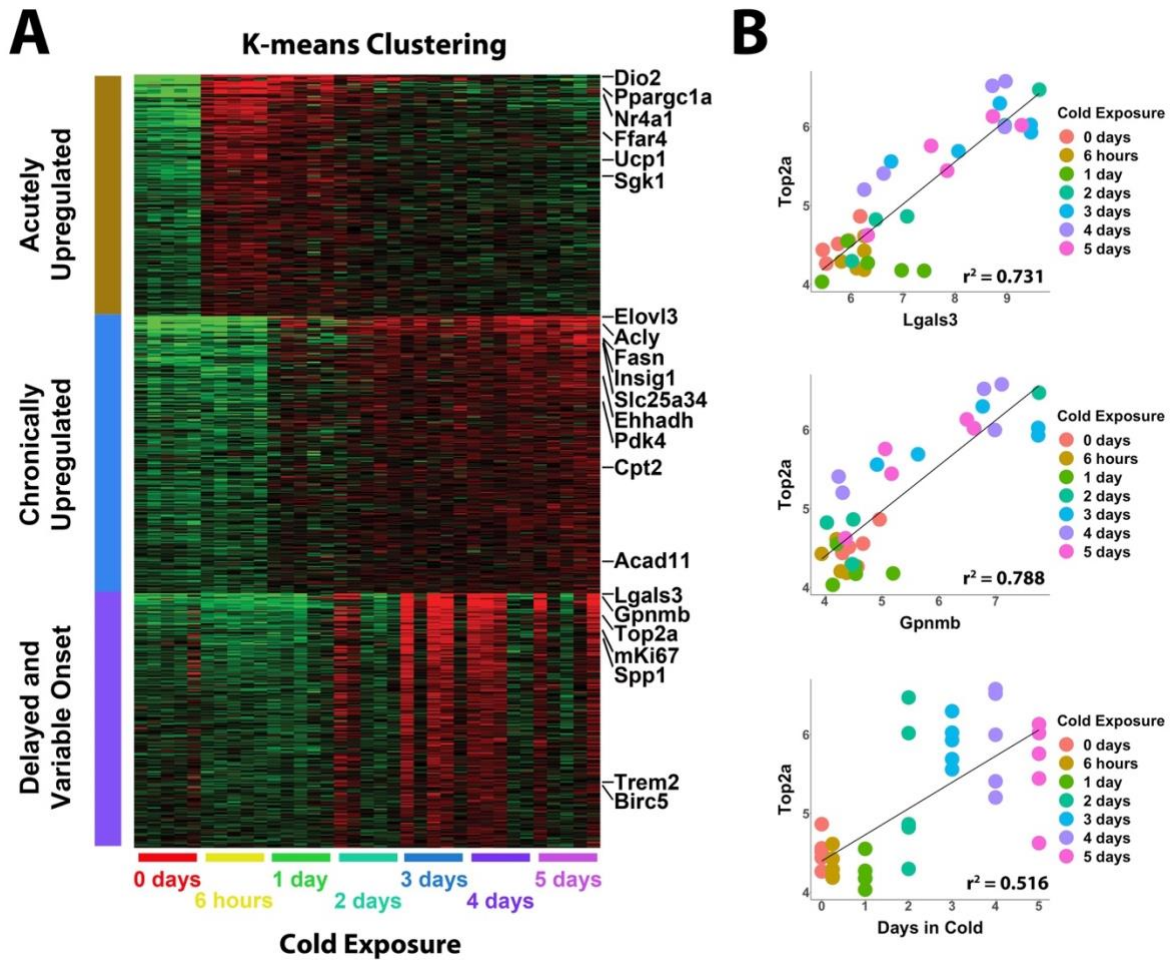


2; while both ASC clusters are found each depot, the position of these ASC populations in the tSNE plot indicates clear depot-selective differences within ASC clusters. Depot-specific differences could be evaluated by refined clustering or by identifying DEGs between depots using the lasso utility in the Loupe™ Cell Browser software. Comparing gene expression profiles between ASC 1 and ASC 2, we found genes specific to each cluster, but there were also genes that are common to both clusters (**Figure 13C**). As expected, the adipogenic transcription factors *Cebpa* and *Pparg* are sporadically expressed in ACS. Nonetheless, 12% and 14% of cells in cluster ASC 1 expressed *Cebpa* and *Pparg*, respectively, compared to 1.8% and 4.0% in ASC 2 (chi square,  $p < 0.00001$ ). Together, these observations indicate that the two major populations of ASC in iWAT and eWAT could be differentially primed for adipogenesis and is consistent with previous studies that used *Pparg*-driven Cre recombinase to trace subpopulations of adipogenic stromal cells [135]. That is not to say, however, that cells within ASC 2 are incapable of adipogenesis. In this regard, we note that the vast majority of genes detected in *Pdgfra*<sup>+</sup>*Ly6a*/*Sca1*<sup>+</sup> ASCs are not differentially expressed. We hypothesize that the clusters represent different states wherein certain stimuli in the microenvironment drive cells closer to an adipogenic phenotype. Thus, in cluster ASC 2 of eWAT, CL treatment greatly reduced expression of *Pi16*, *Ackr3*, *Anxa3*, *Cd55*, and *Igfbp6*, and upregulated expression of proadipogenic factors *Igf1*, *Sfrp1*, and *Adam12* (**Figure 6**).

## Chapter 4. Deconstructing cold-induced neogenesis in classic brown adipose tissue

### 4.1 RNA-seq analysis of mouse iBAT during cold exposure time course reveals activation of immune cells that correlates with proliferation

To gain insight into the timing of cold-induced iBAT neogenesis, we first sequenced total tissue RNA to establish the time course and profile individual variation of cold-induced gene expression (**Figure 14**). K-means clustering of the top differentially expressed genes (DEGs) identified three distinct patterns of upregulated gene expression (**Figure 14A**). Acutely upregulated genes were induced within 6 hours of cold exposure, but then returned to control levels after chronic cold acclimation. Genes in this cluster are well known targets of protein kinase A (PKA), including peroxisome proliferative activated receptor gamma coactivator 1 alpha (*Ppargc1a*), uncoupling protein 1 (*Ucp1*), nuclear receptor subfamily 4 groups A member 1 (*Nr4a1*), and iodothyronine deiodinase 2 (*Dio2*) (**Figure 14A**). Chronically upregulated genes were induced following 1-2 days of cold exposure and remained elevated for the duration of the time in cold. This cluster included genes involved in lipid synthesis and oxidation, such as elongation of very long chain fatty acids-like 3 (*Elovl3*), fatty acid synthase (*Fasn*), and pyruvate dehydrogenase kinase isoenzyme 4 (*Pdk4*). The third cluster was interesting, as the gene upregulation was delayed and variable among individual mice. Genes in this cluster included proliferation markers (*Birc5*, *Top2a*), as well as various genes indicating innate immune activation and macrophage recruitment (*Lgals3*, *Gpnmb*, *Trem2*) (**Figure 14A**). Importantly, these variables were highly correlated and this relationship was largely independent of time spent in the cold (**Figure 14B**; p-value < 0.001). These data confirm that cell proliferation



and immune cell recruitment are connected and peak around the fourth day of cold exposure.

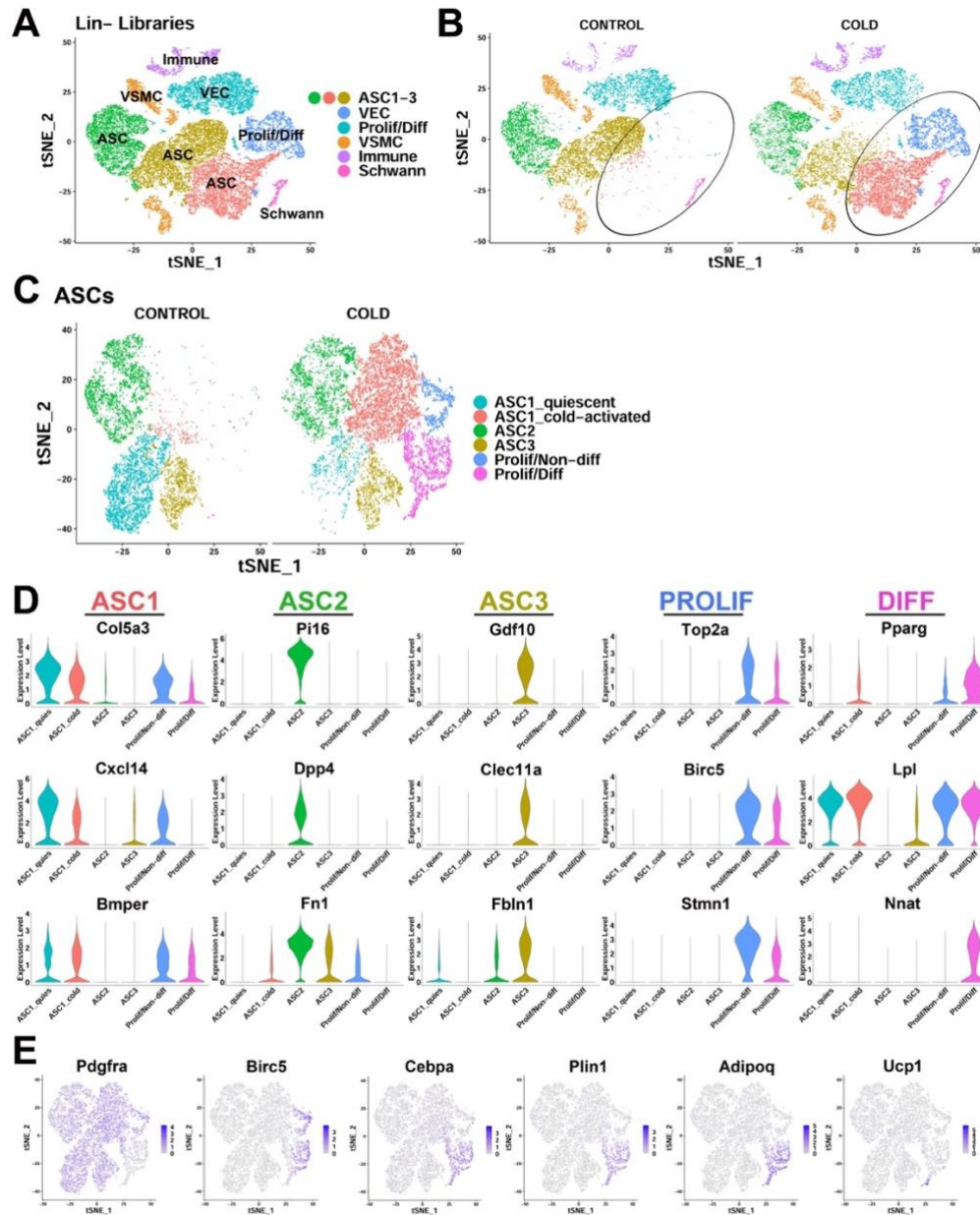


**Figure 15. scRNA-seq reveals ASC heterogeneity and maps adipogenic trajectories in mouse iBAT** (A) t-SNE plot of 28,691 lineage marker negative (Lin-) cell from iBAT of control mice and mice exposed to cold for four days. Clustering applied to the t-SNE plot identified eight major clusters, highlighted in different colors. ASC, adipose tissue stromal cell; VEC, vascular endothelial cell; VSMC, vascular smooth muscle cells; Prolif/Diff, proliferating/differentiating cells. DEGs that define these clusters are in Supplementary Table S6A. (B) t-SNE plot from (A) split into cells from the separate treatments (CONTROL and COLD). Circles highlight new clusters. (C) t-SNE plot of 19,659 re-clustered ASC and Prolif/Diff cells from (A). The t-SNE plot and clustering identified six clusters. Prolif/Non-diff, proliferating/non-differentiating; Prolif/Diff, proliferating/differentiating. DEGs that define these clusters are in Supplementary Table S6B. (D) Violin plots of log<sub>2</sub> expression levels of select marker genes for individual clusters from the CONTROL and COLD data presented in (C). (E) t-SNE plots displaying the log<sub>2</sub> expression levels for genes involved in adipogenic differentiation from the CONTROL and COLD data presented in (C).

## 4.2 iBAT scRNA-seq of total stromal cells identifies multiple adipocyte stromal cell subtypes

To investigate heterogeneity of iBAT stromal and immune cells, as well as gain insight into adipogenic differentiation *in vivo*, we performed scRNA-seq analysis of stromal cells isolated from iBAT (**Figure 1C**). Mice were adapted to room temperature (RT; 22-23°C) or exposed to 6°C for four days to induce iBAT neogenesis and capture the peak in cold-induced proliferation. iBAT stromal cells were isolated and cells were split into immune and non-immune cell populations by magnetic bead cell separation (MACS) with a lineage marker cocktail (**Figure 1C**). Individual single-cell libraries were prepared from two independent experiments of RT control and cold-exposed mice, yielding a total of eight single-cell libraries (**Figure 1C**). Sequencing data from these independent cohorts were merged and integrated, as detailed in Methods (**Figure 1D**).

Lineage marker negative (Lin-) cell libraries contained adipose stromal cells (*Pdgfra*+ ASCs), vascular cells, and proliferating/newly differentiating adipocytes (**Figure 15A**). Clustering of scRNA-seq data from control and cold-exposed mice identified eight major clusters, ranging from ~500 – 6500 cells per cluster (**Figure 15A, Supplementary Table S6A**). Three of these clusters were defined as ASCs based on their expression of common mesenchymal stem cell markers *Pdgfra*, *Cd34*, and lymphocyte antigen 6 complex locus A (*Ly6a*, a.k.a. *Sca1*) (**Figure 16A**) that are often used for identification of adipocyte progenitors [97, 136-138]. ASCs clustered together at low resolution (resolution  $\leq 0.04$ ), indicating they are more similar to each other than the other cell types present in the libraries (**Figure 16B**). scRNA-seq also identified a cluster of proliferating and differentiating ASCs (Prolif/Diff) (**Figure 15A**). The remaining clusters

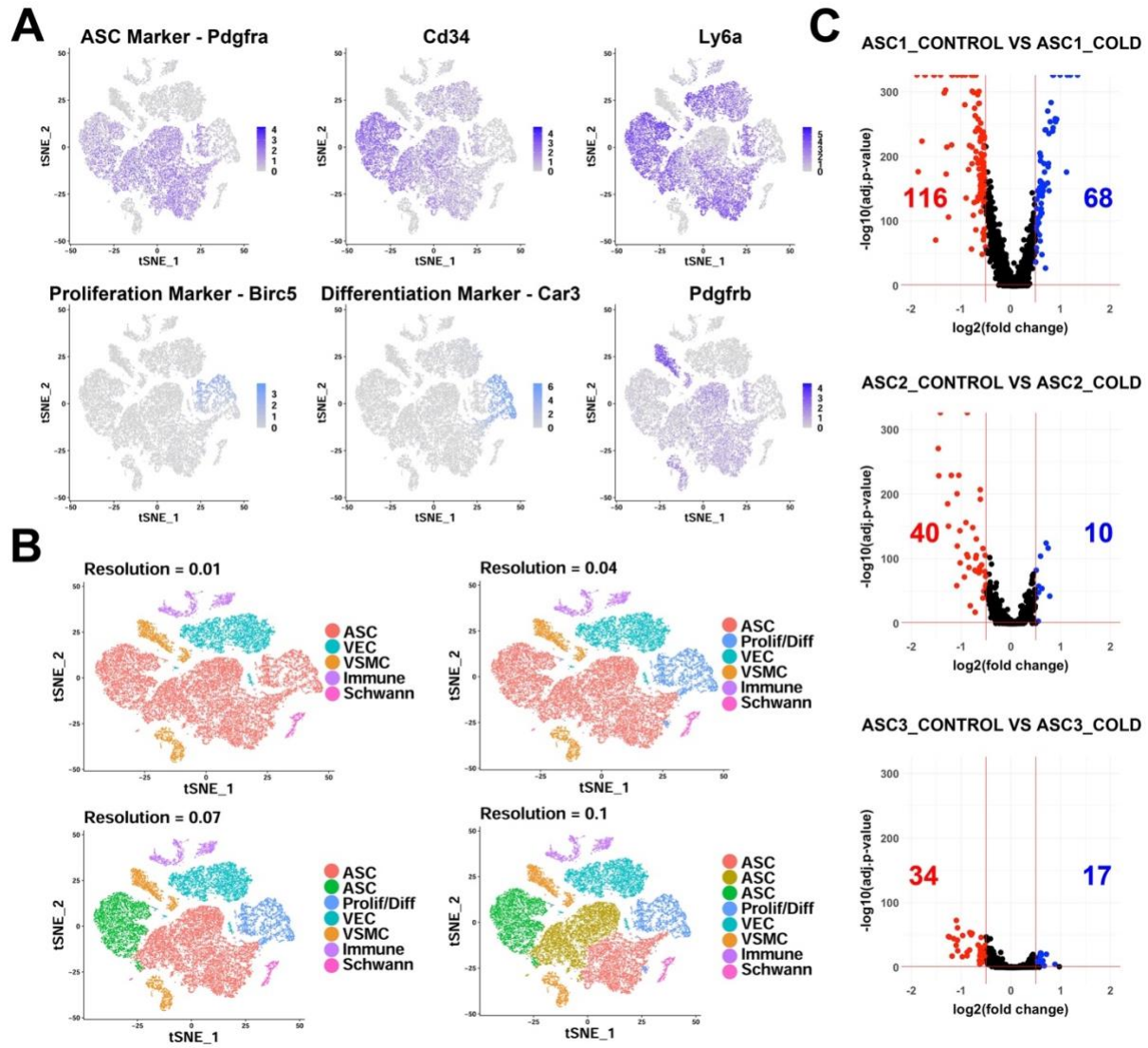


**Figure 16. scRNA-seq analysis of Lin<sup>-</sup> cells from iBAT of control and cold-exposed mice.** Related to Figure 15. (A) t-SNE of Lin<sup>-</sup> data displaying the log<sub>2</sub> expression levels for genes commonly used to isolate adipocyte precursors and markers for proliferating/differentiating cells. (B) t-SNE plot of Lin<sup>-</sup> data with clustering at different resolutions, resulting in different numbers of clusters. (C) Volcano plots of DEGs between cells from control and cold-exposed mice for the three ASC subtypes. Numbers displayed on the plot are the number of genes with an adjusted p-value less than 0.05 and the absolute value of the fold change greater than 0.5.

appeared to be a mixture of vascular endothelial cells (VEC), vascular smooth muscle cells (VSMC), Schwann cells, and a small (~5%) mixture of immune cells (Immune) that were not excluded by MACs separation (**Figure 15A**). Separating data by treatment revealed that two cell clusters were unique to cold-exposed mice (circled; **Figure 15B**).

One cluster retained numerous ASC markers like *Pdgfra*, whereas the other was largely *Pdgfra* negative and expressed high levels of markers of proliferation (e.g., *Birc5*) and adipocyte differentiation (e.g., *Car3*) (**Figure 16A, Supplementary Table S6A**)

To gain greater insight into the relationships among the various ASCs, we reclustered the ASC and Prolif/Diff populations at a higher resolution (**Figure 15C, Supplementary Table S6B**). This clustering resolved three distinct ASC cell types prominent in iBAT controls: ASC1-3 (**Figure 15C**, left). Genes that define these clusters were similar to the expression profiles of mouse PDGFRA<sup>+</sup> ASC subtypes recently identified in various mouse fat depots [97, 136-140]. In control mice, ASC subtypes were distinguished by genes that encode extracellular matrix (ECM) and matrix remodeling proteins, and paracrine signaling proteins of the transforming growth factor beta superfamily. Thus, ASC1 selectively expressed Collagen Type V Alpha 3 Chain (*Col5a3*), C-X-C motif chemokine ligand 14 (*Cxcl14*), and the bone morphogenic protein (BMP)-binding endothelial regulator (*Bmper*) (**Figure 15D**). Cells in ASC2 expressed secreted protease inhibitor peptidase inhibitor 16 (*Pi16*), surface glycoprotein dipeptidyl peptidase 4 (*Dpp4*), and ECM component fibronectin (*Fbn1*). ASC3 cells selectively expressed secreted ligand growth differentiation factor 10 (*Gdf10*), C-type lectin domain containing 11a (*Clec11a*), and fibulin1 (*Fbln1*) (**Figure 15D**).

High resolution clustering identified three additional cell clusters in cold-exposed mice (**Figure 15C**, right). All of these clusters expressed ASC1-specific markers; however, two of the clusters were primarily defined by genes for proliferation (*Top2a*, *Birc5*, *Stmn1*), and/or adipogenic differentiation (*Pparg*, *Lpl*, *Car3*) (**Figure 15D**). This dramatic change in the expression profile of cells expressing ASC1 markers (e.g. *Col5a3*, *Cxcl14*, and

*Bmp6*) (**Figure 16C**) allowed for the characterization of these clusters as distinct expression states of the ASC1 subtype. For the purpose of exposition, we referred to these clusters as 'quiescent' and 'cold-activated' ASC1 from control and cold-exposed libraries, respectively (**Figure 15C**). Cold exposure had comparatively little impact on the profiles of ASC2 or ASC3 (**Figure 16C**). Examination of the two ASC1 expression states indicated that cold activation greatly reduced expression of genes involved in cholesterol biosynthesis (sterol biosynthetic process; GO:0016126,  $p = 2.8E-10$ ), cell adhesion (GO:0007155,  $p = 4.9E-2$ ) and extracellular matrix organization (GO:0030198,  $p = 7.7E-7$ ), and strongly induced expression of genes involved in immune system process (GO:0002376,  $p = 2.2E-6$ ), chemokine activity (GO:0008009,  $p = 5.0E-3$ ) and cell migration (GO:0016477,  $p = 3.6E-4$ ). In addition, ASC1 cells appeared highly poised for adipogenesis, expressing higher levels of the master adipocyte transcriptional regulator peroxisome proliferator activated receptor gamma (*Pparg*) and its target genes, such as lipoprotein lipase (*Lpl*) (**Figure 15D**). Notably, cells in the differentiating cluster selectively expressed the imprinted gene neuronatin (*Nnat*) that was transiently upregulated during differentiation and silenced in mature BA (**Figure 15D**).

### **4.3 iBAT scRNA-seq identifies cells undergoing cold-induced adipogenic differentiation**

Numerous ASC1-specific marker genes were co-expressed in the proliferating and differentiating clusters (**Figure 15D**), indicating that expression of these genes persists as cell differentiated into BAs. In contrast, none of the aforementioned ASC2 and ASC3 markers were expressed in these proliferating/differentiating clusters (**Figure 15D**). From these data, we concluded that cold-activated ASC1 are the immediate progenitors of new



BAs induced by cold exposure. In addition, differentiating cells exhibited a clear trajectory along t-SNE2 that included loss of ASC marker expression (*Pdgfra*), transient proliferation (*Birc5*), and sequential upregulation of early (*Cebpa*) and late (*Adipoq*, *Ucp1*) markers of brown adipogenesis (**Figure 15E**). In contrast, the proliferating, non-differentiating cells that retained ASC1 marker expression did not appear to contribute to adipogenesis and might function to replenish the ASC1 population, as suggested by previous fate mapping studies [37].

In summary, analysis of BAT ASCs and total stromal cell populations indicates that interstitial ASC1 cells are highly responsive to cold exposure and comprise most, if not all, BA progenitors during acute cold-induced neogenesis. In further support of this conclusion, we repeated the lineage tracing experiments described in Lee *et al.* [37] using an independent *Pdgfra*-CreER<sup>T2</sup> x LSL-tdTomato mouse model. We found that 100% (258/258, n = 5 mice) of new brown adipocytes were derived from the proliferation with a recent history of PDGFRA expression.

#### **4.4 Localizing ASC subtypes and adipogenic niches within the tissue microenvironment**

scRNA-seq does not retain the tissue architecture and spatial relationships among cell subtypes, yet previous work suggested that cold-induced neogenesis occurs in specific tissue regions [37]. To address this issue, we used scRNA-seq data to identify subtype-specific mRNAs for spatial analysis by single molecule fluorescence *in situ* hybridization (smFISH). scRNA-seq data indicate that ASC1-3 are distinguished by the differential expression of ECM proteins and paracrine signaling factors, suggesting that these cells have distinct functions in the tissue microenvironment. Therefore, we

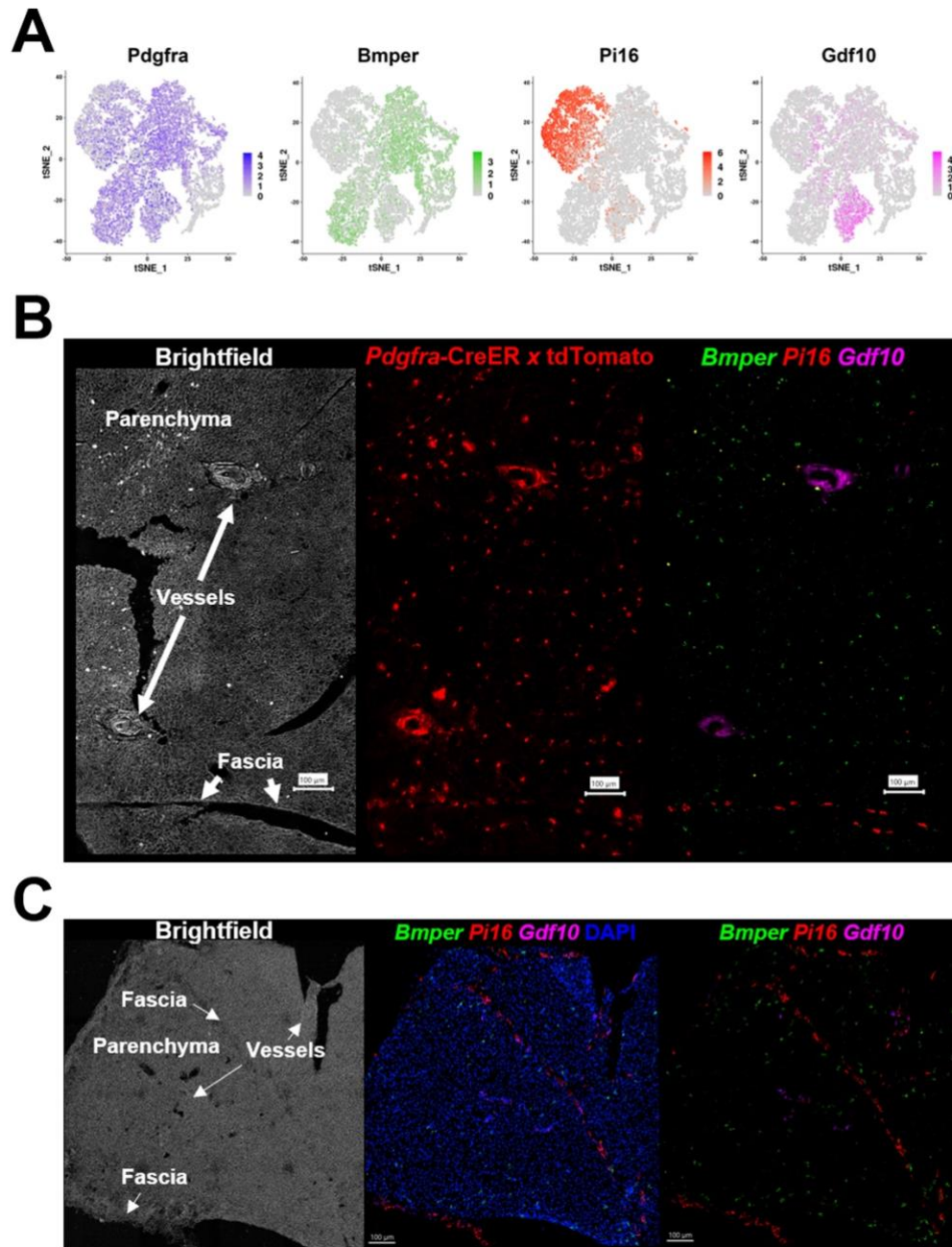


**Figure 17. *Pdgfra*<sup>+</sup> ASC subtypes occupy distinct areas of the tissue** (A) t-SNE plot of log<sub>2</sub> gene expression from *Pdgfra* genetic tracing and smFISH probes in scRNA-seq data. t-SNE plot is ASCs from iBAT of control and cold-exposed mice, as in Figure 2C. (B) Representative image of fixed frozen iBAT from *Pdgfra*-CreER<sup>T2</sup> x LSL-tdTomato reporter mice. (Left) Brightfield image shows gross tissue structures, including the tissue fascia, parenchyma, and large vessels. (Center) TdTomato (red) native fluorescence. (Right) Tissue was bleached and stained with smFISH probes *Bmper* (green), *Pi16* (red), and *Gdf10* (pink). *Bmper* distinguishes ASC1, *Pi16* ASC2, and *Gdf10* ASC3. Scale bar, 100  $\mu$ m. (C) Representative images of control fixed frozen iBAT stained with smFISH probes *Bmper* (green), *Pi16* (red), and *Gdf10* (pink) taken at higher resolution. Associated brightfield image shows gross tissue structures. Nuclei were counterstained with DAPI. Scale bar, 100  $\mu$ m.

examined the spatial distribution of ASCs by smFISH using the subtype-specific markers *Bmper* (ASC1), *Pi16* (ASC2), and *Gdf10* (ASC3) (**Figure 17A**). Using smFISH in combination *Pdgfra*-CreER<sup>T2</sup> x LSL-tdTomato genetic tracing, we note that *Pdgfra*<sup>+</sup> cells are found throughout the tissue, including the parenchyma and fascia. Using smFISH, we found that while ASC1 comprised the majority of the *Pdgfra*<sup>+</sup> parenchymal interstitial cells, ASC2 were localized to the tissue fascia and surrounding large vessels, whereas ASC3 were predominately localized to areas surrounding vessels, but not capillaries (**Figure 17B-C**). Importantly, the interstitial location of ASC1 is consistent with the work of Bukoweicki *et al.* [55] who, using electron microscopy, concluded that cold-induced brown adipocytes are derived from interstitial stromal cells.

#### 4.5 Mapping an adipogenic trajectory *in situ*

scRNA-seq data indicated an adipogenic trajectory in which ASC1 cells reduce expression of stromal markers (*Pdgfra* and *Dcn*), while upregulating proliferation (*Top2a*, *Birc5*) and early differentiation markers (*Car3* and *Plin1*), and finally the terminal differentiation marker *Ucp1*. Among genes expressed within the adipogenic trajectory, we found that *Nnat* was induced during early differentiation, then silenced upon terminal differentiation (**Figure 18A**). Thus, *Nnat* expression marks the transient state of early differentiation. To determine whether we could observe an adipogenic trajectory *in situ*, we used multiplexed smFISH to probe for quiescent ASC1 (interstitial cells, *Dcn*<sup>+</sup>, *Top2a*<sup>-</sup>), proliferating ASC1 (interstitial cells, *Dcn*<sup>+</sup>, *Top2a*<sup>+</sup>), and early differentiating cells (*Nnat*<sup>+</sup>, *Top2a*<sup>+/-</sup>, *Dcn* low) (**Figure 18B**). Low magnification imaging showed a fairly uniform distribution of *Dcn*<sup>+</sup> ASCs throughout iBAT, with little evidence of proliferation (*Top2a*) or active differentiation (*Nnat*). In contrast, cold exposure triggered the

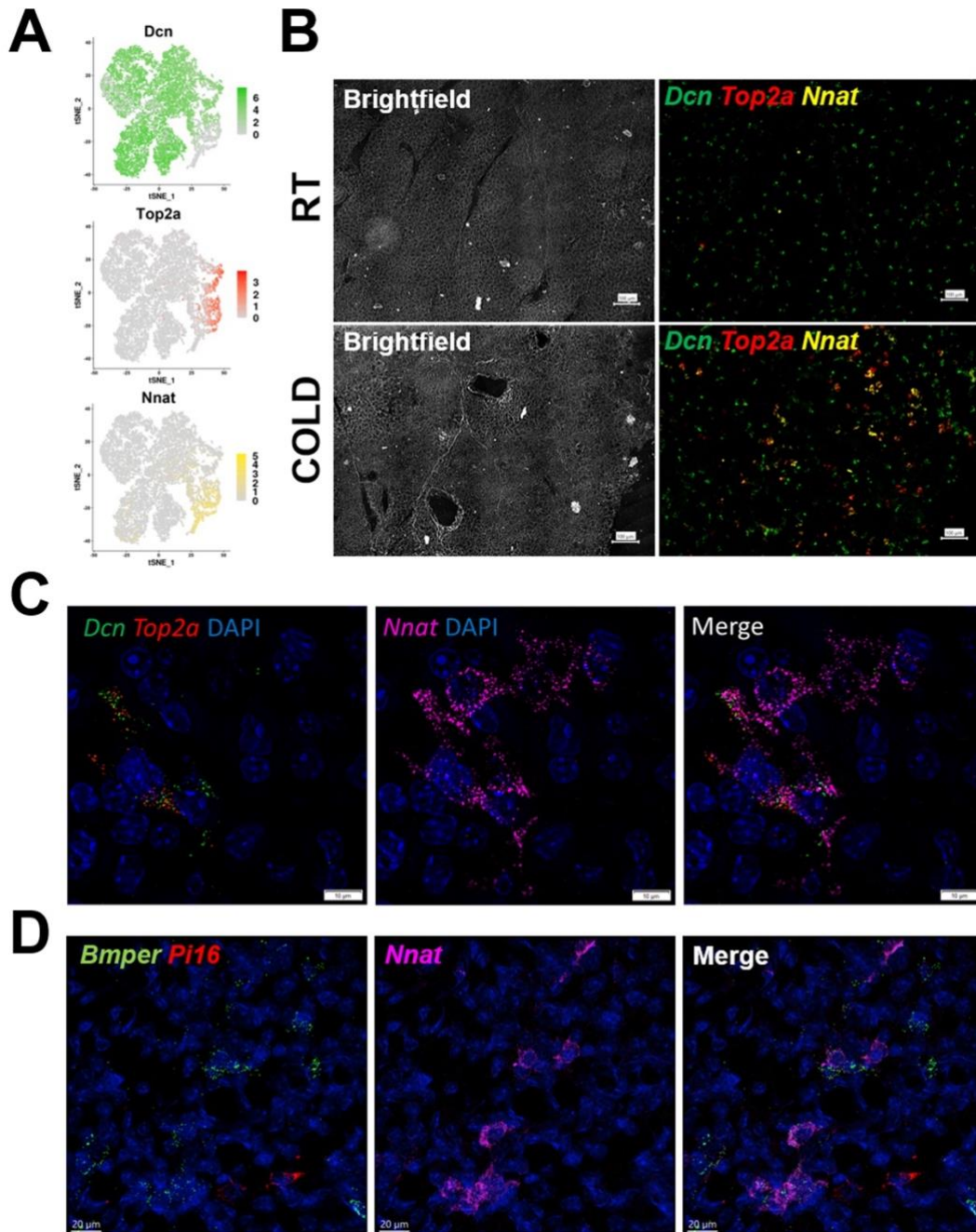
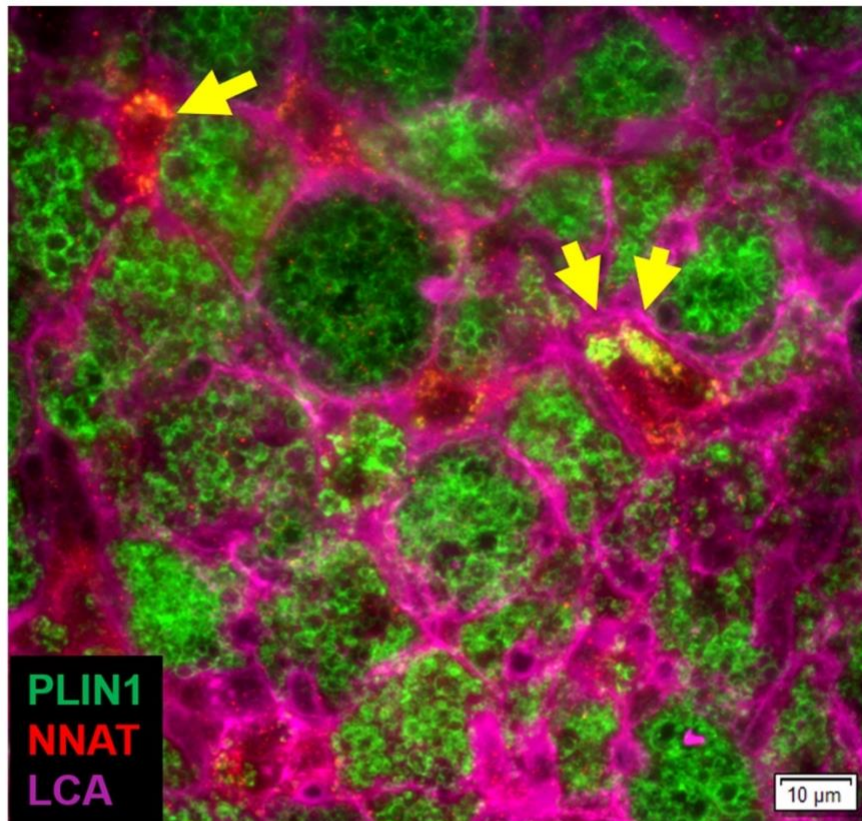


**Figure 18. smFISH maps adipogenic trajectories and supports ASC1 as the direct precursors of new BA.** (A) t-SNE plot of log<sub>2</sub> gene expression of smFISH probes in scRNA-seq data. t-SNE plot displays ASCs from iBAT of control and cold-exposed mice. (B) Representative low magnification images of fixed frozen iBAT stained with smFISH probes for *Dcn* (green), *Top2a* (red), and *Nnat* (yellow). Tissue is from control and cold-exposed mice, as indicated. Associated brightfield image shows gross tissue structure. Scale bar, 100  $\mu$ m. (C) High-magnification image of fixed frozen cold-exposed mouse iBAT stained with smFISH probes *Dcn* (green), *Top2a* (red), and *Nnat* (pink). Nuclei were counterstained with DAPI. Scale bar, 10  $\mu$ m. (D) High-magnification image of fixed frozen cold-exposed mouse iBAT stained with smFISH probes *Bmper* (green), *Pi16* (red), and *Nnat* (pink). Nuclei were counterstained with DAPI. Scale bar, 20  $\mu$ m.

A



B

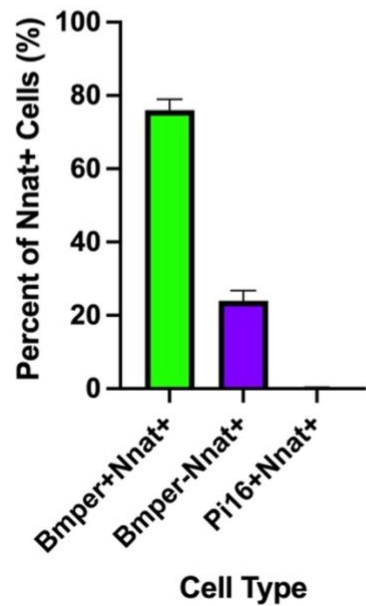


**Figure 19. Immunohistochemistry identified newly differentiating ASCs that are NNAT and PLIN1 positive** Related to Figure 18. (A) Representative image of fixed frozen iBAT from cold-exposed mice stained with the antibodies PLIN1 (green), NNAT (red), and LCA (pink). Arrows identify PLIN1+NNAT+ cells. Scale bar, 10  $\mu$ m. (B) Quantification of the co-expression of smFISH probe *Nnat* with probes for *Bmper* and *Pi16* ( $n = 3$  animals; mean  $\pm$  SD).

appearance of numerous *Top2a*<sup>+</sup> *Dcn*<sup>+</sup> cells, as well as clusters of *Nnat* positive cells with and without co-expression of *Top2a* (**Figure 18B**). Immunofluorescence analysis of NNAT protein confirmed NNAT<sup>+</sup> cells containing nascent PLIN1<sup>+</sup> lipid droplets (**Figure 19A**).

High resolution 3-dimensional confocal imaging provided strong evidence for an adipogenic trajectory within a tissue niche. Thus, we observed proliferating ASC1 immediately adjacent to proliferating/differentiating ASC1, and more distally to differentiating ASC1 lacking expression of proliferation markers. Note the concomitant loss of the ASC marker (*Dcn*) as cells undergo early differentiation (*Nnat*) (**Figure 18C**). As anticipated from scRNA-seq data, the majority of *Nnat*<sup>+</sup> cells co-expressed the ASC1 marker *Bmper*, but not the ASC2 marker *Pi16* (**Figure 18D and Figure 19B**).

#### **4.6 ASC proliferation/differentiation is triggered indirectly via adrenergic activation of BAs**

Cold-induced neogenesis in BAT requires intact sympathetic innervation and can be mimicked by infusion of NE [37, 63]. Furthermore, global knockout of ADRB1 blocked neogenesis induced by systemic NE infusion [37]. From these data, we and others hypothesized that ADRB1 on preadipocytes mediates cold-induced proliferation. To test this hypothesis, we used PDGFRA-CreER<sup>T2</sup> to inducibly knockout *Adrb1* in PDGFRA<sup>+</sup> cells from floxed *Adrb1* mice and performed scRNA-seq analysis (**Figure 20A and Supplementary Table S7A**). Control mice were floxed *Adrb1* mice treated with tamoxifen. Although sparsely expressed, scRNA-seq data indicates that *Adrb1* is expressed in ASC1, but not in ASC2 or ASC3 (**Figure 20B**). Tamoxifen treatment

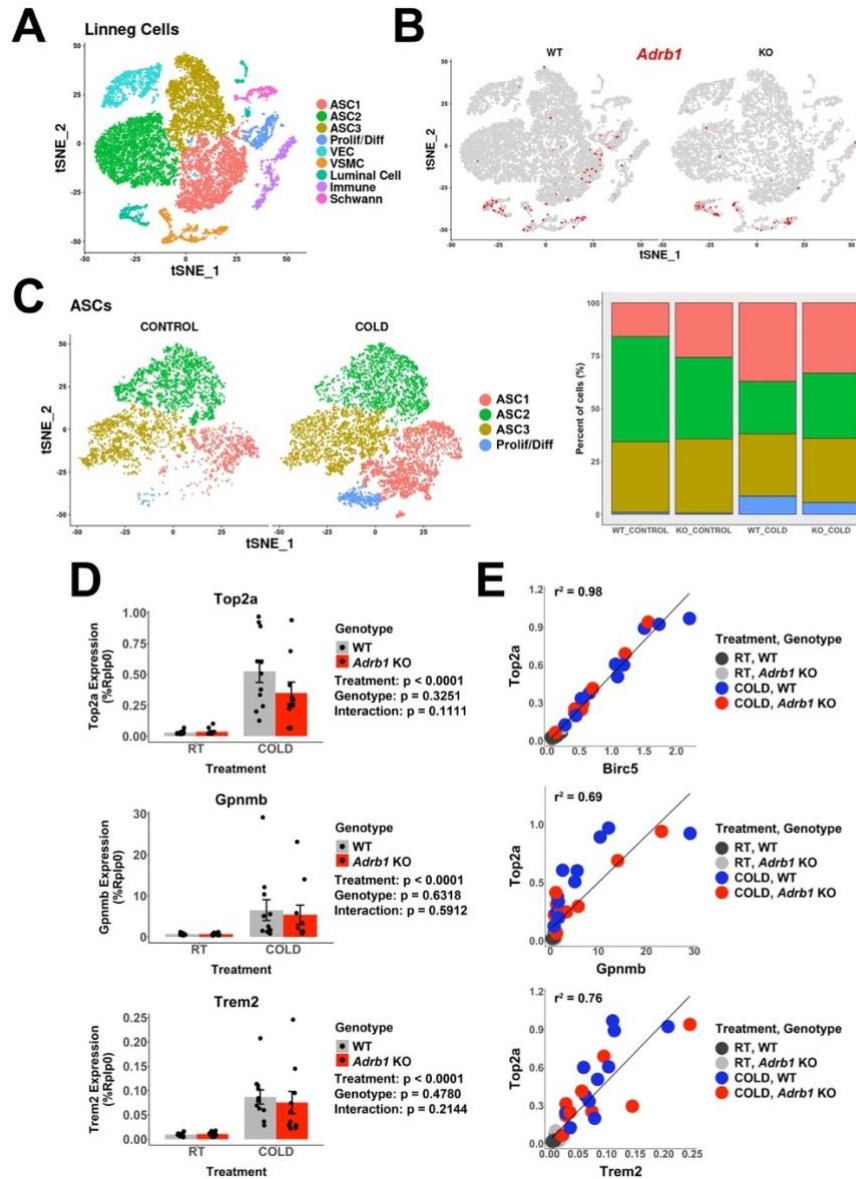


**Figure 20. *Adb1* is dispensable for cold-induced brown adipocyte neogenesis.** Related to Table 1A. (A) t-SNE plot of 18,332 Lin<sup>-</sup> cells from iBAT of WT (*Adb1*<sup>fl/fl</sup>) or *Adb1* KO mice, either housed at room temperature or exposed to cold for four days. Clustering identified 9 cell types. ASC, adipose tissue stromal cell; VEC, vascular endothelial cell; VSMC, vascular smooth muscle cells; Prolif/Diff, proliferating/differentiating cells. DEGs that define these clusters are in Supplementary Table S7A. (B) t-SNE plot from (A), split into cells from WT or *Adb1* KO animals. Colored cells have *Adb1* expression > 0. (C) ASCs and Prolif/Diff cells from (A) reclustered, and split into cells from control or cold-exposed libraries. The bar graph shows the proportion of each cell type in the individual libraries. DEGs that define these clusters are in Supplementary Table S7B. (D) Quantitative PCR analysis of proliferation and immune cell activation genes in iBAT of WT or *Adb1* KO mice maintained at room temperature or exposed to cold for four days (n = 10-11 per condition; mean ± SE). p-values are from 2-way ANOVA analysis of log transformed data. (E) Correlation of specific genes in the quantitative PCR data with *Top2a* expression by individual animal.  $r^2$  values are displayed on the plot.

reduced *Adrb1* expression in ASC1 by more than 90% (chi-square  $p < 0.00001$ , **Figure 20B**). Surprisingly, we found that *Adrb1* KO in ASC1 had no discernable effect on the ability of cold exposure to increase ASC1 proliferation/differentiation (both being ~10-fold over basal in WT and *Adrb1* KO mice) (**Table 1 and Supplementary Table S7B, and Figure 20C**).

In a larger independent cohort of mice, we found that *Adrb1* knockout in ASCs had no significant effect on cold-induced expression of proliferation makers at the whole tissue level (**Figure 20D**). In addition, smFISH demonstrated that cold induced the appearance of differentiating *Nnat+* preadipocytes in the absence of detectible *Adrb1* mRNA following PDGFRA-CreER<sup>T2</sup>-mediated recombination ( $p < 0.00001$ ; **Figure 21A-B**). Taken together, these data demonstrate that ASC *Adrb1* expression is not required for cold-induced BA neogenesis. However, while *Adrb1* expression did not impact neogenesis, 68-72% of the total individual variation in proliferation marker expression (*mKi67*, *Top2a*)

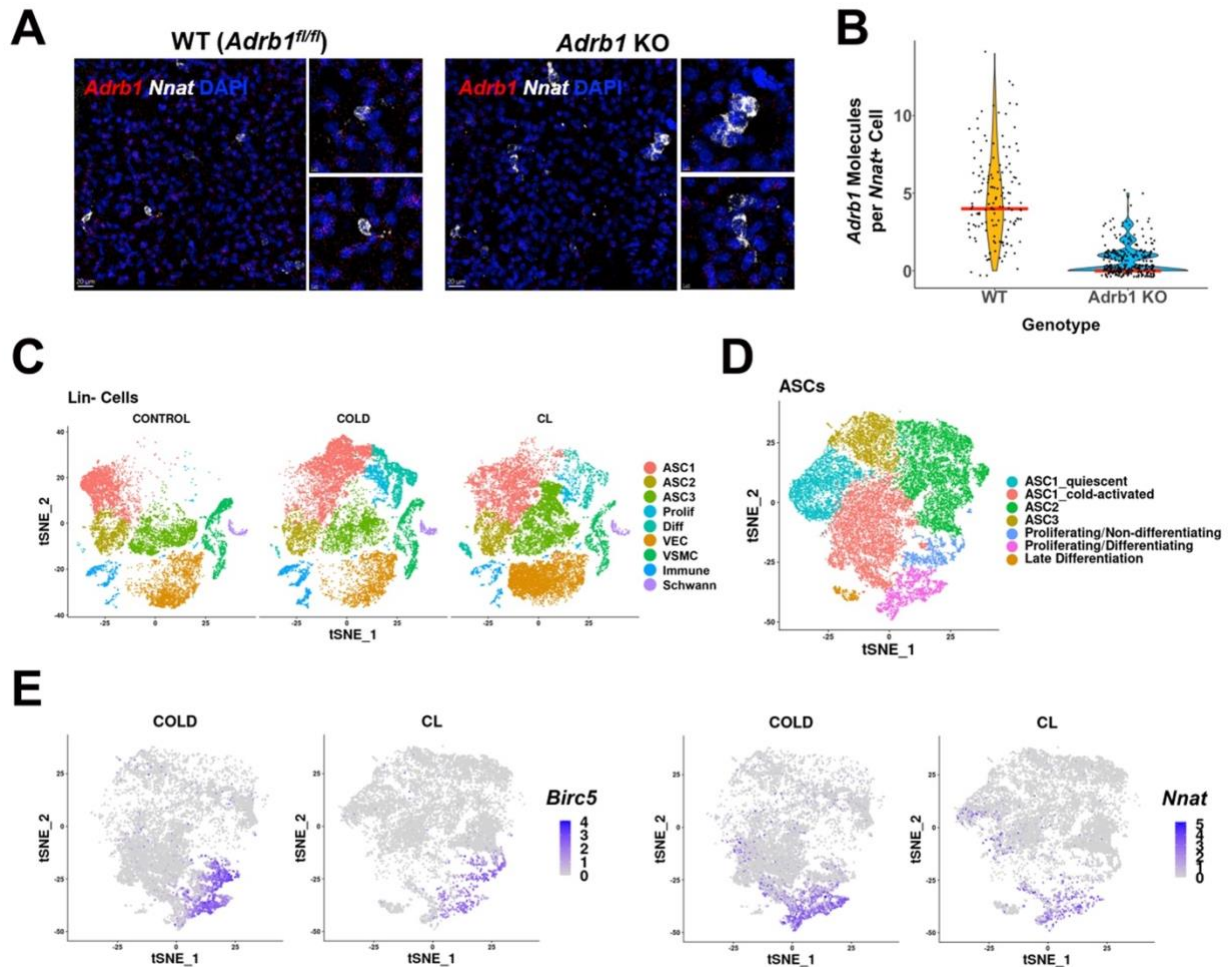
**Table 1. Analysis of  $\beta$ -adrenergic receptor manipulation by scRNA-seq.** Related to Figures 20 and 21. (A) Cell counts and calculated percentages for proliferating/differentiating cells (Prolif/Diff) and ASCs in the *Adrb1* KO single-cell libraries. p-values were calculated by chi-squared analysis between CONTROL and COLD libraries for the two genotypes. \*\*\*p-value  $< 1E-5$ . (B) Cell counts and calculated percentages for Prolif/Diff cells and ASCs in the CONTROL and CL-treated single-cell libraries. p-values were calculated by chi-squared analysis between CONTROL and CL libraries. \*\*\*p-value  $< 1E-5$ .

<b>A</b>	<b>Library</b>	<b>Number of Prolif/Diff Cells</b>	<b>Number of ASCs</b>	<b>Percent of Prolif/Diff Cells out of Total ASCs (%)</b>
	CONTROL, WT	31	3,695	0.84
	COLD, WT	437	5,118	8.54***
	CONTROL, <i>Adrb1</i> KO	9	1,543	0.58
	COLD, <i>Adrb1</i> KO	171	3,063	5.58***

<b>B</b>	<b>Library</b>	<b>Number of Prolif/Diff Cells</b>	<b>Number of ASCs</b>	<b>Percent of Prolif/Diff Cells out of Total ASCs (%)</b>
	CONTROL	38	7,234	0.53
	CL	1,526	11,275	13.5***





**Figure 21. Role of ADRB subtypes in cold-induced iBAT neogenesis** (A) Related to Figure 20. Representative images of iBAT fixed-frozen sections from WT or *Adrb1* KO mice stained with smFISH probes for *Adrb1* (red) and *Nnat* (white). Nuclei were counterstained with DAPI. Scale bar, 20  $\mu$ m and 5  $\mu$ m. (B) Quantification of the number of *Adrb1* molecules in *Nnat*<sup>+</sup> cells between WT and *Adrb1* KO samples ( $n = 3$  animals per condition; red line is the median of the data). (C-E) Related to Table 1B. (C) t-SNE plot of Lin<sup>-</sup> data from control, cold-exposed, and CL-treated mice. DEGs that define these clusters are in Supplementary Table S6C. (D) ASCs and Prolif/Diff cells from (C) reclustered. DEGs that define these clusters are in Supplementary Table S6D. (E) t-SNE plots displaying the log<sub>2</sub> expression levels for proliferation marker *Birc5* and adipogenic differentiation marker *Nnat*.

across treatment groups was accounted for by variation in markers of immune cell recruitment (*Trem2*, *Gpnmb*; **Figure 20E**).

BAs also express ADRB1 and, owing to its higher affinity for NE, is a major receptor for mediating cold-induced metabolic activation [141, 142]. Additionally, we note that proliferation marker expression did not correspond to the rapid activation of classic

adrenergic PKA targets, but instead required chronic cold exposure that was correlated with immune cell recruitment (**Figure 14A-B**). Thus, we reasoned that the effects of cold on ASC1 proliferation might be mediated indirectly by metabolic activation of BAs, similar to brown adipogenesis in WAT [50, 51]. To determine whether adrenergic activation of BAs is sufficient to induce neogenesis, we infused 2 independent cohorts of mice with the highly-selective ADRB3 agonist CL316,243 (CL, 0.75 nmol/hr) for 4 days, noting that BAs express ADRB3, but ASC1 do not. We found that CL treatment triggered significant activation, proliferation and differentiation of ASC1 cells (**Table 1, Supplementary Tables S6C and S6D, and Figure 21C-E**). Taken together, these data strongly suggest that cold exposure triggers progenitor proliferation/differentiation *indirectly* via adrenergic activation of BA and not through direct ADRB1 activation of progenitors.

#### **4.7 Cold exposure recruits macrophages and dendritic cells in iBAT**

Previous analysis indicated that cold-induced neogenesis involves immune cell recruitment and proliferation of uncharacterized myeloid cells [37]. To gain insight into the immune cell complexity of mouse iBAT, we used scRNA-seq to profile lineage positive (Lin+) cells from mice at RT or exposed to cold and identified 16 immune clusters (**Figure 22A and Supplementary Table S6E**). Seven of these clusters were different subpopulations of macrophages and dendritic cells (MAC and DEND, respectively), comprising 52.0% of the cells in this dataset. This dataset also contained populations of monocytes (MONO), natural killer T cells (NKT), T lymphocytes (Tlym), B lymphocytes (Blym), reticulocytes (RET), neutrophils (NEUT), and small populations of non-immune cells (< 3% of total cells). The DEGs that define the Lin+ clusters are presented in **Supplementary Table S6E**.

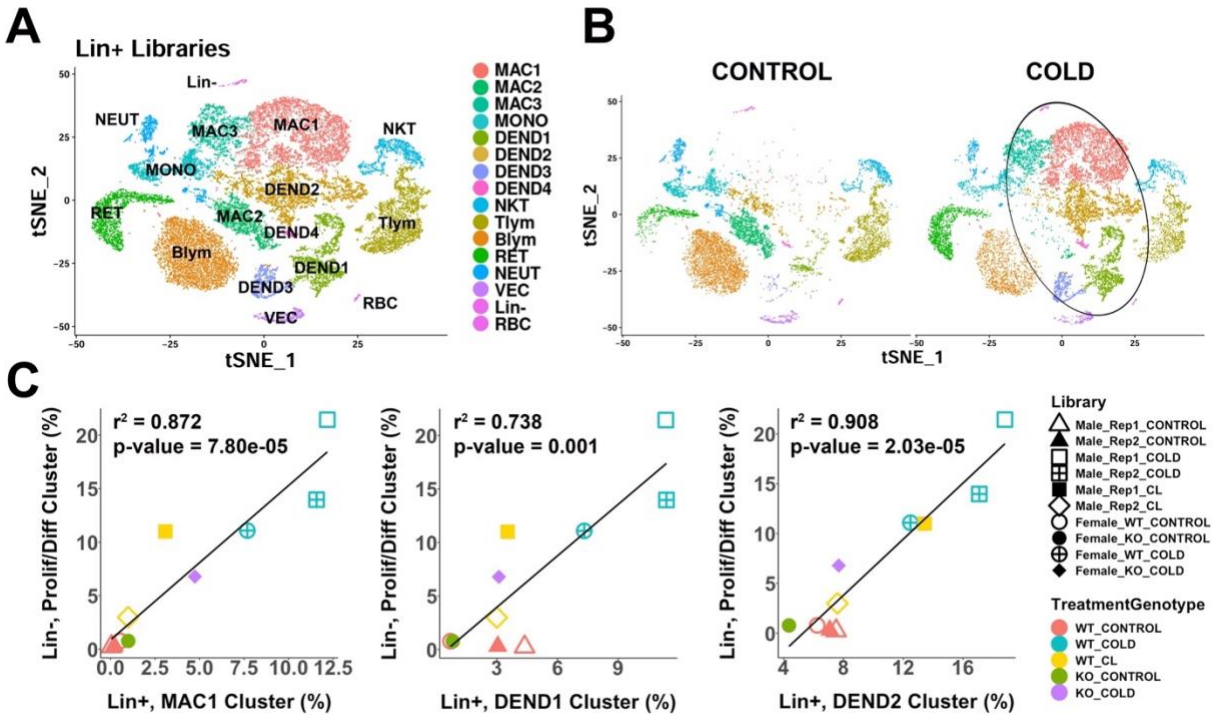


**Figure 22. scRNA-seq analysis of Lin+ immune cells from iBAT of control or cold-exposed mice** (A) t-SNE plot of 25,344 lineage marker positive (Lin+) cells from iBAT of control mice and mice exposed to cold for four days. Clustering applied to the t-SNE plot identified 16 clusters, highlighted in different colors. MAC, macrophage; MONO, monocyte; DEND, dendritic cell; NKT, natural killer T-cell; Tlym, T lymphocyte; Blym, B lymphocyte; RET, reticulocyte; NEUT, neutrophil; VEC, vascular endothelial cell; Lin-, lineage negative cells; RBC, red blood cell. Cell types were determined by DEGs within each cluster. DEGs that define these clusters are in Supplementary Table S6E. (B) t-SNE plot from (A) split into the cells from control (CONTROL) and cold-exposed (COLD) mice. Circle highlights cold-induced cell clusters. (C) Lin+ or Lin- libraries from the 10 single-cell experiments presented in this paper were visualized and clusters in one t-SNE plot and the proportion of each immune cell cluster in the Lin+ libraries were correlated with the proportion of the proliferating/differentiating cluster in the Lin- libraries. Point shapes correspond to individual libraries. Point color corresponds to the combination of treatment (CONTROL, COLD, CL) and the genotype (WT, KO).  $r^2$  values and p-values are displayed on the plot. p-values were calculated using the Pearson's product-moment correlation.

Cold exposure dramatically altered the immune cell landscape in mouse iBAT and led to the expansion of dendritic cells and altered phenotype/subtypes of macrophages (Figure 22B, circled). All four dendritic cell clusters increased with cold exposure (DEND1-4; Figure 22B). DEGs for these clusters generally correspond to known dendritic cell subtypes. DEND1 cells expressed conventional dendritic cell type 1 (cDC1) markers, including high levels of the master transcriptional regulator *Irf8*, as well as genes *Ppt1*,

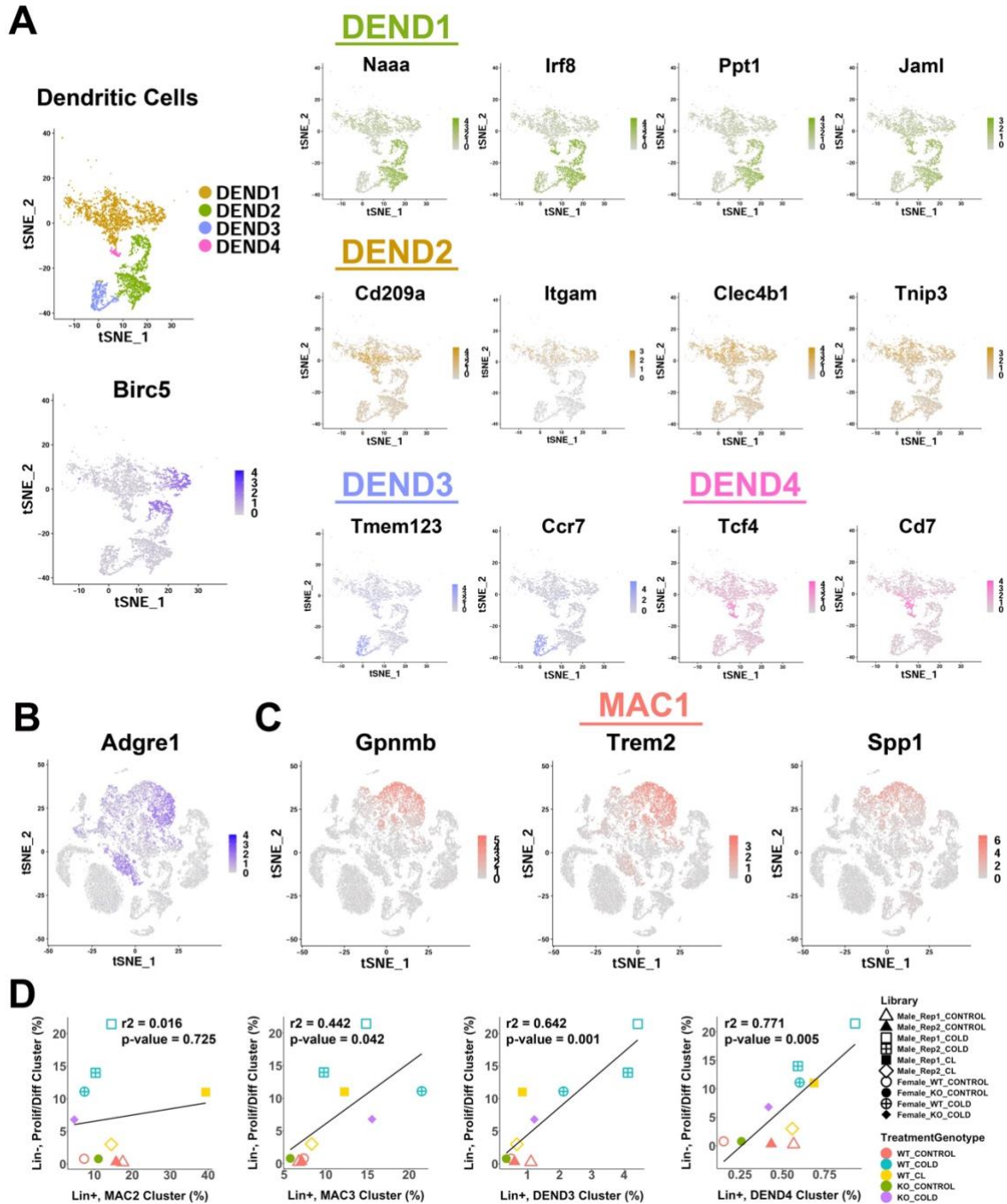


**Figure 23. Analysis gene expression markers from single-cell analysis of iBAT dendritic cells and lipid-handling macrophages** Related to Figure 22. (A) t-SNE of dendritic cell clusters from Figure 22A (top left), along with a t-SNE plot displaying the log2 expression levels of proliferation marker *Birc5* (bottom left). Additionally, t-SNE plots displaying the log2 expression levels for genes that define each dendritic cell cluster. (B) t-SNE plot displaying the log2 expression level of *Adgre1* (F4/80). (C) t-SNE plots displaying the log2 expression levels for genes that define cluster MAC1. (D) Correlation of remaining immune cell clusters with proliferating/differentiating cells in across all single-cell libraries.  $r^2$  values and p-values are displayed on the plot. p-values were calculated using the Pearson's product-moment correlation.

*Jaml*, and *Naaa* (**Figure 23A**) [86, 143]. These cDC1 cells were 33.6% of the dendritic cells. We identified the cluster DEND2 as monocyte-derived dendritic cells (moDCs) based on expression of the moDC markers *Cd209a* and *Itgam* (CD11b) (**Figure 23A**) [144]. The most abundant dendritic cell type in this dataset (51.6% of dendritic cells), moDCs also expressed *Tnip3* and *Clec4b1* (**Figure 23A**). The minor dendritic cell clusters, DEND3 (12.1%) and DEND4 (2.7%) exhibited profiles consistent with mature/migratory dendritic cells (*Tmem123*, *Ccr7*) [145, 146], and plasmacytoid dendritic cells (*Irf8* high, *Cd7*, *Tcf4*) [147] (**Figure 23A**), respectively.

Previous fluorescence-activated cell sorting (FACS) analysis demonstrated that cold exposure induces proliferation in F4/80+ immune cells [37]. While *Adgre1* (gene encoding the F4/80 antigen) was expressed in both macrophage and dendritic cell populations (**Figure 23B**), multidimensional scRNA-seq analysis indicates cold-induced proliferation occurs mostly in cDC (DEND1) and moDC (DEND2) subpopulations and not in cold-recruited macrophages. (**Figure 23A**).

scRNA-seq distinguished one resident population of macrophages in control mice, and cold exposure led to the dramatic appearance of two new types of macrophages (**Figure 22B**). Cold exposure increased the number of MAC1 and MAC3 macrophage populations and reduced the number of MAC2 cells (**Figure 22B**). The MAC2 cluster had a resident macrophage profile, and expressed genes including *Folr2*, *F13a1*, *Cbr2*, *Pf4*, *Gas6*, and *Mrc1*. Some of these genes (*Folr2*, *Cbr2*, *Mrc1*) are also associated with an M2 anti-inflammatory macrophage phenotype. The largest cold-induced macrophage cluster, MAC1, had an anti-inflammatory and lipid handling phenotype. MAC1 cells express the dead cell receptor *Trem2*<sup>+</sup>, which functions in to promote efferocytosis

(**Figure 23C**). These cells also express the anti-inflammatory gene *Gpnmb*, and *Spp1*, which is known in other adipose depots as chemotactic for ASCs (**Figure 23C**). Apart from these markers, the top DEGs for MAC1 include genes involved in ECM remodeling (*Ctsb*, *Ctsd*, *Ctsl*, *Mmp12*), and lipid handling (*Fabp5*, *Lpl*, *Plin2*). These macrophages have a similar expression profile to that recently described during WAT remodeling [97, 148]. The second cold-induced macrophage cluster, MAC3, had lower expression of these MAC1 markers and higher expression of interferon-activated genes (*Ifi204*, *Ifi207*, *Ifi209*), several c-type lectin domain family 4 members (*Clec4d*, *Clec4e*, *Clec4n*), and many other interferon-regulated genes (*Irf7*, *Slnf2*, *Ifit3*, *Rsad2*, *Isg15*).

#### **4.8 Recruitment of cold-induced immune cells predicts the magnitude of progenitor proliferation and differentiation across experimental conditions**

In this study we performed 10 independent scRNA-seq experiments of > 100,000 stromal and immune cells in which the magnitude of neogenesis was manipulated by temperature, and beta-adrenergic receptor knockout and activation. Using these data, we assessed whether the induction of ASC1 proliferation and differentiation was associated with the recruitment of specific immune cell populations. We found that ASC1 proliferation and differentiation were strongly predicted by the magnitude of cold-induced recruitment of conventional dendritic cells type 1 (DEND1;  $r^2 = 0.74$ ), monocyte-derived dendritic cells (DEND2;  $r^2 = 0.91$ ) and lipid-handling macrophages (MAC1,  $r^2 = 0.87$ ) across these diverse experimental conditions (**Figure 22C** and **Figure 23D**). Importantly, this highly significant relationship held even when basal values were excluded from the analysis.

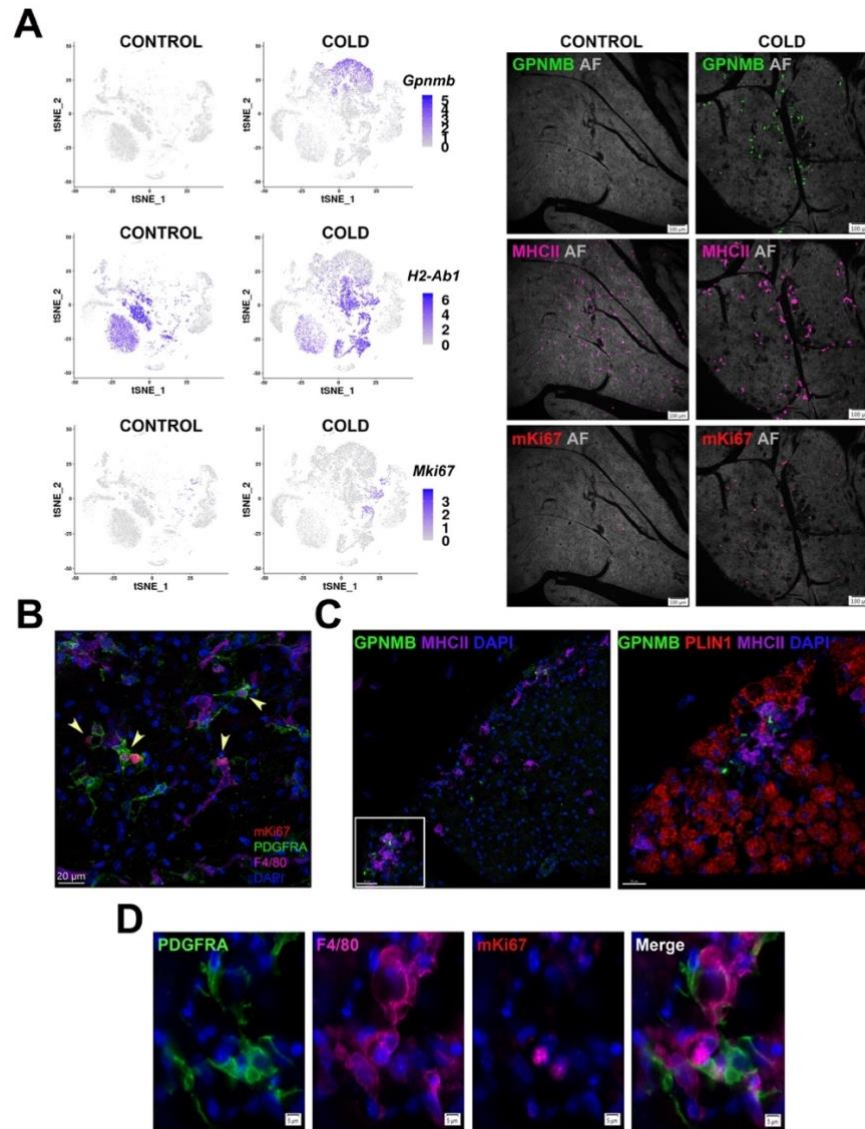


**Figure 24. Cold-induced iBAT neogenesis involves close interaction between immune cells and proliferating ASCs** (A) Low-magnification images of iBAT fixed-frozen sections from control and cold-exposed mice stained for GPNMB (green), MHCII (pink), and mKi67 (red), along with their corresponding log<sub>2</sub> gene expression in Lin<sup>+</sup> scRNA-seq data. Lin<sup>+</sup> t-SNE plots were split between cells from control and cold-exposed mice. Tissue images for antibody staining show the same tissue area for each treatment. Background for each image is autofluorescence (AF) in grey scale. Scale bar, 100  $\mu$ m. (B) iBAT fixed-frozen sections from cold-exposed mice stained with antibodies for mKi67 (red), PDGFRA (green), and F4/80 (pink). Nuclei were counterstained with DAPI. Arrows indicate PDGFRA<sup>+</sup>mKi67<sup>+</sup> cells. Scale bar, 20  $\mu$ m. 3D rendering presented in Supplementary Movie 1. (C) iBAT fixed-frozen sections from cold-exposed mice. Left image displays antibody staining for GPNMB (green) and MHCII (purple). Right image is a magnified view of the boxed region from left, displaying staining for GPNMB (green), PLIN1 (red), and MHCII (purple). Nuclei were counterstained with DAPI. Scale bars, 30  $\mu$ m and 20  $\mu$ m. 3D rendering presented in Supplementary Movie 2. (D) iBAT fixed-frozen sections from cold-exposed mice stained for PDGFRA (green), F4/80 (pink), and mKi67 (red). Nuclei were counterstained with DAPI. Scale bar, 5  $\mu$ m.

#### **4.9 Macrophages and dendritic cells interact with proliferating ASCs in known sites of neogenesis**

The data above suggest a scenario in which metabolic stress in brown adipocytes leads to immune cell recruitment, niche formation, and brown adipocyte neogenesis, similar to that observed for brown adipocyte neogenesis induced by ADRB3 activation in WAT [51, 67, 149]. We previously reported that cold-induced neogenesis in mice is concentrated near tissue borders, although intense drug-induced neogenesis can expand into the parenchyma [37]. Furthermore, analysis of adipogenesis induced by ADRB3 activation in white adipose tissue demonstrated a close interaction of immune cells (mainly macrophages) and progenitor cells at sites of dead adipocyte removal. Therefore, we next examined the distribution of immune cells relative to tissue architecture and proximity to activated progenitors, utilizing informative cell markers extracted from scRNA-seq analysis.

MAC2 are the predominant macrophage subtype of warm-adapted mice and their levels sharply declined during cold exposure (**Figure 22B**). MAC2 express F4/80 (*Adgre1*) and MHCII (*H2-Ab1*), have a compact morphology, and are evenly distributed throughout the parenchyma (**Figure 24A**). As expected, few stromal or immune cells of control mice were positive for the proliferation marker mKi67 (**Figure 24A**). Histological analysis of iBAT at the peak for cold-induced proliferation demonstrated the dramatic appearance of GPNMB+ MAC1 cells and dendritic cells labeled with MHCII antibodies (noting that MHCII+ MAC2 are nearly absent in iBAT of cold-exposed mice) (**Figure 24A**). Interestingly, nearly all MAC1 and dendritic cells were present in clusters in two distinct locations: within 50 micrometers of the tissue border or near acellular vacancies in the



parenchyma. As expected, low resolution imaging identified numerous mKi67+ cells in sections of cold-exposed iBAT, indicative on ongoing proliferation (**Figure 24A**).

High-resolution confocal imaging of the tissue border region demonstrated that nearly all actively proliferating ASC1 (mKi67+, PDGFRA+) cells were in close proximity to F4/80+ immune cells (**Figure 24B and Supplementary Movie 1**). According to our single cell data, F4/80 (*Adgre1*) is expressed in macrophage clusters and DEND2 (moDCs). ASC1 extend cellular processes that have the potential to probe the tissue microenvironment [37]. 3-D confocal microscopy of cold-exposed iBAT indicates that ASC1 cellular processes extend toward and contact F4/80+ cells (**Figure 24B and Supplementary Movie 1**).

We also observed GPNMB+ MAC1 and MHCII+ dendritic cells surrounding vacancies lacking cellular autofluorescence and PLIN1, a lipid droplet marker of live adipocytes (**Figure 24C and Supplementary Movie 2**). Such structures are the hallmark of adipocytes undergoing death and replacement [50, 150]. Indeed, all PLIN1 negative

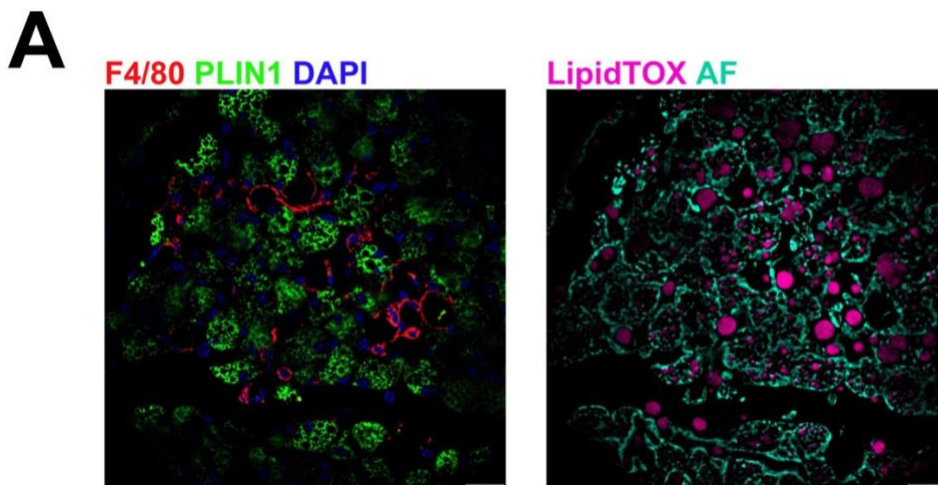


**Figure 25. Macrophages surround cellular vacancies containing lipid remnants** (A) iBAT fixed-frozen sections from cold-exposed mice. Both images show the same tissue area. Left image displays antibody staining for F4/80 (red) and PLIN1 (green). Nuclei were counterstained with DAPI. Right image displays lipid staining (LipidTOX, pink) and cellular autofluorescence (AF, cyan). Scale bar, 20  $\mu$ m.

vacancies had a uniform diameter of approximately 20  $\mu\text{m}$  which closely matches the size of adjacent BAs, and many retained remnants of intracellular lipid droplets in cyrosections (Figure 24C, Supplementary Movie 2, and Figure 25). Thus, the vacancies appear to be sites of efferocytosis by GPNMB+ MAC1 and MHCII+ dendritic cells. Importantly, these sites contained actively proliferating (mKi67+) ASC1 (PDGFRA+) near immune cells (F4/80+) (Figure 24D).

#### 4.10 Adipogenic niches are dynamic

We estimate that at the peak of neogenesis there are hundreds of adipogenic niches

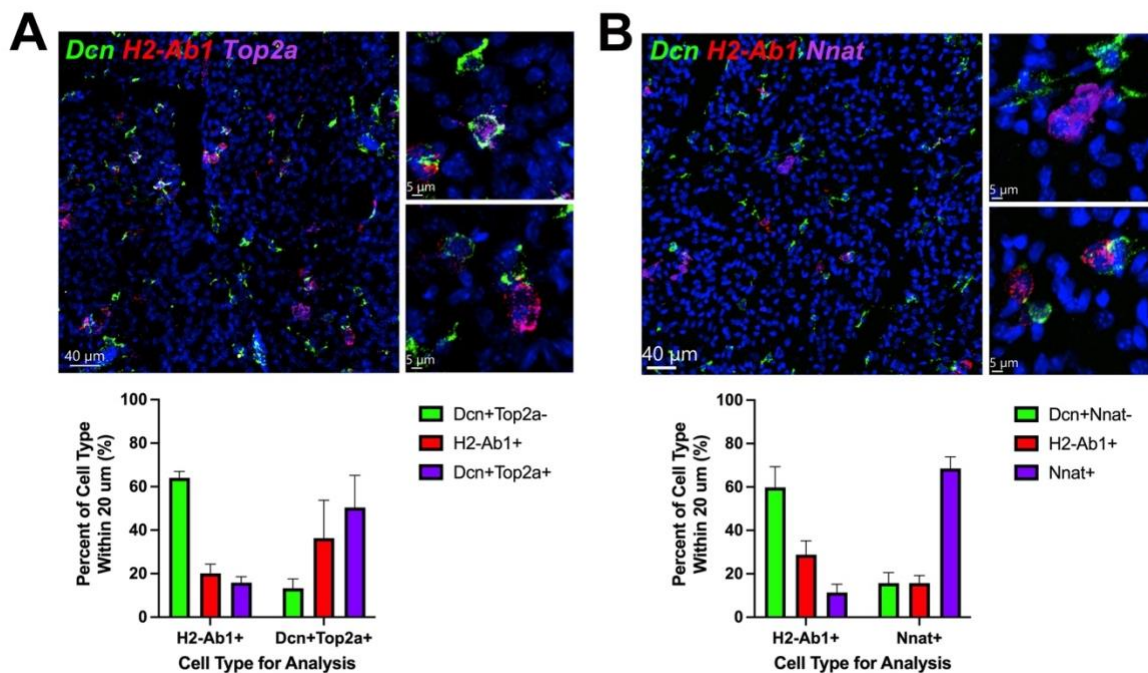


**Figure 26. ASCs and immune cells comprise a dynamic cellular niche** (A, top) Representative images of fixed frozen mouse cold-exposed iBAT. Tissue was stained with smFISH probes *Dcn* (green), *H2-Ab1* (red), and *Top2a* (pink). Nuclei were counterstained with DAPI. Images on the right are a magnified view of the boxed regions on the left. Scale bars, 40  $\mu\text{m}$  and 5  $\mu\text{m}$ . (A, bottom) Quantification of cell types within 20  $\mu\text{m}$  around either an *H2-Ab1*+ cell or a *Dcn+Top2a*+ cell ( $n = 3$  animals; mean  $\pm$  SD). (B) Representative images of fixed frozen mouse cold-exposed iBAT. Tissue was stained with smFISH probes *Dcn* (green), *H2-Ab1* (red), and *Nnat* (pink). Nuclei were counterstained with DAPI. Images on the right are a magnified view of the boxed regions on the left. Scale bars, 40  $\mu\text{m}$  and 5  $\mu\text{m}$ . (B, bottom) Quantification of cell types within 20  $\mu\text{m}$  around either an *H2-Ab1*+ cell or a *Nnat*+ cell ( $n = 3$  mice, >100 cells/mouse; mean  $\pm$  SD).

in various stages of initiation, proliferation and differentiation. We hypothesized that smFISH analysis of state-dependent markers (e.g., *Top2a* and *Nnat*) might provide clues regarding the cellular basis of adipogenic niche formation and resolution. For this purpose, we used smFISH to systematically assess the proximity of immune cells (*H2-Ab1*) with proliferating (*Dcn+*, *Top2a+*) and differentiating progenitors (*Nnat+*), and considered neighbors within 20 microns (the thickness of cryosections) of the reference cell type. Analysis by machine learning classification and automated measurement yielded similar results. As expected from immunofluorescence analysis (**Figure 26A-B**), proliferating progenitors and differentiating adipocytes were nearest neighbors (NN) of themselves, reflecting clustering within adipogenic niches. Furthermore, proliferating progenitors were closely associated with *H2-Ab1+* dendritic cells (**Figure 26A**) and this close association declined by 4-5-fold as progenitors differentiated into BAs (**Figure 26B**). These data indicate that progenitor proliferation occurs in close proximity to recruited immune cells, which depart as progenitors differentiate into BAs.

smFISH provides a tissue 'snapshot' suggesting dynamic trafficking and interactions among progenitor and phagocytes in tissue renewal and expansion. To further establish this concept, we mapped the relative positions of actively-proliferating ASC1 and newly-differentiated BAs relative to dendritic cells in the tissue microenvironment. For this purpose, PDGFRA+ progenitors were genetically labeled using *Pdgfra-CreER<sup>T2</sup>* x *LSL-tdTomato* mice prior to cold exposure (**Figure 27A**), then flash-tagged proliferating cells with 5-ethynyl-2'-deoxyuridine (EdU) and monitored their positions relative to immune cells immediately after tagging (on the third day), or 2 days later when most cells had

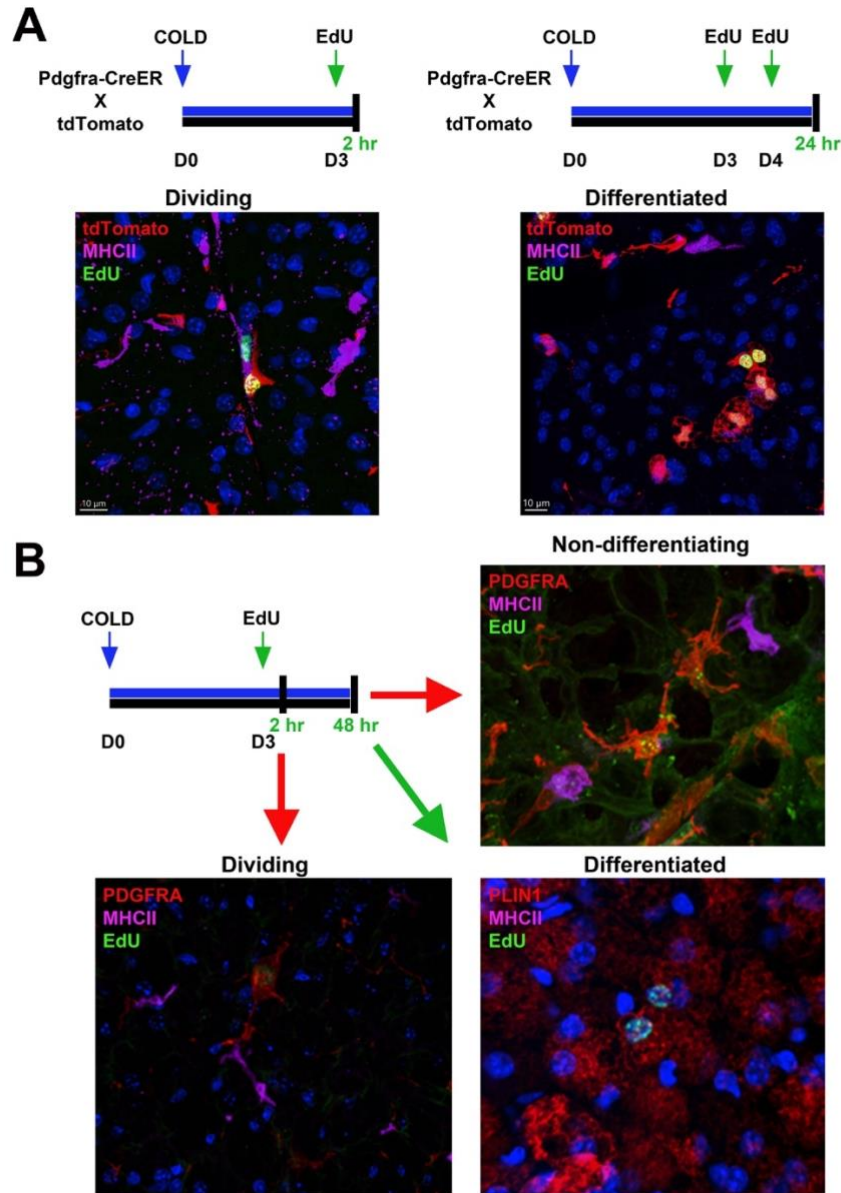


**Figure 27. Flash-labeling of proliferating cells and proximity of MHCII<sup>+</sup> dendritic cells.** (A, top) Procedure for EdU labeling to trace dividing ASCs and differentiated adipocytes. *Pdgfra*-CreER<sup>T2</sup> x LSL-tdTomato were used for genetic tracing of *Pdgfra*<sup>+</sup> cells. Seven days after induction with tamoxifen, animals were housed in the cold for up to five days. For dividing ASCs, on the third day animals were injected with EdU, and sacrificed two hours later. For differentiated adipocytes, animals were injected with EdU on days three and four of cold exposure and sacrificed on day 5. (A, bottom) Representative images from iBAT for the experiments outlined, where tissue was stained with EdU (green) or MHCII (pink). tdTomato (red) was detected by native fluorescence. Nuclei were counterstained with DAPI. Scale bar, 10  $\mu$ m. (B) Alternatively, C57 mice were exposed to cold for up to 5 days. EdU was injected on day three and animals were sacrificed on two hours or 2 days after EdU injection. Representative images of iBAT harvested from mice after the indicated times. Tissue was stained with either PDGFRA (red), MHCII (pink), and EdU (green) or PLIN1 (red), MHCII (pink), and EdU (green). Nuclei were counterstained with DAPI.

differentiated into BAs. This analysis indicated that MHCII<sup>+</sup> DC were three times more likely to be within 10 micrometers of a dividing preadipocyte versus a divided/differentiated brown adipocyte (27.3% vs 9.35%,  $p = 0.00013$ ,  $n = 267$  cells, 2-3 mice) (**Figure 27A**). We confirmed spatial relationships among actively dividing and newly differentiated progenitors by immunofluorescence (**Figure 27B**). In this experiment, we also located a limited number of progenitors that divided on day 3, yet failed to differentiate by day 5, and found that nearly all of these cells maintained close contact with MHCII<sup>+</sup> cells in the tissue microenvironment (**Figure 27B**). Taken together, these observations indicate that ASC1 and recruited immune cells comprise a cellular niche for progenitor proliferation and that immune cells depart the niche as progenitors differentiate into BA.

#### **4.11 Investigating potential cell-cell communication in the adipogenic niche**

The close proximity of the cold-activated ASC1 and immune cell subtypes suggests cell-to-cell communication orchestrates the neogenic process. To gain insights into potential ligand-receptor interactions between immune and progenitor cells, we interrogated our scRNA-seq data for ligand-receptor pairs using published databases and publicly available computational programs [102-104]. All pairs identified by these methods were manually examined for ligand-receptor specificity in our dataset. We focused on ligand-receptor pairs between immune cells (MAC1 and DEND1-4) and cold-responsive ASC1. This analysis identified several ligand-receptor pairs that could contribute to adipocyte progenitor recruitment and differentiation (**Figure 28A**). Osteopontin (*Spp1*), a DEG in the cold-induced MAC1 cluster (**Figure 23C**), is known to be chemotactic for ASCs in other adipose depots [51, 67]. Cd44 molecule (*Cd44*) and Syndecan 1 (*Sdc1*) were identified as receptors for *Spp1* in our queried databases (**Figure 28A**). *Cd44* has

already been identified as a marker of activated adipocyte progenitors in other depots [50, 67, 109]. *Sdc1* has been categorized as a regulator of adipogenesis [151-153], and its expression was highly specific to the cold-activated ASC1 cells.

Cold-responsive immune cells and ASC1 also selectively upregulated genes

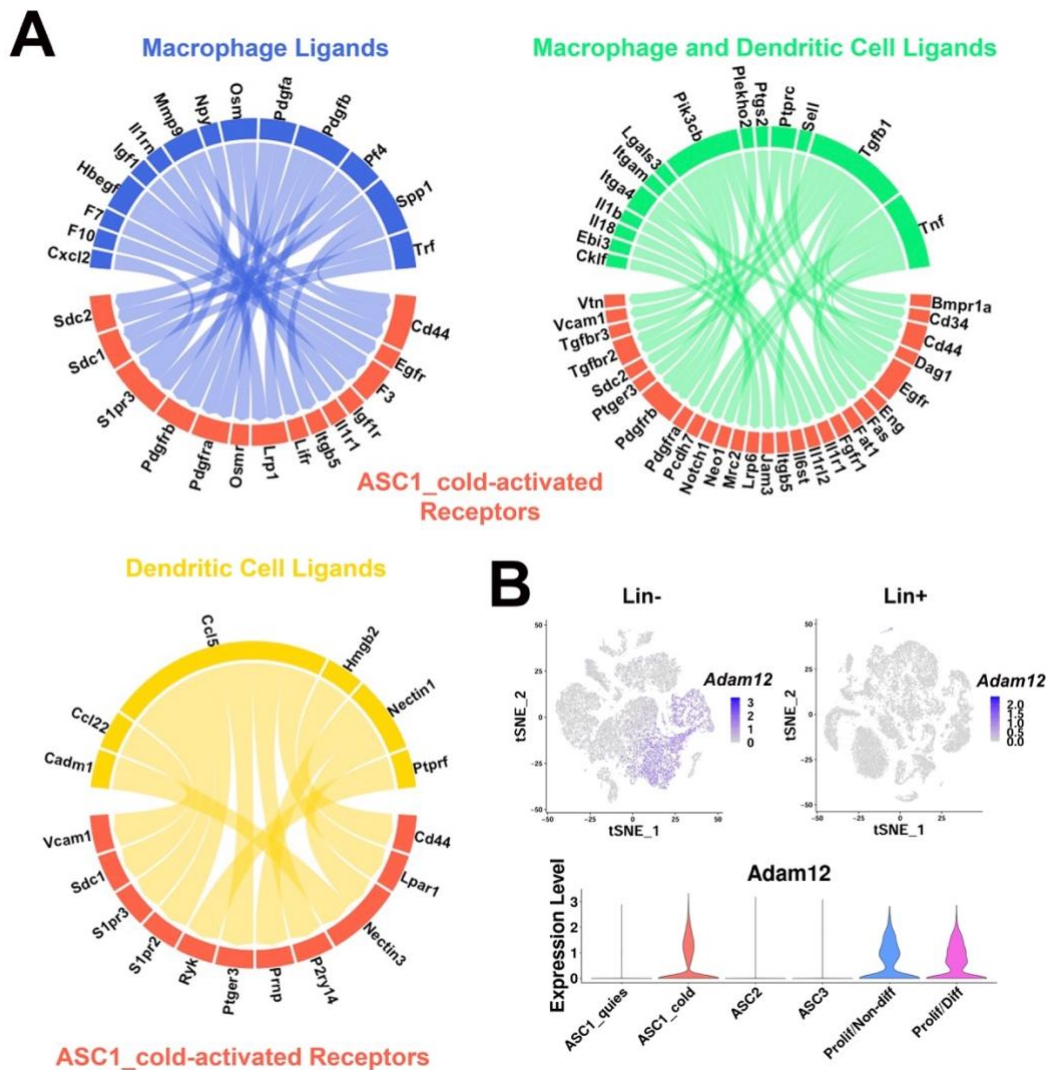


**Figure 28. scRNA-seq data reveal potential ligand-receptor pairs for ASC-immune cell crosstalk** (A) Circos plots of ligand-receptor pairs where cold-activated ASC1 cells expressed the receptor, and dendritic cells and/or macrophages expressed the ligand. Ligand-receptor pairs were identified from computational programs CellPhoneDB and NicheNet, and additional ligand-receptor databases. The cellular phenotype specificity was confirmed using expression patterns in t-SNE plots. (B) t-SNE plots displaying the log<sub>2</sub> expression pattern levels for *Adam12* corresponding to Lin<sup>-</sup> data (Figure 15A), Lin<sup>+</sup> data (Figure 22A), and ASC re-clustered data (Figure 15C), respectively.

involved in ECM remodeling, including several metalloproteinases that are known to activate latent growth factors in the microenvironment. In this regard, cold exposure greatly upregulated ASC1 expression of the disintegrin and metalloproteinase ADAM metallopeptidase domain 12 (*Adam12*) (**Figure 28B**). ADAM12 is multifunctional sheddase that could promote ASC1 proliferation and differentiation by multiple mechanisms, including local release of active HB-EGF and augmentation of IGF1 signaling via inactivation of IGF3BP [154, 155]. Indeed, ADAM12 promotes adipogenesis *in vitro*, and ectopic overexpression of ADAM12 in muscle is sufficient to induce fat pad formation *in vivo* [117, 156].

## Chapter 5. Effect of tissue digestion method on single-cell analysis

### 5.1 Introduction

The identity of the direct precursors of new brown adipocytes remains highly debated [37, 51, 73, 136]. Early fate mapping by Bukoweicki *et al.* strongly indicated that brown adipocytes arise from interstitial cells that are transiently recruited in the first few days of cold stress [45, 54, 55]. Subsequently, genetic tracing and fate mapping studies established that brown adipocytes arise from an interstitial stromal cell population that expresses PDGFRA in brown adipose tissue [37, 65, 66].

Our scRNA-seq data clearly demonstrate that ASC1 cells are the immediate progenitors of BA in iBAT. Thus, proliferating/differentiating cells expressed ASC1 markers, but not ASC2 or ASC3 markers. In addition, smFISH analysis demonstrated that a high proportion of actively differentiating cells that express *Nnat* co-express the ASC1 marker *Bmper*. Some proliferating ASC1 cells proceeded along an adipogenic trajectory, upregulating markers such as *Car3*, *Adipoq*, and *Plin1*, while some proliferating cells did not. These non-differentiating cells could function to maintain populations of ASC1 cells in iBAT. What determines these different cells fates is not known, but our data suggests that microenvironmental factors, such as proximity to recruited immune cells, could play a role.

While this work was in progress, Shamsi, *et al.* published scRNA-seq data of iBAT from cold-exposed mice suggesting that *Trpv1*<sup>+</sup> vascular smooth muscle cells give rise to BA [73]. In contrast, our data only identified adipogenic differentiation from *Pdgfra*<sup>+</sup> ASCs by scRNA-seq, smFISH, and genetic tracing. We believe that key differences in experimental design might have contributed to these differences in results and



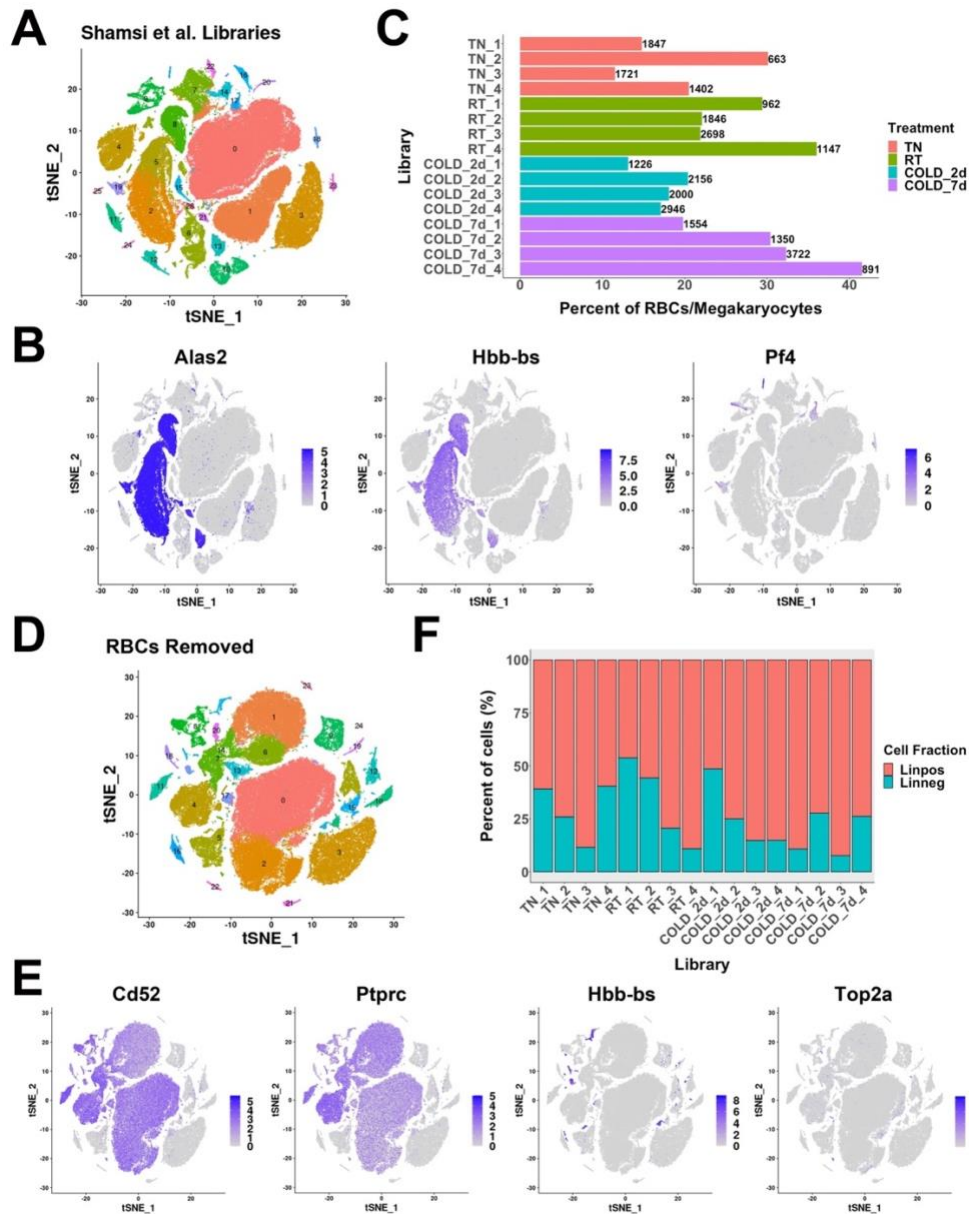
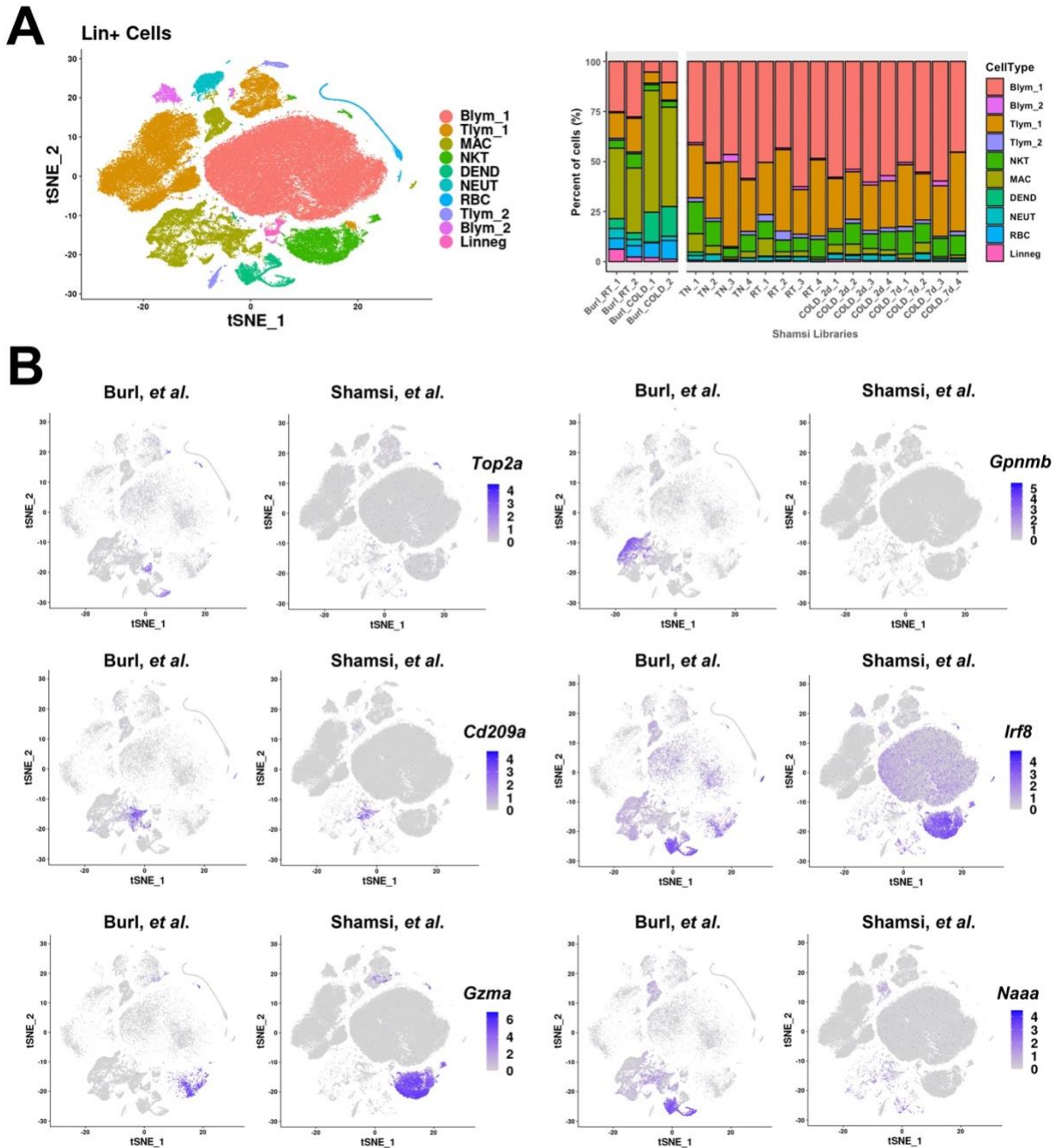


**Figure 29. Analysis and subsetting of Shamsi, *et al.* mouse iBAT scRNA-seq data** (A) t-SNE plot of 137,868 iBAT SVF cells profiled with scRNA-seq by Shamsi, *et al.* Cells come from mice housed at thermoneutral, room temperature, 2 days of cold exposure (5°C), and 7 days of cold exposure (5°C). This data consists of 16 scRNA-seq libraries, prepared from four individual mice per treatment group. Clustering applied to the t-SNE plot identified 26 clusters, highlighted in different colors. (B) t-SNE plots displaying the log<sub>2</sub> expression levels for genes to identify red blood cells and megakaryocytes. (C) Bar graph displaying the percent of RBCs/megakaryocytes per single-cell library. Numbers at the end of bars correspond to the number of RBCs/megakaryocytes in the corresponding library. (D) t-SNE plot of iBAT SVF cells from (A) after filtering out RBCs and megakaryocytes. This t-SNE plot contains 109,737 cells. Clustering applied to the t-SNE plot identified 24 clusters, highlighted in different colors. (E) t-SNE plots displaying the log<sub>2</sub> expression levels for genes to identify immune cells, red blood cells, and proliferating cells. (F) Bar graph displaying the percent of immune versus non-immune cells in each library.

interpretation. Therefore, we compared our scRNA-seq to the data collected by Shamsi, *et al.* We noted significant differences in the proportions of cells captured, which led us to compare different digestion methods with scRNA-seq.

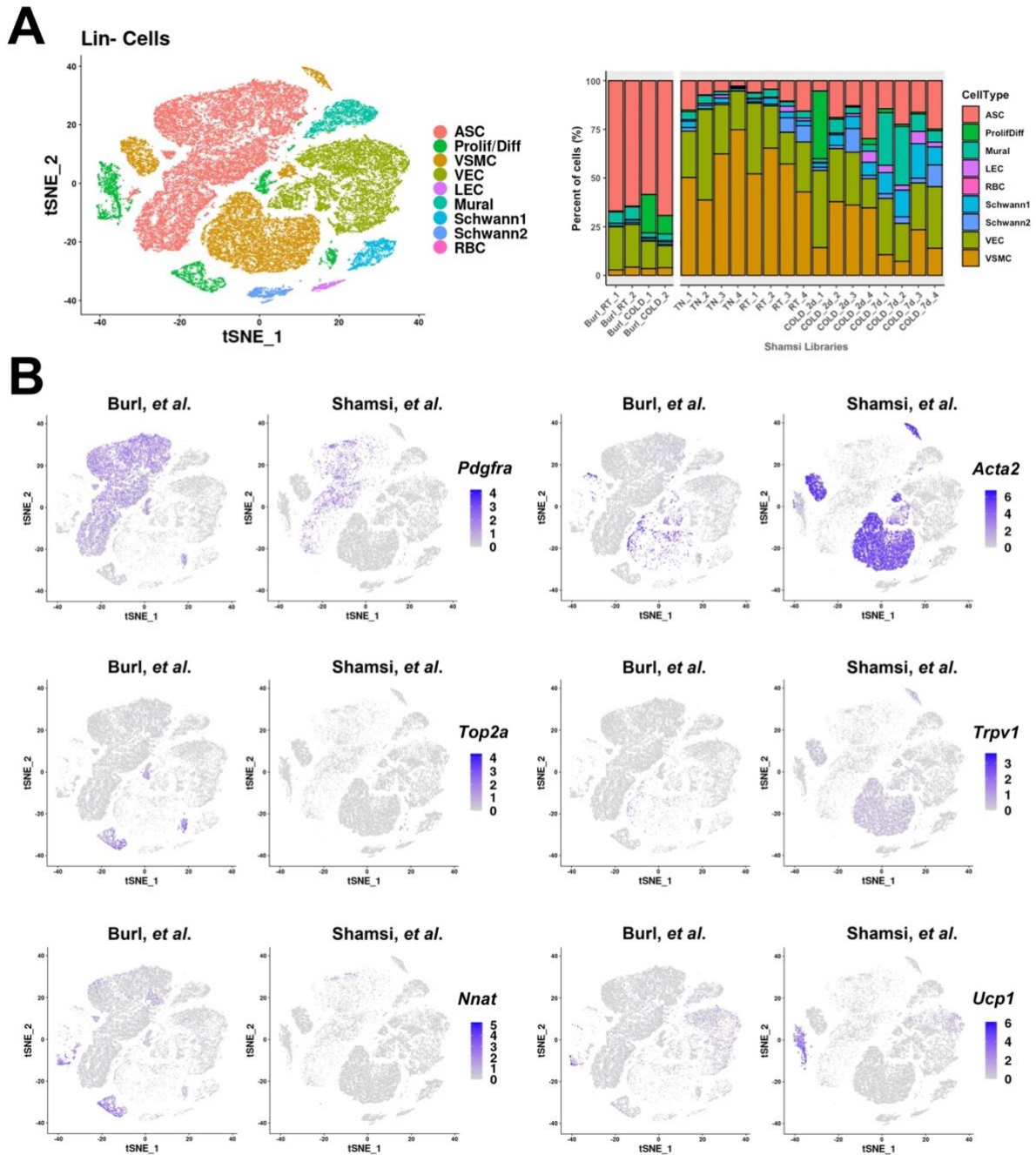
## 5.2 Integration of iBAT scRNA-seq data with the Shamsi, *et al.* cold exposure iBAT single-cell data

First, we examined the Shamsi, *et al.* single-cell data [73]. Single-cell libraries were prepared from mouse iBAT total SVF cells collected from mice housed at thermoneutral (30°C), room temperature, or cold (5°C) for two days or seven days. Four libraries were prepared per condition, each from individual mice, for a total of 16 scRNA-seq libraries. To directly compare these libraries to our iBAT data, we processed these libraries using the same workflow to generate the individual count files, using cellranger and SoupX. Shamsi, *et al.* libraries range from 2,453 to 18,211 cells per library. Libraries were quality filtered to the same specifications as our iBAT libraries: percent mitochondria < 10, number of counts per cell < 15,000, and number of genes per cell < 4,000. This was more stringent than the filtering conducted for the Shamsi, *et al.* manuscript. Clustering identified 26 clusters of iBAT SVF cells (**Figure 29A**). We removed clusters of red blood cells (RBCs), which have high expression of 5'-aminolevulinate synthase 2 (*Alas2*) and hemoglobin beta adult s chain (*Hbb-bs*), and clusters of megakaryocytes, which have high expression of platelet factor 4 (*Pf4*) (**Figure 29B**). RBCs and megakaryocytes comprised between 11.5% to 41.5% of cells in each library (**Figure 29C**). With RBCs and megakaryocytes removed, we reclustered the data (**Figure 29D**). Because this data is from iBAT total SVF, we separated the data into immune and non-immune cells to



cluster with our Lin+ and Lin- data. Using CD52 molecule (*Cd52*) and protein tyrosine phosphatase receptor type C (*Ptprc*) to distinguish immune cells, we separated immune and non-immune clusters, as well as remove any additional clusters of RBCs (**Figure 29E**). The proportion of immune and non-immune cells captured varied by library, ranging from 46.2% to 92.3% of cells being *Cd52+Ptprc+* immune cells (**Figure 29F**). Notably, we didn't observe any clusters exhibiting expression of proliferation makers, like *Top2a* (**Figure 29E**).

We integrated the Shamsi, *et al.* data with our iBAT single-cell libraries (**Figure 30**). Integration demonstrated significantly different composition of cells that were captured (**Figure 30A and Supplementary Table S8A**). Starting with the immune cells, integrated immune cell data identified ten clusters, including B lymphocytes (Blym), T lymphocytes (Tlym), macrophages (MAC), dendritic cells (DEND), natural killer T-cells (NKT), and neutrophils (NEUT). Immune cells from the Shamsi, *et al.* libraries were overwhelming lymphocytes (Blym, Tlym, NKT), making up 93.6% of the immune cells, compared to our single-cell libraries where lymphocytes are only 33.5% of the cells (**Figure 30A**). The majority of immune cells captured in our iBAT single-cell libraries were macrophages and dendritic cells (MAC and DEND). Both of these cell types are a combined 54.1% of the immune cells in our libraries, compared to only 4.0% in the Shamsi, *et al.* libraries. Notably, there was negligible expression of proliferation marker *Top2a* or the MAC1 lipid-handling macrophage marker *Gpnmb* in the Shamsi, *et al.* immune cells (**Figure 30B**). However, they did capture a small population of *Cd209a+* cells, which corresponds to DEND2 monocyte-derived macrophages in our data. While we profiled a population of



*Irf8+Naaa+* DEND1 conventional dendritic cells, *Irf8* expression in the Shamsi, *et al.*, data instead appears to be expressed in a population of *Gzma+* NKT cells (**Figure 30B**).

Examining the non-immune cells, we find significantly different proportions of cells (**Figure 31A and Supplementary Table S8B**). Nine clusters of cells were identified, including ASCs, proliferating/differentiating cells (ProlifDiff), vascular smooth muscle cells (VSMC), vascular endothelial cells (VEC), lymphatic endothelial cells (LEC), mural cells (Mural), Schwann cells (Schwann), and RBCs. Our data included primarily ASCs, making up 64.8% of the cells in the libraries. The Shamsi, *et al.* data only included 13.3% ASCs in their libraries. In contrast, the Shamsi *et al.* data included primarily vascular cells (VECs and VSMCs), comprising 65.6% of the cells, compared to our data where the average was 21.0%. Both data contained cells that clustered together by markers of proliferation and adipogenic differentiation (Prolif/Diff) (**Figure 31A**). However, cells in this cluster from the Shamsi, *et al.* data do not express proliferation markers (*Top2a*), or markers of early differentiation (*Nnat*), but have high expression of the BA marker *Ucp1* (**Figure 31B**). Interestingly, the majority of the cells in the proliferating/differentiating cluster from the Shamsi, *et al.* data come from a single library from cold exposed mice, COLD\_2d\_1, where they are 34.8% of the non-immune cells (**Figure 31A**). In the other two day cold libraries, proliferating/differentiating cells are only 1.5% of the cells, which is approximately the same percentage as the 7 day cold libraries at 1.2% (**Figure 31A**). In our libraries, obtained from 4 day cold-exposed mice, cells in the proliferating/differentiating cluster made up 14.6% of the total non-immune cells (**Figure 31A**). Our data captured populations of proliferating/non-differentiating (*Pdgfra+/Top2a+*) and proliferating/differentiating (*Pdgfra-/Top2a+/Nnat+*) cells, as well as a small

population of *Ucp1*+ cells (**Figure 31B**), which includes every state along the proposed adipogenic trajectory. *Trpv1* was co-expressed in *Acta2*+ VSMCs, and did not overlap with proliferating/differentiating cells (**Figure 31B**).

Despite being from the same tissue, these scRNA-seq data contain very different proportions of SVF cells. The Shamsi, *et al.* dataset does not contain any evidence of stromal cell proliferation, which is thought to be the basis of brown adipose tissue neogenesis [37, 54, 55, 64].

### **5.3 iBAT digestion method alters proportions of cells profiled with scRNA-seq**

We hypothesized that the differences in cell type proportion were likely due to numerous differences in isolation protocols, including dissociating enzymes, debris cleanup, and centrifugation speeds [73]. We therefore decided to compare two methods of iBAT cell isolation (collagenase type II versus dispase + collagenase type I) using scRNA-seq on all isolated cells. Collagenase type II is the digestion enzyme we used, while the Shamsi, *et al.* protocol used dispase and collagenase type I. To compare, we only changed the tissue digestion method and kept the rest of the protocols identical (see Methods). We isolated total stromal cells from mice housed at room temperature (22°C) or housed at 6°C for four days. We found that the method of isolation greatly affects the proportions of cells that are isolated from iBAT (**Figure 32A-B and Supplementary Table S9A**). As anticipated, tissue digestion with collagenase type II, which is the method used in our dataset, captured majority ASCs (52%). Digestion with dispase and collagenase type I profiled majority VECs (66%) (**Figure 32A-B**). Apart from the VECs, digestion with dispase and collagenase type I, captured the same cell types as digestion with

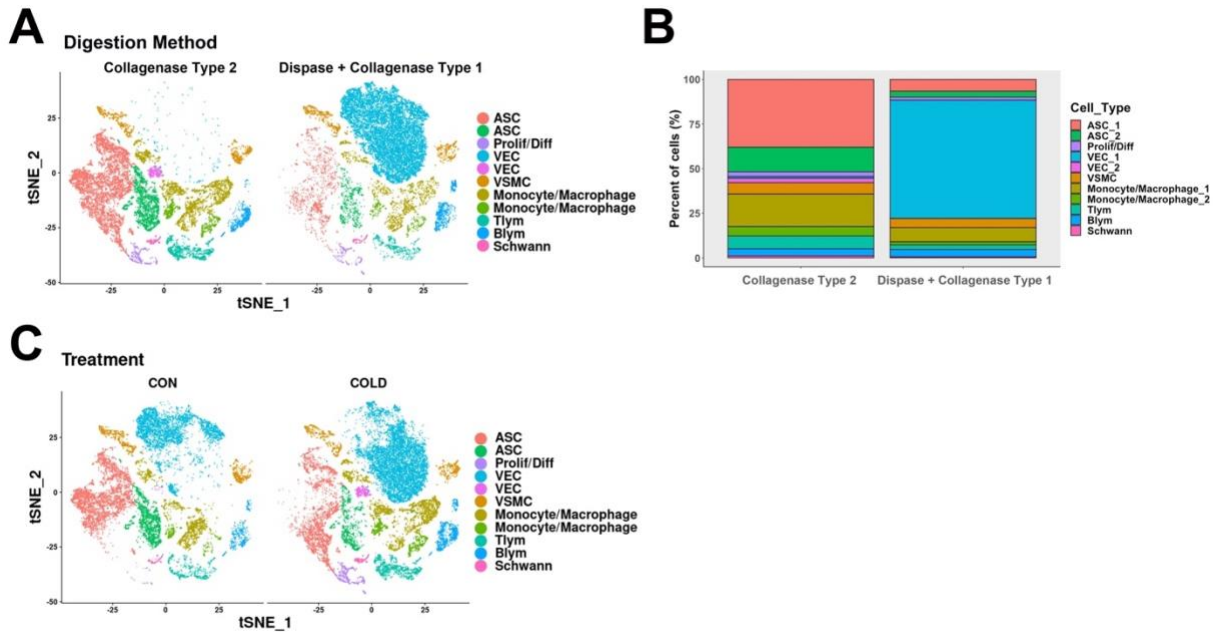


**Figure 32. iBAT digestion method affects proportions of SVF cells profiled with scRNA-seq** (A) t-SNE plot of 37,514 stromal vascular cells from mouse iBAT digested with different enzymes: Collagenase Type 2, or Dispase + Collagenase Type 1. These plots contain mice housed at room temperature or 6°C for four days. Clustering applied to the t-SNE plot identified 11 clusters, highlighted in different colors. ASC, adipose tissue stromal cell; Prolif/Diff, proliferating/differentiating cells; VEC, vascular endothelial cells; VSMC, vascular smooth muscle cells; Tlym, T lymphocytes; Blym, B lymphocytes; Schwann, Schwann cells. DEGs for each cluster are presented in Supplementary Table S9A. (B) Bar graph of cell type proportions corresponding to each digestion method. (C) t-SNE plot from (A), split into libraries corresponding to different treatments: room temperature controls (CON) and mice housed at 6°C for 4 days (COLD).

collagenase type II (ie. ASCs, VSMC, differentiating cells, immune cells), but at much lower numbers due to the abundance of VECs. Collagenase type II captured ~3% VECs of the total SVF.

To gain a better resolution of captured cell types, we subset immune and non-immune cells and reclustered the data. Both digestion methods captured the same immune cell types, and in similar proportions (**Figure 33A-B** and **Supplementary Table S9B**), including cold-induced macrophages (MAC1) and dendritic cells (DEND1-3) (**Figure 33C**). Both methods also captured proliferating immune cells (**Figure 33C**). Reclustering ASCs and differentiating cells distinguished the same three ASC subtypes and pointed to



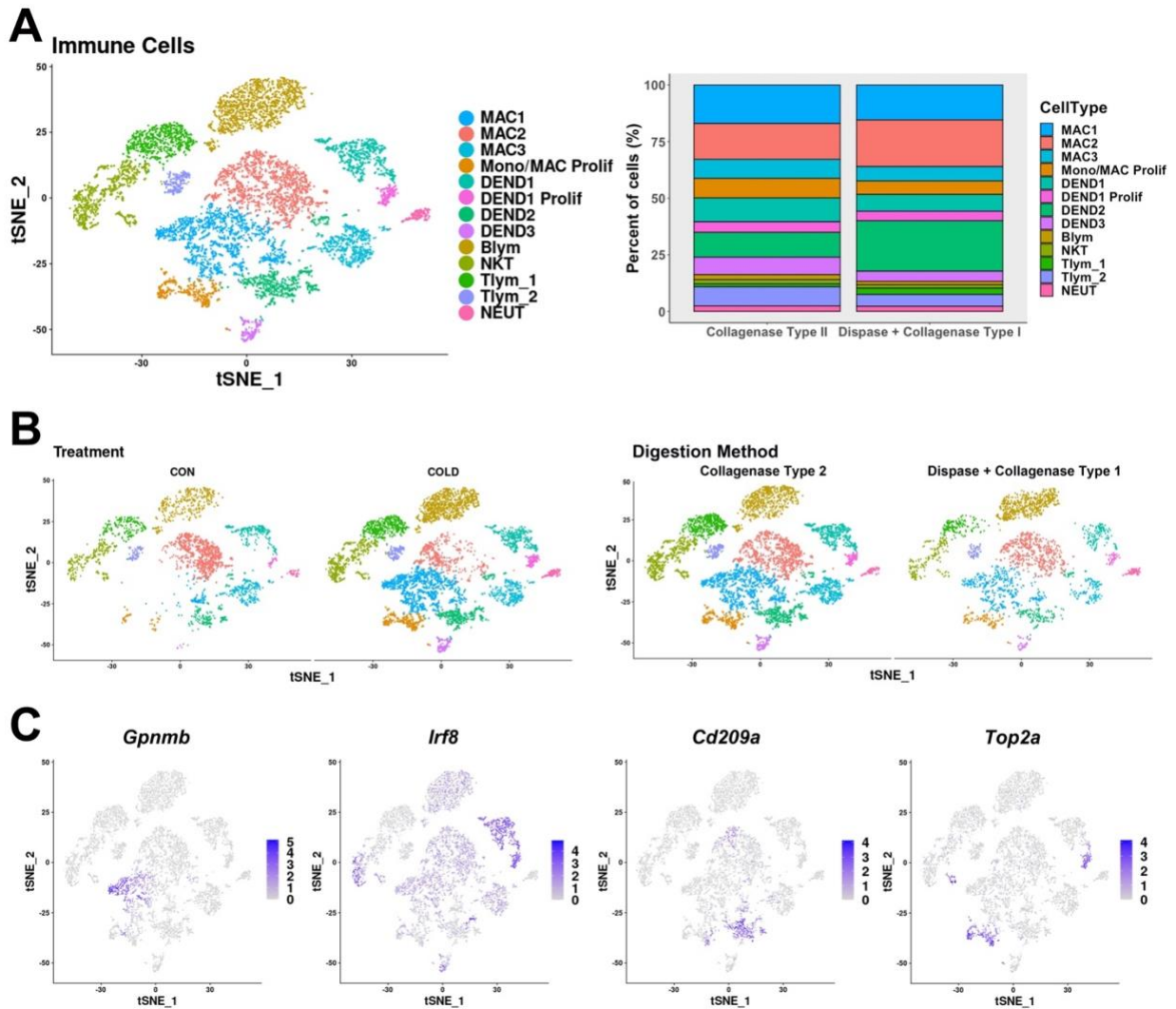


**Figure 33. Different iBAT digestion methods capture similar proportions of immune cells** (A) t-SNE plot of 8,680 immune cells from mouse iBAT, reclustered from the immune cells in Figure 32A. Clustering applied to the t-SNE plot identified 13 clusters, highlighted in different colors. Bar graph of cell type proportions corresponding to each digestion method. MAC, macrophages; Mono/MAC Prolif, proliferating monocytes/macrophages. DEND, dendritic cells; DEND1 Prolif, proliferating DEND 1 dendritic cells; Blym, B lymphocytes; NKT, natural killer T cells; Tlym, T lymphocytes; NEUT, neutrophils. DEGs for each cluster are presented in Supplementary Table S9B. (B) t-SNE plot from (A), split into libraries corresponding to different treatments (CON and COLD) or different digestion methods (Collagenase Type 2 or Dispase + Collagenase Type 1). (C) t-SNE plots displaying the log<sub>2</sub> expression levels for genes to identify specific immune cell subtypes and proliferating cells.

ASC1\_cold-activated cells and the direct precursors of differentiating adipocytes

(Figure 34A-B and Supplementary Table S9C). In the cluster of proliferating and

differentiating cells, some cells expressed markers of proliferation only (*Birc5*), while

some expressed proliferation and differentiation markers (*Car3*, *Adipoq*) (Figure 34C). Differentiating cells downregulate expression of ASC marker *Pdgfra* (Figure 34C). More terminally differentiated cells were captured, that show high *Ucp1* expression (Figure 34C).

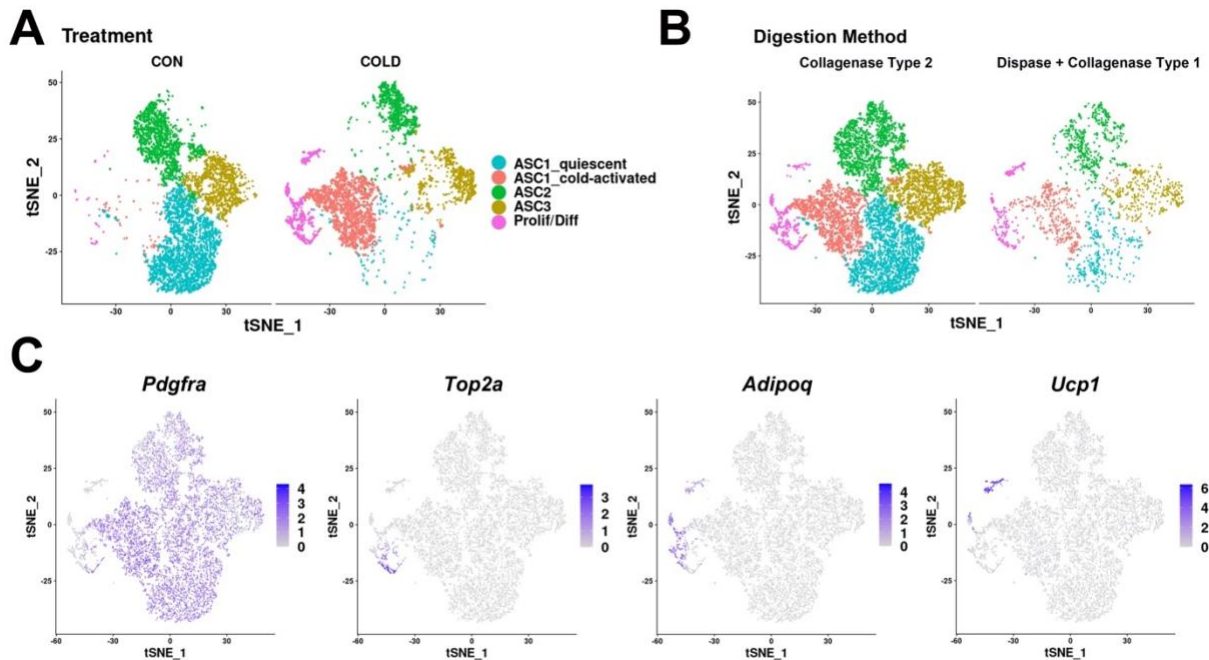


**Figure 34. Different iBAT digestion methods retain cold-activated ASCs and cells undergoing adipogenic differentiation** (A) t-SNE plot of 10,989 ASCs from mouse iBAT, reclustered from the ASC clusters in Figure 32A. This t-SNE plot is split into cell from mice from different treatments. Clustering applied to the t-SNE plot identified five clusters, highlighted in different colors. ASC, adipose tissue stromal cell; Prolif/Diff, proliferating/differentiating cells. DEGs for each cluster are presented in Supplementary Table S9C. (B) t-SNE plot from (A), split into libraries corresponding to different digestion methods: Collagenase Type 2 or Dispase + Collagenase Type 1. (C) t-SNE plots displaying the log2 expression levels for genes to identify ASCs and proliferating/differentiating cells.

## Chapter 6. Manipulation of immune cell types in brown adipose tissue

### 6.1 Introduction

Cold triggers the appearance of multiple immune cell types in iBAT, including populations of lipid-handling macrophages (MAC1) and dendritic cells (DEND1-4). Recruitment of these immune subtypes is highly correlated with proliferation of adipocyte progenitors. To better understand the causal relationship between immune cell recruitment and progenitor proliferation, our goal was to manipulate immune cell populations *in vivo* and observe the effect on cell proliferation. scRNA-seq was used to identify potential gene targets, or detail how specific cell types might be genetically targeted. Presented here are the results for three immune cell models.

### 6.2 Ccr2 KO does not affect proliferation or immune cell recruitment

C-C motif chemokine receptor 2 (CCR2) is a chemokine receptor expressed on monocytes and T lymphocytes which directs their recruitment to tissues [157-159]. Eliminating *Ccr2* expression could prevent infiltration of key macrophage and dendritic cell subpopulations involved in iBAT neogenesis. In our iBAT single-cell data, *Ccr2* is expressed in the macrophages, dendritic cells, and NKT cells (**Figure 35A**). In addition, common *Ccr2* ligands like *Ccl8*, *Ccl2*, *Ccl11*, and *Ccl7* are expressed in different iBAT cell subtypes. *Ccl8*, *Ccl2*, and *Ccl7* are expressed in ASCs and certain subtypes of macrophages. *Ccl11* is highly expressed in ASC1. Therefore, CCR2 signaling could be a possible mechanism for immune cell recruitment (**Figure 35A**). To investigate the role of *Ccr2* in the recruitment of cold-induced macrophages and dendritic cells, and the potential effect on adipocyte proliferation and differentiation, we used a *Ccr2*<sup>gfp/gfp</sup> knock-in/knock-out (KI/KO) mouse model. Heterozygous mice were used as controls. iBAT was collected

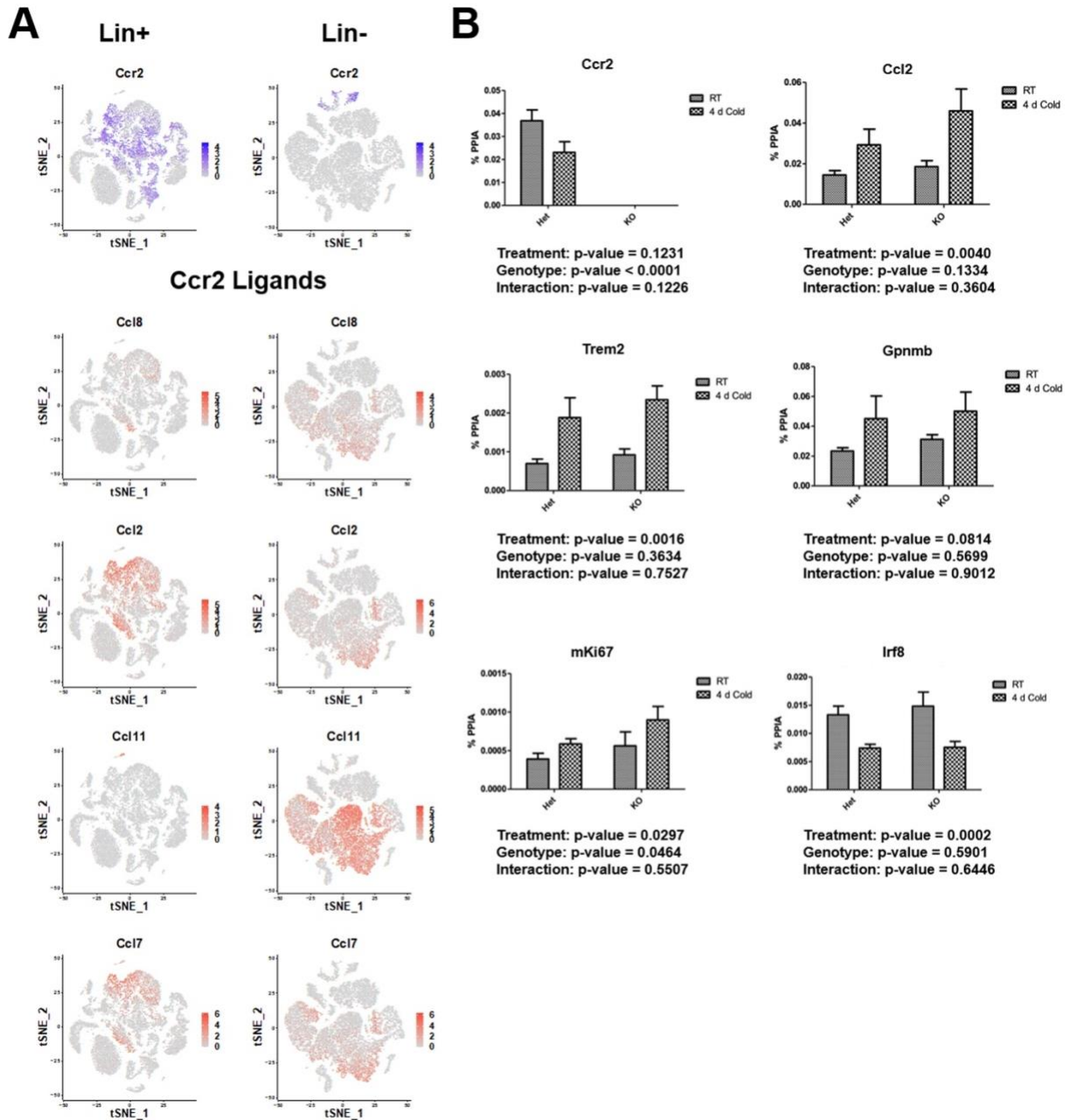


**Figure 35. *Ccr2* KO does not affect cold-induced immune cell recruitment or proliferation** (A) t-SNE plots of our iBAT scRNA-seq Linpos and Linneg data, showing log<sub>2</sub> gene expression of *Ccr2* and its associated ligands. (B) Quantitative PCR analysis of proliferation and immune cell activation genes in iBAT of *Ccr2* heterozygous (Het) or *Ccr2* KO (KO) mice maintained at room temperature or exposed to cold for four days (n = 6-10 per condition; mean ± SE). p-values are from 2-way ANOVA analysis.

from mice maintained at room temperature, or after four days at 6°C. qPCR analysis of RNA from iBAT confirmed *Ccr2* knockout, but we observed no change in gene expression

for key immune and proliferation markers (**Figure 35B**). While *Ccr2* and its associated ligands are expressed in iBAT during cold-induced neogenesis, the mechanism of macrophage and dendritic cell recruitment does not appear to be *Ccr2* dependent.

### **6.3 Diphtheria toxin receptor model system was ineffective in knocking down immune cell populations *in vivo***

Another method for manipulating immune cells *in vivo* uses a diphtheria toxin receptor (DTR) inducible system that transiently depletes cell types depending on promoter-specific expression [160-162]. Expression of the DTR under the control of specific immune cell promoters allow diphtheria toxin (DT) to selectively deplete subpopulations of immune cells. For our purposes, we used mice that express DTR under the control of the integrin subunit alpha M (*Itgam*) promoter (ITGAM-DTR) [160]. In the single-cell data, *Itgam* (CD11b) is expressed in all macrophages clusters, and the cold-responsive monocyte-derived dendritic cells (DEND2) (**Figure 36A**). The genotyping protocol for the ITGAM-DTR mice amplified the transgene, which had the expected product size of 625 bp (**Figure 36B**). This PCR product was confirmed to be identical to diphtheria toxin receptor mRNA.

In order to test CD11b<sup>+</sup> cell knockdown in ITGAM-DTR mice, we tested mouse whole blood after DT injection using flow cytometry. PBS injection was used as a control, and concentrations of 25 ug/kg or 50 ug/kg DT were administered i.p. approximately 20 hours before sacrifice and blood collection. Of the viable leukocytes captured, the percentage of CD11b<sup>+</sup> cells was 28.3% for the PBS-injected mouse, 48.7% for the 25 ug/kg DT-injected mouse, and 56.3% for the 50 ug/kg DT-injected mouse (**Figure 36C**), providing no evidence of CD11b<sup>+</sup> cell depletion. Finally, we tested the response of ITGAM-DTR

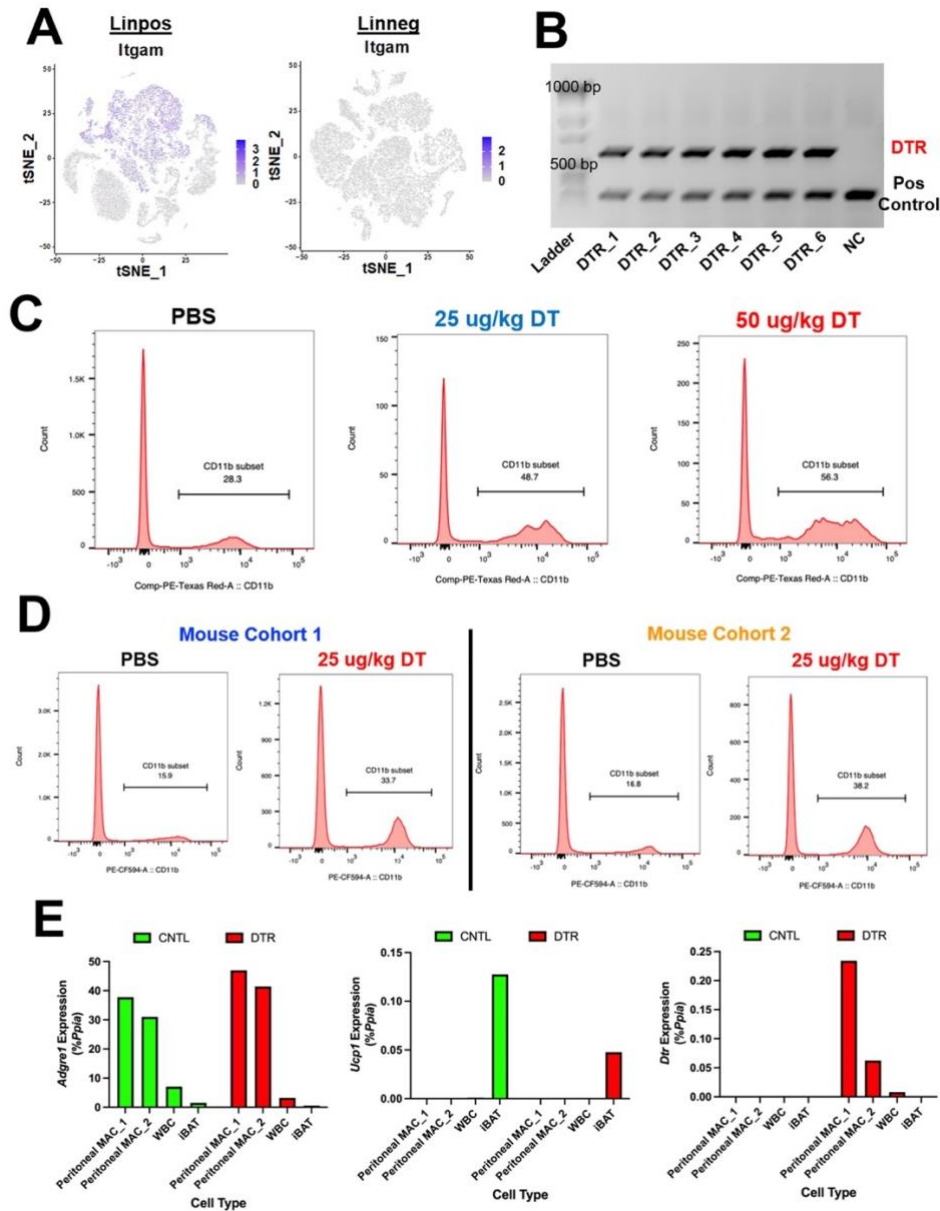


**Figure 36. ITGAM-DTR mouse model was unsuccessful in knocking down CD11b+ cells** (A) t-SNE plots of our iBAT scRNA-seq Linpos and Linneg data showing log<sub>2</sub> gene expression of *Itgam*, the promoter expressing *Dtr*. (B) Ethidium bromide agarose gel electrophoresis showing results of PCR genotyping for *Dtr* (625 bp) and a positive control (200 bp). Each PCR product corresponds to a different individual mouse. NC, negative control. (C) Representative histogram of flow cytometry (FACS) analysis of CD11b+ cells from mouse whole blood represented in a single parameter histogram. Animals were ITGAM-DTR mice injected i.p. with either PBS, 25 ug/kg diphtheria toxin (DT), or 50 ug/kg DT. (D) Representative histogram of flow cytometry (FACS) analysis of CD11b+ cells from mouse whole blood represented in a single parameter histogram. CD11b+ cells were quantified after gating for cell viability. Animals were ITGAM-DTR mice from two independent cohorts, injected i.p. with either PBS or 25 ug/kg DT. (E) Quantitative PCR analysis of proliferation and immune cell activation genes in different cell fractions (n = 1 per condition). Peritoneal MAC, peritoneal macrophages; WBC, white blood cells.

mice in our colony (Mouse Cohort 1) to the same strain of mice from a colony in a different lab (Mouse Cohort 2). The colonies were independent of one another, started from separate mice purchased from The Jackson Laboratory, and mice from Cohort 2 had previously been used in a published study where they achieved CD11b<sup>+</sup> cell knockdown [163]. Although, at the time of these experiments, Cohort 2 mice were not actively being used for experiments. PBS injection was used as a control. For DT injection, the same aliquot and concentration of DT that was published for Cohort 2 (25 ug/kg) was used. Flow cytometry analysis of mouse blood showed no CD11b<sup>+</sup> cell knockdown in ITGAM-DTR mice injected with DT (**Figure 36D**). The percentage of viable leukocytes that were CD45<sup>+</sup>CD11b<sup>+</sup> was higher in the DT injected mice than the PBS controls in mice from both cohorts (15.9% vs. 33.7% in Mouse Cohort 1, and 16.8% vs. 38.2% in Mouse cohort 2) (**Figure 36D**). This suggests that ITGAM-DTR mice from both colonies are not achieving CD11b<sup>+</sup> cell knockdown with DT administration. Finally, we checked expression of *Dtr* in these mice, RNA was isolated from specific cell populations in either scrub mice or ITGAM-DTR mice. To enrich for macrophages, peritoneal macrophages and immune cells from whole blood were collected. This was compared to RNA from whole iBAT. Peritoneal cell prep captured a large number of macrophages based on *Adgre1* (F4/80) gene expression (**Figure 36C**). Despite capturing a measurable amount of *Adgre1*-expressing macrophages, a cell type expressing the *Dtr*, we observed very low *Dtr* gene expression (**Figure 36E**). *Ucp1* gene expression was used as a control for iBAT (**Figure 36E**).

Unfortunately, there was no evidence that the ITGAM-DTR mice in our colony were successful in knocking down CD11b+ monocytes/macrophages with DT administration. The problem appears to be with DTR expression, and not a change in the gene sequence.

#### **6.4 Effects of systemic or tissue-targeted clodronate liposomes injection in mice**

Apart from genetic models for immune cell manipulation, injecting animals with clodronate-containing liposomes knocks down phagocytic immune cell types *in vivo* [164-167]. Liposomes are artificially manufactured spheres with a phospholipid bilayer that can be used to encapsulate fluorescent compounds or chemicals. Clodronate is hydrophilic, and can be encapsulated within the liposomes. Once phagocytic immune cells engulf the clodronate-containing liposomes, accumulation of intracellular clodronate levels will initiate apoptosis. Different methods of injection can be used to differentially target tissues for macrophage depletion.

The goal was to use clodronate liposomes with our cold exposure model to study how immune cells contribute to cold-induced neogenesis. First, we injected C57 mice i.p. with clodronate-containing liposomes on the second day of cold exposure. This is the time when we observed upregulation of immune markers in whole tissue RNA-seq. PBS-liposomes were used as the injection control, and animals housed at room temperature were the control from cold exposure. Animals were sacrificed two days after the injection. However, we observed that animals injected with clodronate liposomes in the cold became very frail, with some dying before the fourth day of cold exposure. Documenting the mouse weight, we observed that all animals, even those housed at room temperature, lost weight with clodronate liposome injection (**Figure 37A**). It appeared that animals were unable to tolerate the added stress of cold exposure along with clodronate liposome



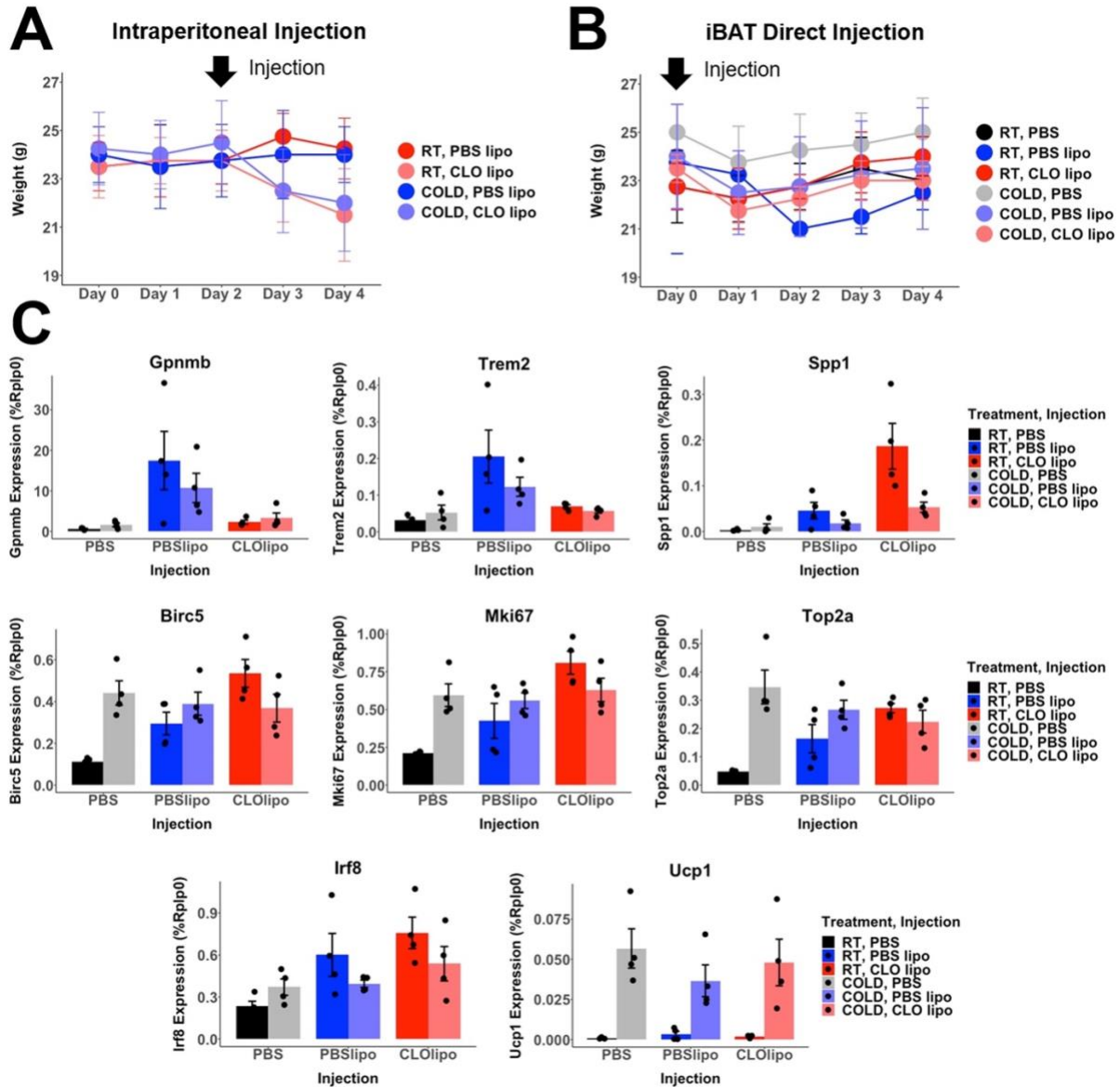


**Figure 37. Quantitative PCR demonstrates that liposome direct injection into mouse iBAT recruits immune cells** (A) Record of mouse weight during intraperitoneal injection of PBS-containing or clodronate-containing liposomes. Mice were maintained at room temperature, or exposed to cold for four days ( $n = 4$  per condition; mean  $\pm$  SD). (B) Record of mouse weight during direct injection of sterile PBS, PBS-containing liposomes, or clodronate-containing liposomes into mouse iBAT. Following injection surgery, mice were maintained at room temperature or exposed to cold for four days ( $n = 4$  per condition; mean  $\pm$  SD). (C) Quantitative PCR analysis of proliferation and immune cell activation genes in iBAT of mice from liposome direct injection experiment ( $n = 4$  per condition; mean  $\pm$  SE).

injection. We therefore decided to modify our experimental strategy.

As an alternative strategy, we decided to directly inject liposomes into iBAT as a way to minimize the effects of clodronate throughout the body [168-171]. We directly injected either sterile PBS, PBS-containing liposomes, or clodronate-containing liposomes into iBAT. Once animals had fully recovered from the procedure, they were housed at room temperature, or placed at 6°C for four days. All animals in the study survived, and monitoring mouse weight showed that clodronate-injected animals had no extreme weight loss (**Figure 37B**). Surprisingly, quantitative PCR analysis of mouse iBAT showed that expression of cold-induced macrophage markers *Gpnmb* and *Trem2* was much higher in iBAT injected with PBS liposomes compared to PBS injected tissue (**Figure 37C**). iBAT injected with clodronate liposomes showed lower expression of *Gpnmb* and *Trem2* than in PBS-injected liposomes, suggesting that these cells were knocked down with clodronate. Expression of proliferation markers *Birc5*, *Mki67*, and *Top2a* was higher in liposome-injected mice housed at room temperature than PBS-injected controls, but expression was comparable in cold exposed mice for all injections (**Figure 37C**). Levels of *Irf8*, a dendritic cell marker, were elevated in mice injected with either type of liposome, suggesting that liposomes recruit dendritic cells but do not deplete them (**Figure 37C**).

Histological examination of iBAT from mice housed at room temperature and injected with PBS liposomes, we observed what appears to be a foreign body reaction, presumably near the site of liposome injection (**Figure 38A**). This reaction was not observed in room temperature mice injected with sterile PBS (**Figure 38A**). The foreign body reaction contained PDGFRA+, MHCII+, GPNMB+, and mKi67+ cells (**Figure 38A**), with PI16+ cells around the border (**Figure 38B**). PI16+ ASCs comprise the fascia,

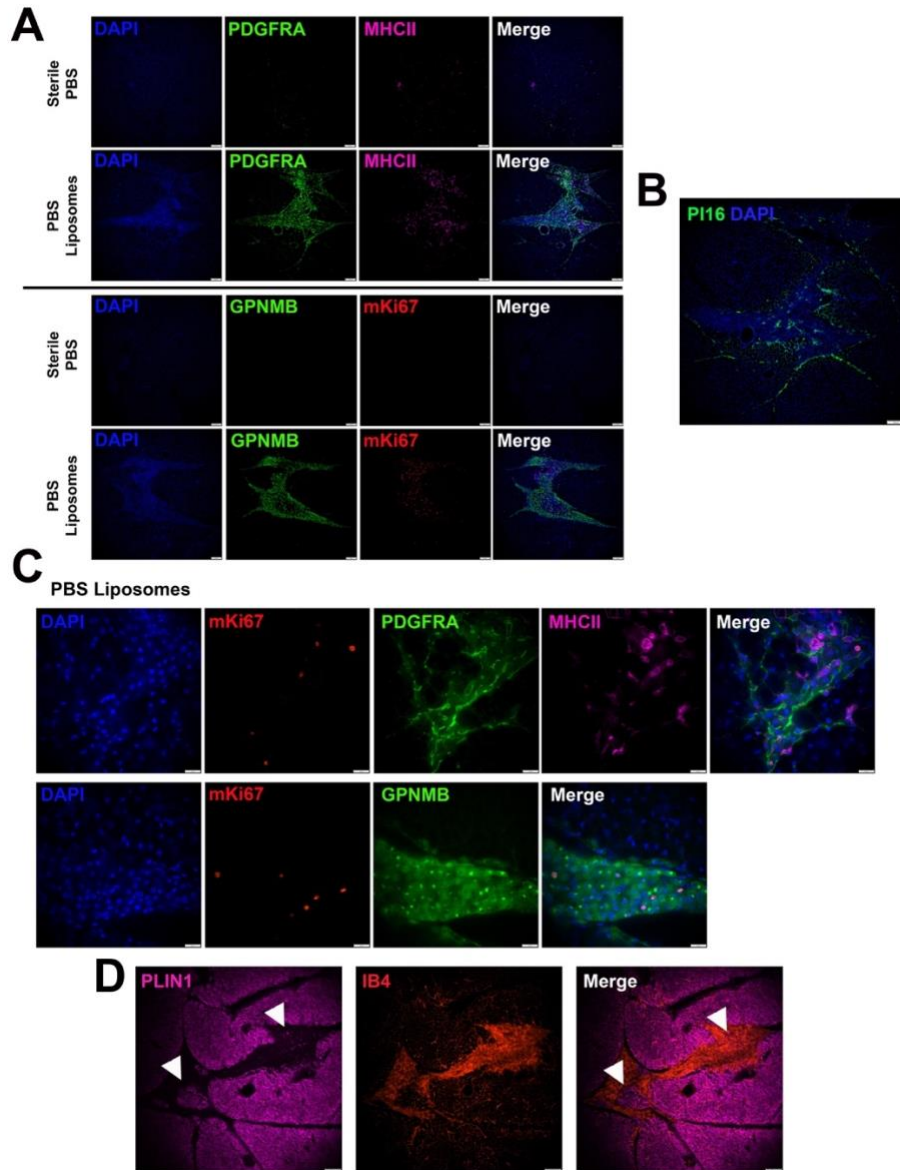


**Figure 38. Direct-injection of liposomes causes a foreign body reaction that recruits immune cells and induces proliferation** (A) Low-magnification images of fixed-frozen sections from room temperature mouse iBAT directly injected with either sterile PBS or PBS-containing liposomes. Sections were stained for PDGFRA (green) and MHCII (pink), or GPNMB (green) and mKi67 (red), and nuclei were counterstained with DAPI. Scale bar, 100  $\mu$ m. (B) Low-magnification images of fixed-frozen sections from room temperature mouse iBAT directly injected with PBS-containing liposomes. Sections were stained for PI16 (green) and nuclei were counterstained with DAPI. Scale bar, 100  $\mu$ m. (C) Higher-magnification images in the area of the foreign body reaction. iBAT fixed-frozen sections from room temperature mice directly injected with PBS-containing liposomes. Sections were stained with either PDGFRA (green), mKi67 (red), and MHCII (pink), or GPNMB (green) and mKi67 (red). Nuclei were counterstained with DAPI. Scale bar, 20  $\mu$ m. (D) Low-magnification images of fixed-frozen sections from room temperature mouse iBAT directly injected with PBS-containing liposomes. Sections were stained for PLIN1 (pink) and IB4 (red). Arrows indicate areas of PLIN1+ cells in the area of the foreign body reaction. Scale bar, 100  $\mu$ m.

which encapsulates the tissue lobules. It is possible that PI16+ cells are encapsulating the foreign material. At higher magnification, mKi67+ cells were GPNMB+ macrophages, as opposed to PDGFRA+ ASCs or MHCII+ dendritic cells (**Figure 38C**). We also noted PLIN1+ cells with an adipocyte-like morphology that were present in the area of this reaction (**Figure 38D**), although it is difficult to say if these are newly differentiated adipocytes or an artifact of tissue sectioning.

In summary, i.p. injection of clodronate liposomes is not well tolerated in mice that are cold-stressed. Unexpectedly, the liposomes themselves triggered a response after direct injection of liposomes into mouse iBAT. This makes the data difficult to interpret. Although, it is interesting that injection of liposomes was sufficient to recruit GPNMB+ and MHCII+ cells.

## Chapter 7. Discussion

### 7.1 Single-cell analysis of eWAT and iWAT discussion

Single-cell analysis of eWAT and iWAT after ADRB3 stimulation demonstrate the power of scRNA-seq to deconvolve stromal cell heterogeneity and to infer adipogenic trajectories [97]. scRNA-seq identifies distinct ASC subpopulations in mouse WAT that differentially express genes related to ECM remodeling, which also appear to be differentially poised to enter the adipogenic pathway. Comprehensive and unbiased scRNA-seq of ASC indicates induction of *de novo* adipogenesis by ADRB3 activation is a prominent feature of epididymal, but not inguinal WAT. Lastly, we have made the primary and processed data sets from these experiments, more than 33,000 cells total, publicly available as a resource for mining and further analysis.

WAT single-cell analysis identified two main types of ASCs: ASC 1 and ASC 2. Since the time of publication, additional WAT scRNA-seq libraries have been published that validate the heterogeneity of *Pdgfra*<sup>+</sup> ASCs [136-138, 172, 173]. A review integrating scRNA-seq stromal cell libraries from mouse eWAT and iWAT by Rondini and Granneman confirmed two ASC subtypes in eWAT, and additionally resolved three ASC subtypes in iWAT [140]. Importantly, immunohistochemistry from that review and a paper by Merrick, *et al.* demonstrated that these subtypes occupy distinct regions of the tissue. ASC2 cells (PDGFRA<sup>+</sup>, DPP4<sup>+</sup>, Pi16<sup>+</sup>) were restricted mainly to the fascia layer surrounding tissue, while ASC1/ASC3 cells (PDGFRA<sup>+</sup>, DPP4<sup>-</sup>, Pi16<sup>-</sup>) were found throughout the parenchyma body and in areas surrounding vessels [137, 140]. ASC subtypes differentially expressed genes for secreted ECM proteins and receptors, as well as paracrine signaling actors regulated to the TGF- $\beta$  superfamily.

Single Cre recombinase drivers for genetic tracing have been employed in adipose tissue to identify stromal cell types with adipogenic potential. However, without knowing all the cell types that express a given driver, it is unclear how many different cell types are being traced. scRNA-seq allows for better assessment of driver specificity. Unbiased profiling of mouse eWAT SVF cells demonstrates that *Pdgfra* is the best marker to define the population of adipogenic cells *in vivo*. In contrast, *Pdgfrb* is expressed in a subset of *Pdgfra*<sup>+</sup> cells, but also expressed in VECs. *Cdh5* and *Acta2* label vascular cells, which show no overlap with expression of adipogenic genes (i.e. *Plin1*, *Adipoq*, *Car3*).

Neogenesis induced by ADRB3 activation is associated with immune cell recruitment. Analysis of eWAT immune cells identified a cluster of *Gpnmb*<sup>+</sup>*Trem2*<sup>+</sup>*Spp1*<sup>+</sup> macrophages that appear to occupy the adipogenic niche based on expression of genes involved in lipid handling and ECM reorganization. Macrophages have been traditionally classified into M1 (inflammatory) and M2 (non-inflammatory) phenotypes. scRNA-seq, which interrogates hundreds of genes, revealed a diversity of macrophage phenotypes. In light of certain immune markers defined in our iBAT data, a cursory examination of iBAT immune cell markers suggests that a refined classification of eWAT immune cells may be necessary. For example, there are distinct areas of *Irf8*<sup>+</sup> cells, *Cd209a*<sup>+</sup> cells, and *Chil3*<sup>+</sup> cells that in the iBAT data define populations of DEND1 cDC1s, DEND2 moDCs, and MAC3 cold-induced macrophages, respectively. F4/80<sup>+</sup> macrophages that secrete osteopontin (*Spp1*) drive ADRB3-induced adipogenesis through efferocytosis and ASC recruitment [50, 51, 67]. *Adgre1* is highly expressed in the eWAT *Gpnmb*<sup>+</sup> cluster compared to any of the other aforementioned potential immune cell types, so this is likely the phenotype of cells at the site of efferocytosis.

Since the time this WAT single-cell dataset was published, our methods for analysis of scRNA-seq libraries have changed to include additional steps for library cleanup, quality filtering, and different methods of clustering. Processing the WAT scRNA-seq data with that pipeline may further refine SVF subtype heterogeneity, especially among eWAT immune cells.

There are certain limitations to the interpretation of WAT scRNA-seq results. First, in light of the digestion method comparison from mouse iBAT, it is possible that the tissue dissociation and cell isolation procedures required to generate single cells could affect cell type composition or gene expression profiles. Second, our profiling excluded analysis of mature fat cells, whose size and fragility currently present technical challenges for droplet-based single cell analysis. Nonetheless, we note that the overall pattern of gene expression observed in the present experiments is consistent with analysis of bulk tissue RNA, as well as RNA from enriched cell populations isolated by FACS. The development of protocols for analyzing RNA of single nuclei isolated directly from tissue have recently allowed for single nuclei RNA-seq analysis of adipocytes in some depots [174, 175]. Lastly, scRNA-seq provides no information regarding cell location, so it is important to interpret results in the context of concurrent or retrospective histochemical analysis. In this regard, methods like smFISH demonstrated here are powerful tools for cross-validating expression patterns observed in scRNA-seq data.

## **7.2 Deconstructing cold-induced iBAT neogenesis discussion**

Neogenesis is an important adaptive mechanism for expanding the thermogenic capacity of BAT during sustained cold exposure, yet the cellular mechanisms involved are poorly understood. It is well established that cold-induced neogenesis is mediated by

sympathetic nerve activity, can be mimicked by systemic infusions of NE [37, 63], and global knockout of ADRB1 prevents induction of neogenesis by NE infusion *in vivo* [37], supporting the hypothesis that activation of progenitor ADRB1 mediates cold-induced BA neogenesis. However, this simple scenario does not readily account for the observations that neogenesis 1) commences after 2-3 days of cold exposure [37, 55, 64], well after cold activation of classic  $\beta$ -adrenergic/PKA signaling, 2) occurs in specific locations in iBAT [37], and 3) correlates with recruitment of myeloid cells to the tissue.

To address these phenomena, we performed scRNA-seq and fate mapping *in situ* to identify the source of cold-induced BAs among the ASC subtypes present in the tissue. We determined ASC *Adrb1* is not necessary, whereas activation of adipocyte ADRB3 is sufficient to induce BA neogenesis *in vivo*. We confirmed that iBAT neogenesis begins only after 2-3 days of cold exposure, and further determined that the onset and magnitude of neogenesis in individual mice was tightly correlated with specific immune cell recruitment, but not the acute or chronic induction of genes known to be regulated by the  $\beta$ -adrenergic/PKA signaling pathway. Together, these results indicate that cold-induced neogenesis is largely an indirect response to chronic activation of BAs that ultimately serves to increase thermogenic capacity to match thermogenic demand (**Figure 39**). From a physiological perspective, this scenario implies the existence of mechanisms that report metabolic stress, which is detected and transduced into targeted adaptive hyperplasia.

Our scRNA-seq data highlights the diversity of *Pdgfra*<sup>+</sup> stromal cells in BAT and indicate that *Pdgfra* expression most clearly defines ASCs, whereas *Cd34*, *Ly6a*, and *Pdgfrb* are present in additional stromal vascular subtypes. We identified three populations



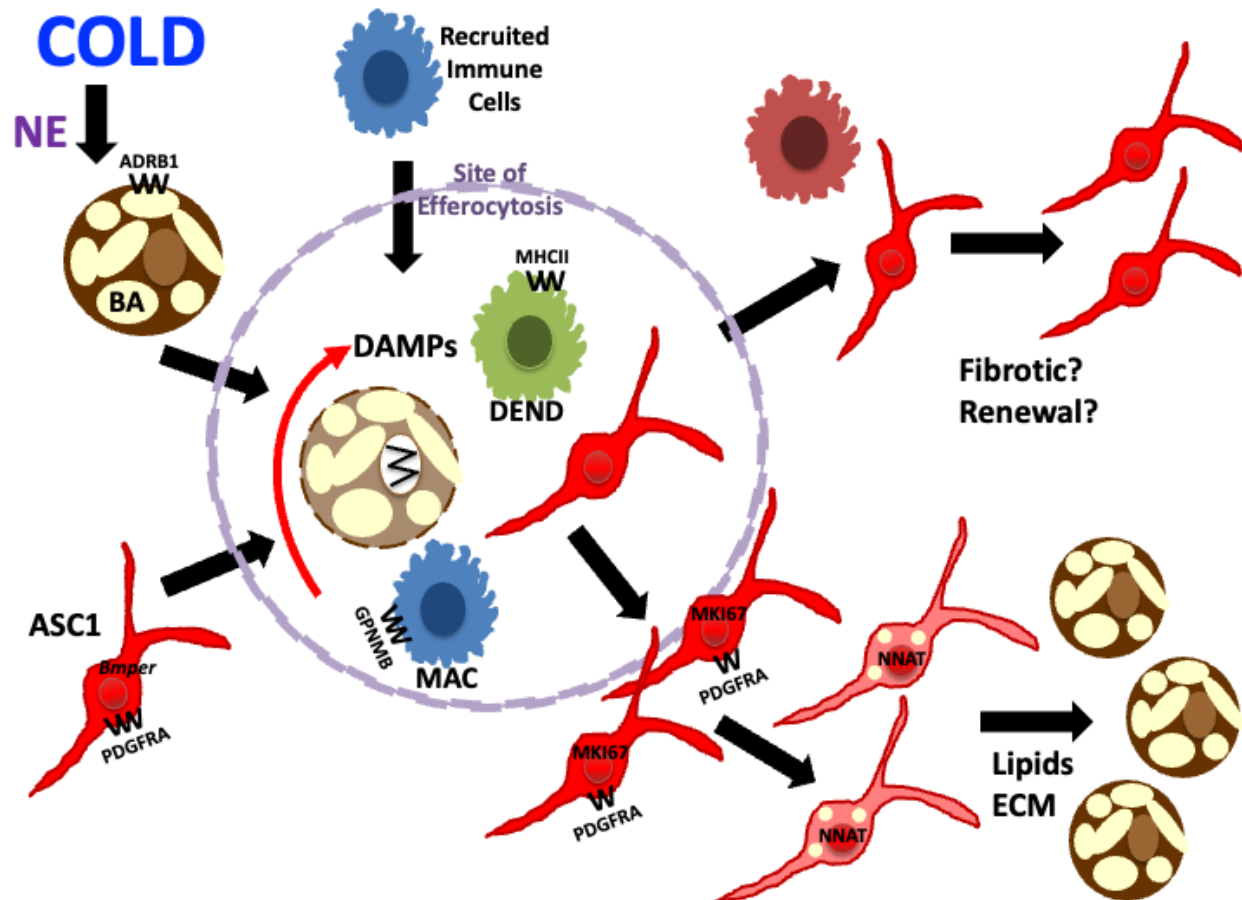


**Figure 39. Model summary of cold-induced iBAT neogenesis.** (Left to right) Cold triggers sympathetic release of norepinephrine (NE) in brown adipose tissue which acts through beta adrenergic receptors (ADRB1) on mature brown adipocytes to initiate brown adipocyte turnover. Brown adipocytes release damage-associated molecular patterns (DAMPs), which are biomolecules that can be recognized by immune cells to trigger a response. These DAMPs could be free fatty acids released from dying adipocytes. Immune cells are recruited to these sites of efferocytosis, including GPNMB+ lipid-handling macrophages (MAC; blue) and MHCII+ dendritic cells (DEND; green). PDGFRA+ *Bmper*+ ASC1 cells in the parenchyma (red) are also recruited to these sites, likely through extracellular matrix remodeling or release of specific ligands. Different local signals from immune cells could control ASC fate, leading to proliferation (MKI67+) and differentiation (NNAT+), proliferation and ASC population renewal, or perhaps moving ASCs to a more fibrotic phenotype.

of ASCs (ASC1, ASC2, ASC3). Importantly, the ASC subtypes can be distinguished by differential expression of genes that are involved in ECM production and signaling by members of the TGF- $\beta$  superfamily. We observed a similar spatial distinction of ASCs to those observed in WAT [137, 140]. Using smFISH, iBAT ASC3 cells surround large vessels, ASC2 cells are present in the fascia that encases the tissue lobes, and ASC1

cells residing in the tissue parenchyma. These distinctions, however, were not absolute, as we observed cells expressing *Pi16* and *Gdf10* on some large vessels, and interstitial ASC1 cells closely associated with capillaries. Together, these data indicate that the ASC subtypes serve distinct functions in the tissue microenvironment. We note in this regard that both ASC1 and ASC2 can be differentiated into adipocytes *in vitro* by conventional chemical inducers (unpublished); thus, *in vitro* differentiation potential should not be used to infer *in vivo* contributions to new fat cell formation.

Eight of our single-cell libraries were prepared from iBAT cells from female mice, while 12 were prepared from iBAT cells from male mice. This gave us the opportunity to compare and query whether there are sex-specific iBAT stromal cell subtypes. Interestingly, we found a small cell cluster (1.4% - 6.4% of cells per library) in the female *Adrb1* KO Lin<sup>-</sup> libraries that we labeled Luminal Cells. This Luminal Cell cluster was distinct from other Lin<sup>-</sup> cell types, was reproduced in every female Lin<sup>-</sup> library, and the top DEGs that defined this cluster were not found in the male libraries. DEGs for this cluster include certain genes (*Krt18*, *Krt19*, *Krt8*, *Krt7*), WAP four-disulfide core domain genes (*Wfdc18*, *Wfdc2*), and epithelial cell adhesion molecule (*Epcam*). This profile is very similar to a mouse mammary luminal cell phenotype, as profiled in the *Tabula Muris* atlas [176]. Although the function of this cell phenotype in BAT is unclear, we note that this cluster selectively expresses the progesterone receptor (*Pgr*), and that the effect of female hormones could be driving this cell phenotype [177].

The identity of the direct precursors of new brown adipocytes remains a highly debated topic [37, 51, 73]. Early fate mapping by Bukoweicki *et al.* strongly indicated that brown adipocytes arise from interstitial cells that are transiently recruited in the first few

days of cold stress [45, 54, 55]. Subsequently, genetic tracing and fate mapping studies established that brown adipocytes arise from an interstitial stromal cell population that expressed PDGFRA in brown adipose tissue (**Figure 39**) [37, 65, 66].

Our scRNA-seq data clearly demonstrate that *Pdgfra*<sup>+</sup> ASC1 cells are the immediate progenitors of cold-induced BAs in adult iBAT (**Figure 39**). Thus, proliferating/differentiating cells expressed ASC1 markers, but not markers of ASC2 or ASC3 markers. In addition, smFISH analysis demonstrated that a high proportion of actively differentiating cells that express *Nnat* co-express the ASC1 marker *Bmper*. Some proliferating ASC1 cells proceeded along an adipogenic trajectory, upregulating markers such as *Car3*, *Adipoq*, and *Plin1*, while some proliferating cells did not. These non-differentiating cells could function to maintain populations of ASC1 cells in iBAT. What determines these different cells fates is not known, but our data suggests that microenvironmental factors, such as proximity to recruited immune cells, could play a role.

Previous FACS analysis of iBAT neogenesis identified a population of F4/80<sup>+</sup> proliferating cells that are recruited after cold stress [37]. Current scRNA-seq data provide new insights into the composition and location of cold-induced immune cell recruitment. Specifically, cold exposure led to the reorganization of immune cell composition of iBAT that included reduction of resident MAC2 cells and striking recruitment of phagocytic macrophage and dendritic cell subtypes.

Macrophage involvement in adipogenesis has been well documented in white adipose depots [50, 67], but remains poorly described in brown adipose tissue. While both macrophage clusters MAC1 and MAC3 were profiled specifically in libraries from cold-

exposed mice, the MAC1 transcriptional profile suggests these cells are involved in the adipogenic process. Top DEGs for MAC1 included genes involved in extracellular matrix remodeling (*Ctsd*, *Ctsb*, *Ctss*), lipid handling (*Fabp5*, *Plin2*, *Lpl*), and chemoattractant activity (*Spp1*). MAC1 cells also expressed high levels of *Gpnmb* and *Trem2*. A similar macrophage gene expression profile was observed in single cell data from mouse white adipose tissue, and, under certain conditions, corresponds to macrophages involved in adipogenesis [97, 148]. *Trem2*<sup>+</sup> macrophages have been well reported in the liver, where they are protective against non-alcoholic fatty liver disease [148, 178-180]. *Trem2* itself has been documented in the brain primarily as a dead cell receptor involved in efferocytosis [181-185]. In gonadal WAT, dying adipocytes recruit macrophages which in turn recruit ASCs for proliferation and differentiation [50, 67]. The presence of *Trem2*<sup>+</sup> macrophages in our iBAT dataset, along with histology, indicate that cold exposure induces localized cellular turnover that involves immune cell recruitment.

Surprisingly, cold exposure also recruited several dendritic cell subtypes, including conventional and monocyte-derived subtypes, and lesser numbers of mature/migratory and plasmacytoid dendritic cells. Moreover, dendritic cells were the primary proliferating immune cell type in the lineage positive cell fraction. Dendritic cells are typically considered antigen presenting cells that modulate adaptive and innate immune responses. However, roles of dendritic cells in non-immune signaling functions have been recognized, such as tissue homeostasis and wound healing [186]. These dendritic cells likely function in a more homeostatic role, as no overt lymphocyte activation was observed. Because monocyte-derived dendritic cells express *Adgre1* (encoding F4/80), we conclude that the proliferating F4/80<sup>+</sup> cells we previously identified by FACS were

primarily monocyte-derived dendritic cells. To confirm this point, immunohistochemical co-staining of mKi67 with either GPNMB or MHCII identified 7X more mKi67+MHCII+ cells than mKi67+GPNMB+ cells (data not shown).

Proliferation and differentiation were highly correlated with the recruitment of monocyte-derived dendritic cells and lipid-handling macrophages, so it was critical to locate these cellular phenotypes in the BAT microenvironment. Histological analysis demonstrated that cold exposure recruited immune cells to specific tissue subdomains that have been previously associated with neogenesis in iBAT [37] and WAT [50, 51]. These included a region near the border of iBAT lobes and along the interface between iBAT and suprascapular WAT [37]. The mechanisms for recruitment to this tissue subdomain are not known, but we note that ASC2, which comprises the fascia, and is the dominant ASC subtype in this region. ASC2 exhibit an immunosurveillance phenotype, and cold exposure upregulated expression of genes involved in response to stress and immune defense (GO:0006950 and GO:0006955, FDR  $p < 10E-10$ ) in these cells. In view of the fact that parenchymal BAs are physically interconnected by gap junctions [187-189], tissue neogenesis might proceed more effectively near tissue borders. Thus, we suggest that ASC2 are well positioned to sense and communicate metabolic stress, and position nascent niches for tissue expansion.

Histological analysis also indicated that chronic cold stress induces parenchymal cell turnover, involving removal of defective BAs and their precise replacement by ASC1 progenitors (**Figure 39**). We found that cold stress led to the appearance of cellular vacancies within the parenchyma that were the size of BAs and often contained the coalesced remnants of lipid droplets that lacked PLIN1, a marker of live adipocytes.

These structures were surrounded by GPNMB+ and MHCII+ macrophage and dendritic cells indicative of ongoing efferocytosis, and proliferating ASC1 cells involved in cell replacement (**Figure 39**). While mechanistic details are yet to be unraveled, our data suggest that lipid-handling MAC1 cells are recruited to distressed BAs. MAC1 express high levels of active mitogens, like *Igf1* and *Pdgfa*, which have cognate receptors on ASC1 cells. In addition, MAC1 express high levels of matrix remodeling proteases that are known to release latent growth factors, like HB-EGF, and modulate the local action of growth factor signaling by inactivating inhibitory growth factor binding proteins [155, 190].

Dendritic cells occupied the same niche with macrophages and proliferating PDGFRA+ cells (**Figure 39**). Whether dendritic cells are recruited in tandem by signals from distressed adipocytes or are recruited to the adipogenic niche by signals from recruited macrophages is presently unclear. Our data suggests that MHCII+ dendritic cells are more heavily recruited to the iBAT periphery, whereas GPNMB+ MAC1 are associated with efferocytosis in the BAT parenchyma. It thus seems likely that the exact composition of adipogenic niches varies among microdomains. Fate mapping and smFISH analysis indicates that differentiation occurs once immune cells depart the adipogenic niche. Sustained mitogenic signaling opposes adipocyte differentiation and thus niche exit could be required for differentiation to proceed [191]. By the same token, we speculate that the failure of some proliferating ASC1 to differentiate might reflect persistent local interactions with resident or recruited immune cells.

In conclusion, our findings highlight the complex cellular changes that occur in BAT in response to cold exposure. This work indicates that cold exposure triggers the formation of adipogenic niches involving close, dynamic interactions between recruited myeloid

cells and interstitial ASC1. Our results demonstrate that neogenesis is not a reflexive response to ADRB1 activation in progenitors, as widely supposed, but rather is a coordinated adaptive response among BAs, immune cells, and progenitors that serves to match metabolic capacity to metabolic demand.

### **7.3 Effect of digestion method on iBAT single-cell analysis discussion**

While this work was in progress, Shamsi, *et al.* published scRNA-seq data of iBAT from cold-exposed mice suggesting that *Trpv1*+ vascular smooth muscle cells (VSMCs) can give rise to BAs [73]. Although *Trpv1*-expressing VSMCs are present in our dataset, these cells were not linked to an adipogenic trajectory. In contrast, we only identified adipogenic differentiation from *Pdgfra*+ ASCs by scRNA-seq and genetic tracing. We believe that key differences in experimental design might have contributed to these differences in results and interpretation. First, our dataset profiled mice at the peak in progenitor proliferation (4 days of cold), while the Shamsi, *et al.* dataset profiled mice after two and seven days of cold exposure in which little neogenesis is observed [37, 73]. Notably, no proliferating cells are present in the Shamsi *et al.* scRNA-seq data. In contrast, we observed robust (~8-21%) proliferation and differentiation of ASC1 in multiple scRNA-seq experiments, and have confirmed this adipogenic trajectory *in situ* by inducible genetic lineage tracing, chemical fate mapping, and smFISH. Second, the datasets contained drastically different proportions of cell types, despite coming from the same tissue. Adipocytes and ASCs make up only an estimated ~13% of the non-immune cells in the Shamsi, *et al.* data (est. ~2,800 cells), compared to ~68.5% of Lin- cells in the present data (19,659 cells). This difference likely involves cell isolation methodology, such as digestion reagents and centrifugation speed.

While there are several potentially important differences, we focused on method of enzymatic digestion. Therefore, we performed a single-cell experiment digesting mouse iBAT with different protease cocktails and digestion methods to see the effect this had on cell isolation. We noted that approximately 2.5X more SVF cells were recovered from iBAT with the Dispase and Collagenase Type 1 method than the Collagenase Type 2 method. Although, this could be the contribution of just the VECs.

Digestion with Dispase and Collagenase Type 1 retained significantly more VECs than digestion with Collagenase Type 2 alone. Collagenase Type 1 exhibits collagenase, caseinase, clostripain, and tryptic activities, while Type 2 contains higher relative levels of these activities, particularly clostripain [192]. Dispase primarily cleaves fibronectin and collagen IV, which are primarily expressed by ASCs and vascular cells [193]. While the two methods isolated similar proportions of other cell types, like ASCs and immune cells, VECs overwhelmed the Dispase/Collagenase Type 1 single-cell libraries (66% of total cells). This can confound single-cell data interpretation if your method is biased toward the isolation of one cell type and at the expense of profiling others. It is unlikely that either method is capturing the true proportions of all the cell types in the tissue, which is why it is critical to validate key findings in the intact tissue. The effect of digestion method should be an important consideration when using scRNA-seq.

The differences in cell recovery beg the question: which digestion method should be used to study mouse iBAT? Dispase and Collagenase Type 1 yielded more cells, but the VECs overwhelmed the scRNA-seq data and were not shown to contribute to cold-induced BAT neogenesis. Collagenase Type 2 isolated a large population of ASCs, along with cold-induced immune cells, which allowed us to draw major conclusions about the



neogenic process. However, the cell yield is low based on what we would expect for the given volume of tissue. To study proliferation and differentiation of ASCs *in vivo*, the current Collagenase Type 2 method will allow for good capture and profiling of these cells, but digestion methods should be improved to increase cell yield of all cell types from mouse iBAT at numbers closer to their true proportions.

In view of potential differences in the efficiency and recovery of isolated stromal cells, it was important to establish the cold-induced adipogenic trajectory *in situ* using highly sensitive smFISH. High resolution confocal microscopy of informative mRNA markers established the presence of cold-induced adipogenic niches containing the range of adipogenic states of ASC1 from quiescence to active proliferation, and from early to late differentiation. Spatial mapping of this trajectory indicates that adipogenic niches involve close (micron scale) cellular communication in tissue volumes less than 0.0001 cubic millimeter, consistent with the estimated distance of cytokine signaling *in situ* [194].

#### **7.4 Manipulation of iBAT immune cells *in vivo* discussion**

Cold triggers the appearance of multiple immune cell types in iBAT, including populations of lipid-handling macrophages (MAC1) and dendritic cells (DEND1-4). Our goal was to manipulate immune cell populations *in vivo* and observe the effect on cell proliferation. CCR2 has been extensively studied as a mediator of immune cell infiltration into a myriad of tissues, including white adipose tissue; although, it is typically studied in the context of obesity and inflammation. *Ccr2* is expressed in macrophages and dendritic cells in our iBAT single-cell data. *Ccr2* knockout did not affect immune cell recruitment or proliferation, suggesting that CCR2 is not the dominant mechanism for new monocyte recruitment. Our data indicate that neogenesis is associated with BA cell stress that is

likely mediated by release of Damage Associated Molecule Patterns (DAMPs) which could be the signal for recruitment.

ITGAM-DTR mice demonstrated a lack of DTR expression, and we were unable to achieve CD11b<sup>+</sup> cell depletion with this model. Studies controlled for potency of DT and compared separate cohorts of mice, but we observed no reduction in CD11b<sup>+</sup> cells as measured by flow cytometry. Additionally, we reached out to Jackson Labs who responded that the phenotype of the strain may be variable, depending on the route of DT administration, DT dose, target tissue, and possible environmental considerations. Based on our single-cell data, we expected the *Itgam* promoter to target all subpopulations of macrophages, moDCs, and monocytes. However, a different promoter such as *Itgax* or *Zbtb46* would target all dendritic cell subtypes (DEND1-4). This DTR system has many considerations when planning experiments, especially the timing of DT injection as DT will knockdown cells for a limited window of time, followed an increase in the ablated cell types. Additionally, DT is extremely toxic and potentially lethal if DT treatment is prolonged.

As an alternative approach, we used clodronate-containing liposomes, which selectively target and deplete phagocytic monocytes/macrophages *in vivo*. We found that intraperitoneal injection of clodronate-containing liposomes reduced mouse weight in control mice housed at room temperature. This clodronate liposomes-induced weight loss, coupled with cold stress, proved intolerable for some mice in the cohort, causing us to change our method to a tissue-targeted approach. Unexpectedly, we found that liposome direct injection alone was sufficient to recruit immune cells and induce proliferation which confounded the interpretation of our results. qPCR indicates that

clodronate recruits Gpnmb<sup>+</sup> and Irf8<sup>+</sup> cells in the absence of cold. We note that liposomes are essentially foreign bodies whose phospholipid and cholesterol composition likely serve as potent DAMPs for immune recruitment. Cholesterol crystals and oxidized phosphatidylcholine are recognized DAMPs [195-197]. Indeed, histological analysis demonstrated that dense infiltration of GPNMB<sup>+</sup> and MHCII<sup>+</sup> immune cells, and PDGFRA<sup>+</sup> cells, that appeared to encapsulate injected liposomes. These sites included proliferating GPNMB<sup>+</sup> macrophages. While the recruited immune cells did express the immune cell markers GPNMB and MHCII, whether these cells are the same as what we profiled before is undetermined. PI16<sup>+</sup> surround the foreign body reaction, consistent with the immunosurveillance phenotype of these cells. We also noted PLIN<sup>+</sup> cells in the area of the foreign body reaction. However, whether these injections are sufficient to induce local adipogenesis, potentially from ASC2 PI16<sup>+</sup> cells, requires further study.

## Chapter 8. Future Directions

The current work demonstrates that there is a dynamic spatial organization of BA neogenesis. Furthermore, preliminary data suggest that adipogenic niches occupy a volume of less than  $0.001 \text{ mm}^3$ . Thus, dissection will require techniques that locate and classify cells at a micrometer scale. Studies should continue to refine smFISH probes and antibodies to localize specific cell subtypes in the tissue. For example, can we distinguish between cDC1s and moDCs? Localizing these cells may help elucidate their function. Additionally, examining tissue at different cold exposure time points could resolve the order that immune cell types are recruited.

While smFISH and immunohistochemistry were able to support our conclusions from scRNA-seq, these techniques still rely on a limited set of markers and have not completely resolved the spatial relationships between all iBAT cell types. Alternatively, techniques are now available to perform spatial transcriptomics that allow for transcriptomic profiling of single cells while also maintaining the spatial architecture of the tissue [198-200]. It is clear that local interactions between ASCs and immune cells are driving adipogenic differentiation. Deconstructing what cells are in close proximity will provide evidence for how cells are communicating. These data will also allow for the use of computational programs to analyze cell neighborhoods and predict cell signaling [201, 202], which is a much more unbiased approach than the manual method used here.

This work did not evaluate the contribution of the mature adipocytes, which can now be profiled with single-nuclei RNA-seq. Profiling mature adipocytes as they undergo cold-induced cell turnover could demonstrate gene expression changes that indicate why the cell is targeted for turnover, and give insight into signals released by dying cells.

The future directions of this project should also be focused on the causal relationship between immune cell recruitment and ASC proliferation/differentiation in mouse iBAT. While the immune manipulation methods detailed here were unsuccessful in furthering our understanding of iBAT neogenesis, these techniques could be modified. For example, while the ITGAM-DTR mouse model did not deplete CD11b+ cells *in vivo*, DTR models driven by other promoters may work for cell knockdown and be more specific to immune cell subtypes. According to our single-cell data, ITGAX-DTR mice (CD11c) would exclusively target dendritic cells. As for the clodronate liposome experiments, i.p. injection of liposomes coupled with CL-infusion instead of cold exposure may prove more tolerable for mice, as we now know that CL treatment is sufficient to trigger BAT neogenesis.

Another outstanding question is whether the immune cells profiled with scRNA-seq are recruited or resident populations that increase with proliferation. scRNA-seq and immunohistochemistry established that there is an MHCII+ population of macrophages in room temperature BAT that isn't present in scRNA-seq data from cold mice. Instead, cold mice have an abundance of MHCII+ dendritic cells. Are the resident room temperature MHCII+ macrophages changing their phenotype to a cold-induced macrophage profile? We hypothesized that GPNMB+ macrophages are recruited by DAMPs released by dying adipocyte and could be recruited. We observed that specific immune cell types occupy distinct areas of the tissue, with MHCII+ dendritic cells more heavily recruited to the iBAT periphery while GPNMB+ MAC1 are associated with efferocytosis in the BAT parenchyma. This suggests different signals to recruit these cell types to different areas. While little dendritic cells are observed in the room temperature scRNA-seq iBAT data,

we know that cells types are proliferative. Could the numbers of resident cells increase with proliferation or were they recruited and then proliferate?

These results change the focus of iBAT neogenesis to center key immune cells subpopulations, along with ASCs, as potential therapeutic targets for expansion of BA populations *in vivo*.

## REFERENCES

1. Bullard, K.M., et al., *Prevalence of Diagnosed Diabetes in Adults by Diabetes Type - United States, 2016*. MMWR Morb Mortal Wkly Rep, 2018. **67**(12): p. 359-361.
2. Prevention, C.f.D.C.a., *National Diabetes Statistics Report 2020*. . 2020.
3. Sun, K., C.M. Kusminski, and P.E. Scherer, *Adipose tissue remodeling and obesity*. J Clin Invest, 2011. **121**(6): p. 2094-101.
4. Cohen, P. and B.M. Spiegelman, *Brown and Beige Fat: Molecular Parts of a Thermogenic Machine*. Diabetes, 2015. **64**(7): p. 2346-51.
5. Spiegelman, B.M., *Banting Lecture 2012: Regulation of adipogenesis: toward new therapeutics for metabolic disease*. Diabetes, 2013. **62**(6): p. 1774-82.
6. Wu, J., P. Cohen, and B.M. Spiegelman, *Adaptive thermogenesis in adipocytes: is beige the new brown?* Genes Dev, 2013. **27**(3): p. 234-50.
7. Cinti, S., *The adipose organ: morphological perspectives of adipose tissues*. Proceedings of the Nutrition Society, 2001. **60**(3): p. 319-328.
8. Unger, R.H., *Lipotoxic diseases*. Annual review of medicine, 2002. **53**(1): p. 319-336.
9. Unger, R.H. and P.E. Scherer, *Gluttony, sloth and the metabolic syndrome: a roadmap to lipotoxicity*. Trends in Endocrinology & Metabolism, 2010. **21**(6): p. 345-352.
10. de Souza, C.J., et al., *Effects of pioglitazone on adipose tissue remodeling within the setting of obesity and insulin resistance*. Diabetes, 2001. **50**(8): p. 1863-71.

11. Okuno, A., et al., *Troglitazone increases the number of small adipocytes without the change of white adipose tissue mass in obese Zucker rats*. J Clin Invest, 1998. **101**(6): p. 1354-61.
12. Staels, B. and J.C. Fruchart, *Therapeutic roles of peroxisome proliferator-activated receptor agonists*. Diabetes, 2005. **54**(8): p. 2460-70.
13. Tang, W., et al., *Thiazolidinediones regulate adipose lineage dynamics*. Cell Metab, 2011. **14**(1): p. 116-22.
14. Cinti, S., *Transdifferentiation properties of adipocytes in the adipose organ*. Am J Physiol Endocrinol Metab, 2009. **297**(5): p. E977-86.
15. Ghorbani, M. and J. Himms-Hagen, *Appearance of brown adipocytes in white adipose tissue during CL 316,243-induced reversal of obesity and diabetes in Zucker fa/fa rats*. Int J Obes Relat Metab Disord, 1997. **21**(6): p. 465-75.
16. Granneman, J.G., et al., *Metabolic and cellular plasticity in white adipose tissue I: effects of beta3-adrenergic receptor activation*. Am J Physiol Endocrinol Metab, 2005. **289**(4): p. E608-16.
17. Cummings, D.E., et al., *Genetically lean mice result from targeted disruption of the RII beta subunit of protein kinase A*. Nature, 1996. **382**(6592): p. 622-6.
18. Soloveva, V., et al., *Transgenic mice overexpressing the beta 1-adrenergic receptor in adipose tissue are resistant to obesity*. Mol Endocrinol, 1997. **11**(1): p. 27-38.
19. Chondronikola, M., et al., *Brown Adipose Tissue Activation Is Linked to Distinct Systemic Effects on Lipid Metabolism in Humans*. Cell Metab, 2016. **23**(6): p. 1200-1206.



20. Granneman, J.G., *Renaissance of brown adipose tissue research: integrating the old and new*. Int J Obes Suppl, 2015. **5**(Suppl 1): p. S7-s10.
21. Kajimura, S., *Engineering Fat Cell Fate to Fight Obesity and Metabolic Diseases*. Keio J Med, 2015. **64**(4): p. 65.
22. Kajimura, S., B.M. Spiegelman, and P. Seale, *Brown and Beige Fat: Physiological Roles beyond Heat Generation*. Cell Metab, 2015. **22**(4): p. 546-59.
23. Sanchez-Gurmaches, J. and D.A. Guertin, *Adipocyte lineages: tracing back the origins of fat*. Biochim Biophys Acta, 2014. **1842**(3): p. 340-51.
24. Fox, C.S., et al., *Abdominal visceral and subcutaneous adipose tissue compartments: association with metabolic risk factors in the Framingham Heart Study*. Circulation, 2007. **116**(1): p. 39-48.
25. Gastaldelli, A., et al., *Metabolic effects of visceral fat accumulation in type 2 diabetes*. J Clin Endocrinol Metab, 2002. **87**(11): p. 5098-103.
26. Kissebah, A.H., et al., *Relation of body fat distribution to metabolic complications of obesity*. J Clin Endocrinol Metab, 1982. **54**(2): p. 254-60.
27. Luong, Q., J. Huang, and K.Y. Lee, *Deciphering White Adipose Tissue Heterogeneity*. Biology (Basel), 2019. **8**(2).
28. Zhang, M., et al., *Associations of Different Adipose Tissue Depots with Insulin Resistance: A Systematic Review and Meta-analysis of Observational Studies*. Sci Rep, 2015. **5**: p. 18495.
29. Abdullahi, A. and M.G. Jeschke, *White Adipose Tissue Browning: A Double-edged Sword*. Trends Endocrinol Metab, 2016. **27**(8): p. 542-552.

30. Lee, Y.H., E.P. Mottillo, and J.G. Granneman, *Adipose tissue plasticity from WAT to BAT and in between*. *Biochim Biophys Acta*, 2014. **1842**(3): p. 358-69.
31. Park, A., W.K. Kim, and K.H. Bae, *Distinction of white, beige and brown adipocytes derived from mesenchymal stem cells*. *World J Stem Cells*, 2014. **6**(1): p. 33-42.
32. Smorlesi, A., et al., *The adipose organ: white-brown adipocyte plasticity and metabolic inflammation*. *Obes Rev*, 2012. **13 Suppl 2**: p. 83-96.
33. Foster, D.O. and M.L. Frydman, *Brown adipose tissue: the dominant site of nonshivering thermogenesis in the rat*. *Experientia Suppl*, 1978. **32**: p. 147-51.
34. Dawkins, M.J. and D. Hull, *BROWN ADIPOSE TISSUE AND NON-SHIVERING THERMOGENESIS IN NEWBORN ANIMALS*. *Maandschr Kindergeneeskd*, 1964. **32**: p. 641-52.
35. Bartness, T.J., C.H. Vaughan, and C.K. Song, *Sympathetic and sensory innervation of brown adipose tissue*. *International Journal of Obesity*, 2010. **34**(1): p. S36-S42.
36. François, M., et al., *Sympathetic innervation of the interscapular brown adipose tissue in mouse*. *Ann N Y Acad Sci*, 2019. **1454**(1): p. 3-13.
37. Lee, Y.H., et al., *Cellular origins of cold-induced brown adipocytes in adult mice*. *Faseb j*, 2015. **29**(1): p. 286-99.
38. Cannon, B. and J. Nedergaard, *Brown adipose tissue: function and physiological significance*. *Physiol Rev*, 2004. **84**(1): p. 277-359.
39. Lowell, B.B. and B.M. Spiegelman, *Towards a molecular understanding of adaptive thermogenesis*. *Nature*, 2000. **404**(6778): p. 652-660.

40. Muzik, O., T.J. Mangner, and J.G. Granneman, *Assessment of oxidative metabolism in brown fat using PET imaging*. Front Endocrinol (Lausanne), 2012. **3**: p. 15.
41. Muzik, O., et al., *150 PET measurement of blood flow and oxygen consumption in cold-activated human brown fat*. J Nucl Med, 2013. **54**(4): p. 523-31.
42. Becher, T., et al., *Brown adipose tissue is associated with cardiometabolic health*. Nat Med, 2021. **27**(1): p. 58-65.
43. Herz, C.T., et al., *Active Brown Adipose Tissue is Associated With a Healthier Metabolic Phenotype in Obesity*. Diabetes, 2021.
44. Wibmer, A.G., et al., *Brown adipose tissue is associated with healthier body fat distribution and metabolic benefits independent of regional adiposity*. Cell Rep Med, 2021. **2**(7): p. 100332.
45. Géloën, A., et al., *Beta-adrenergic stimulation of brown adipocyte proliferation*. Am J Physiol, 1988. **254**(1 Pt 1): p. C175-82.
46. Hanssen, M.J., et al., *Serum FGF21 levels are associated with brown adipose tissue activity in humans*. Sci Rep, 2015. **5**: p. 10275.
47. Villarroya, F., et al., *Brown adipose tissue as a secretory organ*. Nat Rev Endocrinol, 2017. **13**(1): p. 26-35.
48. Villarroya, J., et al., *New insights into the secretory functions of brown adipose tissue*. J Endocrinol, 2019. **243**(2): p. R19-r27.
49. Barbatelli, G., et al., *The emergence of cold-induced brown adipocytes in mouse white fat depots is determined predominantly by white to brown adipocyte transdifferentiation*. Am J Physiol Endocrinol Metab, 2010. **298**(6): p. E1244-53.

50. Lee, Y.H., A.P. Petkova, and J.G. Granneman, *Identification of an adipogenic niche for adipose tissue remodeling and restoration*. Cell Metab, 2013. **18**(3): p. 355-67.
51. Lee, Y.H., et al., *In vivo identification of bipotential adipocyte progenitors recruited by  $\beta$ 3-adrenoceptor activation and high-fat feeding*. Cell Metab, 2012. **15**(4): p. 480-91.
52. Rosenwald, M., et al., *Bi-directional interconversion of brite and white adipocytes*. Nat Cell Biol, 2013. **15**(6): p. 659-67.
53. Wang, Q.A., et al., *Tracking adipogenesis during white adipose tissue development, expansion and regeneration*. Nat Med, 2013. **19**(10): p. 1338-44.
54. Bukowiecki, L., et al., *Brown adipose tissue hyperplasia: a fundamental mechanism of adaptation to cold and hyperphagia*. Am J Physiol, 1982. **242**(6): p. E353-9.
55. Bukowiecki, L.J., A. G elo en, and A.J. Collet, *Proliferation and differentiation of brown adipocytes from interstitial cells during cold acclimation*. Am J Physiol, 1986. **250**(6 Pt 1): p. C880-7.
56. Nedergaard, J., *Catecholamine sensitivity in brown fat cells from cold-acclimated hamsters and rats*. Am J Physiol, 1982. **242**(3): p. C250-7.
57. Kotzbeck, P., et al., *Brown adipose tissue whitening leads to brown adipocyte death and adipose tissue inflammation*. J Lipid Res, 2018. **59**(5): p. 784-794.
58. Chawla, A., et al., *Peroxisome proliferator-activated receptor (PPAR) gamma: adipose-predominant expression and induction early in adipocyte differentiation*. Endocrinology, 1994. **135**(2): p. 798-800.

59. Farmer, S.R., *Transcriptional control of adipocyte formation*. Cell Metab, 2006. **4**(4): p. 263-73.
60. Green, H. and O. Kehinde, *An established preadipose cell line and its differentiation in culture. II. Factors affecting the adipose conversion*. Cell, 1975. **5**(1): p. 19-27.
61. Wang, N.D., et al., *Impaired energy homeostasis in C/EBP alpha knockout mice*. Science, 1995. **269**(5227): p. 1108-12.
62. Himms-Hagen, J., et al., *Multilocular fat cells in WAT of CL-316243-treated rats derive directly from white adipocytes*. American Journal of Physiology-Cell Physiology, 2000. **279**(3): p. C670-C681.
63. Gélöën, A., A.J. Collet, and L.J. Bukowiecki, *Role of sympathetic innervation in brown adipocyte proliferation*. Am J Physiol, 1992. **263**(6 Pt 2): p. R1176-81.
64. Hunt, T.E. and E.A. Hunt, *A radioautographic study of proliferation in brown fat of the rat after exposure to cold*. Anatomical Record, 1967. **157**: p. 537-546.
65. Cattaneo, P., et al., *Parallel Lineage-Tracing Studies Establish Fibroblasts as the Prevailing In Vivo Adipocyte Progenitor*. Cell Rep, 2020. **30**(2): p. 571-582.e2.
66. Sun, C., et al., *Mosaic Mutant Analysis Identifies PDGFR $\alpha$ /PDGFR $\beta$  as Negative Regulators of Adipogenesis*. Cell Stem Cell, 2020. **26**(5): p. 707-721.e5.
67. Lee, Y.H., et al., *Adipogenic role of alternatively activated macrophages in  $\beta$ -adrenergic remodeling of white adipose tissue*. Am J Physiol Regul Integr Comp Physiol, 2016. **310**(1): p. R55-65.

68. Berry, D.C., Y. Jiang, and J.M. Graff, *Mouse strains to study cold-inducible beige progenitors and beige adipocyte formation and function*. Nature communications, 2016. **7**(1): p. 1-17.
69. Tran, K.-V., et al., *The vascular endothelium of the adipose tissue gives rise to both white and brown fat cells*. Cell metabolism, 2012. **15**(2): p. 222-229.
70. Vishvanath, L., et al., *Pdgfr $\beta$ + mural preadipocytes contribute to adipocyte hyperplasia induced by high-fat-diet feeding and prolonged cold exposure in adult mice*. Cell metabolism, 2016. **23**(2): p. 350-359.
71. Jiang, Y., et al., *Independent Stem Cell Lineages Regulate Adipose Organogenesis and Adipose Homeostasis*. Cell Reports, 2014. **9**(3): p. 1007-1022.
72. Long, Jonathan Z., et al., *A Smooth Muscle-Like Origin for Beige Adipocytes*. Cell Metabolism, 2014. **19**(5): p. 810-820.
73. Shamsi, F., et al., *Vascular smooth muscle-derived Trpv1(+) progenitors are a source of cold-induced thermogenic adipocytes*. Nat Metab, 2021. **3**(4): p. 485-495.
74. Collins, S.,  *$\beta$ -Adrenergic Receptors and Adipose Tissue Metabolism: Evolution of an Old Story*. Annu Rev Physiol, 2022. **84**: p. 1-16.
75. Collins, S. and R.S. Surwit, *The beta-adrenergic receptors and the control of adipose tissue metabolism and thermogenesis*. Recent Prog Horm Res, 2001. **56**: p. 309-28.
76. Bronnikov, G., J. Houstěk, and J. Nedergaard, *Beta-adrenergic, cAMP-mediated stimulation of proliferation of brown fat cells in primary culture. Mediation via beta 1 but not via beta 3 adrenoceptors*. J Biol Chem, 1992. **267**(3): p. 2006-13.

77. Himms-Hagen, J., J. Cui, and S. Lynn Sigurdson, *Sympathetic and sensory nerves in control of growth of brown adipose tissue: Effects of denervation and of capsaicin*. *Neurochemistry International*, 1990. **17**(2): p. 271-279.
78. Bronnikov, G., et al., *beta1 to beta3 switch in control of cyclic adenosine monophosphate during brown adipocyte development explains distinct beta-adrenoceptor subtype mediation of proliferation and differentiation*. *Endocrinology*, 1999. **140**(9): p. 4185-97.
79. Chawla, A., K.D. Nguyen, and Y. Goh, *Macrophage-mediated inflammation in metabolic disease*. *Nature Reviews Immunology*, 2011. **11**(11): p. 738-749.
80. Weisberg, S.P., et al., *Obesity is associated with macrophage accumulation in adipose tissue*. *J Clin Invest*, 2003. **112**(12): p. 1796-808.
81. Xu, H., et al., *Chronic inflammation in fat plays a crucial role in the development of obesity-related insulin resistance*. *J Clin Invest*, 2003. **112**(12): p. 1821-30.
82. Biswas, Subhra K. and A. Mantovani, *Orchestration of Metabolism by Macrophages*. *Cell Metabolism*, 2012. **15**(4): p. 432-437.
83. Ganz, T., *Macrophages and Iron Metabolism*. *Microbiol Spectr*, 2016. **4**(5).
84. Mosser, D.M., K. Hamidzadeh, and R. Goncalves, *Macrophages and the maintenance of homeostasis*. *Cellular & Molecular Immunology*, 2021. **18**(3): p. 579-587.
85. Wynn, T.A. and K.M. Vannella, *Macrophages in Tissue Repair, Regeneration, and Fibrosis*. *Immunity*, 2016. **44**(3): p. 450-462.

86. Guilliams, M. and L. van de Laar, *A Hitchhiker's Guide to Myeloid Cell Subsets: Practical Implementation of a Novel Mononuclear Phagocyte Classification System*. Front Immunol, 2015. **6**: p. 406.
87. Mani, B.K., et al.,  *$\beta$ 1-Adrenergic receptor deficiency in ghrelin-expressing cells causes hypoglycemia in susceptible individuals*. J Clin Invest, 2016. **126**(9): p. 3467-78.
88. Kishi, J.Y., et al., *SABER amplifies FISH: enhanced multiplexed imaging of RNA and DNA in cells and tissues*. Nat Methods, 2019. **16**(6): p. 533-544.
89. Ray, A. and B.N. Dittel, *Isolation of mouse peritoneal cavity cells*. J Vis Exp, 2010(35).
90. Duffield, J.S., et al., *Selective depletion of macrophages reveals distinct, opposing roles during liver injury and repair*. J Clin Invest, 2005. **115**(1): p. 56-65.
91. Sayers, E.W., et al., *Database resources of the national center for biotechnology information*. Nucleic Acids Res, 2022. **50**(D1): p. D20-d26.
92. Li, Y. and J. Andrade, *DEApp: an interactive web interface for differential expression analysis of next generation sequence data*. Source Code Biol Med, 2017. **12**: p. 2.
93. Babicki, S., et al., *Heatmapper: web-enabled heat mapping for all*. Nucleic Acids Res, 2016. **44**(W1): p. W147-53.
94. Dobin, A., et al., *STAR: ultrafast universal RNA-seq aligner*. Bioinformatics, 2013. **29**(1): p. 15-21.
95. Anders, S., P.T. Pyl, and W. Huber, *HTSeq--a Python framework to work with high-throughput sequencing data*. Bioinformatics, 2015. **31**(2): p. 166-9.



96. Ge, S.X., E.W. Son, and R. Yao, *iDEP: an integrated web application for differential expression and pathway analysis of RNA-Seq data*. BMC Bioinformatics, 2018. **19**(1): p. 534.
97. Burl, R.B., et al., *Deconstructing Adipogenesis Induced by  $\beta$ 3-Adrenergic Receptor Activation with Single-Cell Expression Profiling*. Cell Metab, 2018. **28**(2): p. 300-309.e4.
98. Young, M.D. and S. Behjati, *SoupX removes ambient RNA contamination from droplet-based single-cell RNA sequencing data*. Gigascience, 2020. **9**(12).
99. Stuart, T., et al., *Comprehensive Integration of Single-Cell Data*. Cell, 2019. **177**(7): p. 1888-1902 e21.
100. *The Gene Ontology resource: enriching a GOLD mine*. Nucleic Acids Res, 2021. **49**(D1): p. D325-d334.
101. Ashburner, M., et al., *Gene ontology: tool for the unification of biology. The Gene Ontology Consortium*. Nat Genet, 2000. **25**(1): p. 25-9.
102. Efremova, M., et al., *CellPhoneDB: inferring cell-cell communication from combined expression of multi-subunit ligand-receptor complexes*. Nat Protoc, 2020. **15**(4): p. 1484-1506.
103. Browaeys, R., W. Saelens, and Y. Saeys, *NicheNet: modeling intercellular communication by linking ligands to target genes*. Nature Methods, 2020. **17**(2): p. 159-162.
104. Skelly, D.A., et al., *Single-Cell Transcriptional Profiling Reveals Cellular Diversity and Intercommunication in the Mouse Heart*. Cell Rep, 2018. **22**(3): p. 600-610.

105. *R: A Language and Environment for Statistical Computing.*, R.C. Team, Editor. 2020, R Foundation for Statistical Computing: Vienna, Austria.
106. *RStudio: Integrated Development Environment for R.*, R. Team, Editor. 2022, RStudio, PBC: Boston, MA.
107. Stangroom, J. *Chi-Square Test Calculator*. [cited 2022; Available from: <https://www.socscistatistics.com/tests/chisquare2/default2.aspx>].
108. Lee, Y.H., et al., *Adipogenic role of alternatively activated macrophages in beta-adrenergic remodeling of white adipose tissue*. *Am J Physiol Regul Integr Comp Physiol*, 2016. **310**(1): p. R55-65.
109. Lee, Y.H., et al., *Exploring the activated adipogenic niche: interactions of macrophages and adipocyte progenitors*. *Cell Cycle*, 2014. **13**(2): p. 184-90.
110. Lee, Y.H., et al., *In vivo identification of bipotential adipocyte progenitors recruited by beta3-adrenoceptor activation and high-fat feeding*. *Cell Metab*, 2012. **15**(4): p. 480-91.
111. Satija, R., et al., *Spatial reconstruction of single-cell gene expression*. *Nature biotechnology*, 2015. **33**(5): p. 495-502.
112. Marcelin, G., et al., *A PDGFRalpha-Mediated Switch toward CD9high Adipocyte Progenitors Controls Obesity-Induced Adipose Tissue Fibrosis*. *Cell Metab*, 2017. **25**(3): p. 673-685.
113. Sun, C., W.L. Berry, and L.E. Olson, *PDGFRalpha controls the balance of stromal and adipogenic cells during adipose tissue organogenesis*. *Development*, 2017. **144**(1): p. 83-94.

114. Li, Q., et al., *The role of SDF-1-CXCR4/CXCR7 axis in biological behaviors of adipose tissue-derived mesenchymal stem cells in vitro*. *Biochem Biophys Res Commun*, 2013. **441**(3): p. 675-80.
115. Sengenès, C., et al., *Chemotaxis and differentiation of human adipose tissue CD34+/CD31- progenitor cells: role of stromal derived factor-1 released by adipose tissue capillary endothelial cells*. *Stem Cells*, 2007. **25**(9): p. 2269-76.
116. Tseng, Y.H., et al., *Differential roles of insulin receptor substrates in the anti-apoptotic function of insulin-like growth factor-1 and insulin*. *J Biol Chem*, 2002. **277**(35): p. 31601-11.
117. Kawaguchi, N., et al., *ADAM 12 protease induces adipogenesis in transgenic mice*. *Am J Pathol*, 2002. **160**(5): p. 1895-903.
118. Lagathu, C., et al., *Secreted frizzled-related protein 1 regulates adipose tissue expansion and is dysregulated in severe obesity*. *Int J Obes (Lond)*, 2010. **34**(12): p. 1695-705.
119. Lagathu, C., et al., *Dact1, a nutritionally regulated preadipocyte gene, controls adipogenesis by coordinating the Wnt/beta-catenin signaling network*. *Diabetes*, 2009. **58**(3): p. 609-19.
120. Sato-Kusubata, K., et al., *Adipogenic histone mark regulation by matrix metalloproteinase 14 in collagen-rich microenvironments*. *Mol Endocrinol*, 2011. **25**(5): p. 745-53.
121. Chun, T.H., et al., *A pericellular collagenase directs the 3-dimensional development of white adipose tissue*. *Cell*, 2006. **125**(3): p. 577-91.

122. Vishvanath, L., et al., *Pdgfrbeta+ Mural Preadipocytes Contribute to Adipocyte Hyperplasia Induced by High-Fat-Diet Feeding and Prolonged Cold Exposure in Adult Mice*. Cell Metab, 2016. **23**(2): p. 350-9.
123. Berry, D.C., Y. Jiang, and J.M. Graff, *Mouse strains to study cold-inducible beige progenitors and beige adipocyte formation and function*. Nat Commun, 2016. **7**: p. 10184.
124. Tran, K.V., et al., *The vascular endothelium of the adipose tissue gives rise to both white and brown fat cells*. Cell Metab, 2012. **15**(2): p. 222-9.
125. Cinti, S., et al., *An ultrastructural study of adipocyte precursors from epididymal fat pads of adult rats in culture*. J Submicrosc Cytol, 1985. **17**(4): p. 631-6.
126. Hong, K.Y., et al., *Perilipin+ embryonic preadipocytes actively proliferate along growing vasculatures for adipose expansion*. Development, 2015. **142**(15): p. 2623-32.
127. Lee, Y.H., et al., *Metabolic heterogeneity of activated beige/brite adipocytes in inguinal adipose tissue*. Sci Rep, 2017. **7**: p. 39794.
128. Xue, J., et al., *Transcriptome-based network analysis reveals a spectrum model of human macrophage activation*. Immunity, 2014. **40**(2): p. 274-88.
129. Aouadi, M., et al., *Lipid storage by adipose tissue macrophages regulates systemic glucose tolerance*. Am J Physiol Endocrinol Metab, 2014. **307**(4): p. E374-83.
130. Amano, S.U., et al., *Local proliferation of macrophages contributes to obesity-associated adipose tissue inflammation*. Cell Metab, 2014. **19**(1): p. 162-171.

131. Grijalva, A., X. Xu, and A.W. Ferrante, Jr., *Autophagy Is Dispensable for Macrophage-Mediated Lipid Homeostasis in Adipose Tissue*. *Diabetes*, 2016. **65**(4): p. 967-80.
132. Chang, H.R., et al., *Macrophage and adipocyte IGF1 maintain adipose tissue homeostasis during metabolic stresses*. *Obesity (Silver Spring)*, 2016. **24**(1): p. 172-83.
133. Cinti, S., *Transdifferentiation properties of adipocytes in the adipose organ*. *Am. J. Physiol. Endocrinol. Metab.*, 2009. **297**: p. E977-E986.
134. Himms-Hagen, J., et al., *Multilocular fat cells in WAT of CL-316243-treated rats derive directly from white adipocytes*. *Am J Physiol Cell Physiol*, 2000. **279**(3): p. C670-81.
135. Tang, W., et al., *White fat progenitor cells reside in the adipose vasculature*. *Science*, 2008. **322**(5901): p. 583-6.
136. Hepler, C., et al., *Identification of functionally distinct fibro-inflammatory and adipogenic stromal subpopulations in visceral adipose tissue of adult mice*. *Elife*, 2018. **7**.
137. Merrick, D., et al., *Identification of a mesenchymal progenitor cell hierarchy in adipose tissue*. *Science*, 2019. **364**(6438).
138. Schwalie, P.C., et al., *A stromal cell population that inhibits adipogenesis in mammalian fat depots*. *Nature*, 2018. **559**(7712): p. 103-108.
139. Dong, H., et al., *Identification of a regulatory pathway inhibiting adipogenesis via RSPO2*. *Nature Metabolism*, 2022. **4**(1): p. 90-105.

140. Rondini, E.A. and J.G. Granneman, *Single cell approaches to address adipose tissue stromal cell heterogeneity*. *Biochem J*, 2020. **477**(3): p. 583-600.
141. Bukowiecki, L., et al., *Beta-adrenergic receptors in brown-adipose tissue: characterization and alternation during acclimation of rats to cold*. *European Journal of Biochemistry*, 1978. **92**: p. 189-196.
142. Chaudhry, A. and J.G. Granneman, *Differential regulation of functional responses by beta-adrenergic receptor subtypes in brown adipocytes*. *Am J Physiol*, 1999. **277**(1): p. R147-53.
143. Hilligan, K.L. and F. Ronchese, *Antigen presentation by dendritic cells and their instruction of CD4+ T helper cell responses*. *Cell Mol Immunol*, 2020. **17**(6): p. 587-599.
144. Cheong, C., et al., *Microbial stimulation fully differentiates monocytes to DC-SIGN/CD209(+) dendritic cells for immune T cell areas*. *Cell*, 2010. **143**(3): p. 416-29.
145. Förster, R., A.C. Davalos-Miszlitz, and A. Rot, *CCR7 and its ligands: balancing immunity and tolerance*. *Nat Rev Immunol*, 2008. **8**(5): p. 362-71.
146. Takekoshi, T., et al., *Identification of a novel marker for dendritic cell maturation, mouse transmembrane protein 123*. *J Biol Chem*, 2010. **285**(41): p. 31876-84.
147. Rodrigues, P.F., et al., *Distinct progenitor lineages contribute to the heterogeneity of plasmacytoid dendritic cells*. *Nat Immunol*, 2018. **19**(7): p. 711-722.
148. Jaitin, D.A., et al., *Lipid-Associated Macrophages Control Metabolic Homeostasis in a Trem2-Dependent Manner*. *Cell*, 2019. **178**(3): p. 686-698.e14.

149. Lee, Y.H. and J.G. Granneman, *Seeking the source of adipocytes in adult white adipose tissues*. *Adipocyte*, 2012. **1**(4): p. 230-236.
150. Murano, I., et al., *Time course of histomorphological changes in adipose tissue upon acute lipoatrophy*. *Nutr Metab Cardiovasc Dis*, 2013. **23**(8): p. 723-31.
151. Gougoula, C., et al., *Metabolic and behavioral parameters of mice with reduced expression of Syndecan-1*. *PLoS One*, 2019. **14**(7): p. e0219604.
152. Yu, C., et al., *Syndecan-1 Facilitates the Human Mesenchymal Stem Cell Osteo-Adipogenic Balance*. *Int J Mol Sci*, 2020. **21**(11).
153. Zaragosi, L.E., et al., *Syndecan-1 regulates adipogenesis: new insights in dedifferentiated liposarcoma tumorigenesis*. *Carcinogenesis*, 2015. **36**(1): p. 32-40.
154. Taylor, S.R., M.G. Markesbery, and P.A. Harding, *Heparin-binding epidermal growth factor-like growth factor (HB-EGF) and proteolytic processing by a disintegrin and metalloproteinases (ADAM): A regulator of several pathways*. *Seminars in Cell & Developmental Biology*, 2014. **28**: p. 22-30.
155. Loechel, F., et al., *ADAM 12-S cleaves IGFBP-3 and IGFBP-5 and is inhibited by TIMP-3*. *Biochem Biophys Res Commun*, 2000. **278**(3): p. 511-5.
156. Coles, C.A., et al., *Knockdown of a disintegrin A metalloprotease 12 (ADAM12) during adipogenesis reduces cell numbers, delays differentiation, and increases lipid accumulation in 3T3-L1 cells*. *Mol Biol Cell*, 2018. **29**(15): p. 1839-1855.
157. Boring, L., et al., *Impaired monocyte migration and reduced type 1 (Th1) cytokine responses in C-C chemokine receptor 2 knockout mice*. *J Clin Invest*, 1997. **100**(10): p. 2552-61.

158. Braga, T.T., et al., *CCR2 contributes to the recruitment of monocytes and leads to kidney inflammation and fibrosis development*. *Inflammopharmacology*, 2018. **26**(2): p. 403-411.
159. Willenborg, S., et al., *CCR2 recruits an inflammatory macrophage subpopulation critical for angiogenesis in tissue repair*. *Blood*, 2012. **120**(3): p. 613-25.
160. Buch, T., et al., *A Cre-inducible diphtheria toxin receptor mediates cell lineage ablation after toxin administration*. *Nat Methods*, 2005. **2**(6): p. 419-26.
161. Ruedl, C. and S. Jung, *DTR-mediated conditional cell ablation-Progress and challenges*. *Eur J Immunol*, 2018. **48**(7): p. 1114-1119.
162. Saito, M., et al., *Diphtheria toxin receptor-mediated conditional and targeted cell ablation in transgenic mice*. *Nat Biotechnol*, 2001. **19**(8): p. 746-50.
163. Klueh, U., et al., *Impact of macrophage deficiency and depletion on continuous glucose monitoring in vivo*. *Biomaterials*, 2014. **35**(6): p. 1789-1796.
164. Bu, L., et al., *Intraperitoneal injection of clodronate liposomes eliminates visceral adipose macrophages and blocks high-fat diet-induced weight gain and development of insulin resistance*. *Aaps j*, 2013. **15**(4): p. 1001-11.
165. Feng, B., et al., *Clodronate liposomes improve metabolic profile and reduce visceral adipose macrophage content in diet-induced obese mice*. *PLoS One*, 2011. **6**(9): p. e24358.
166. Machida, K., et al., *Role of macrophages in depot-dependent browning of white adipose tissue*. *J Physiol Sci*, 2018. **68**(5): p. 601-608.



167. Sakamoto, T., et al., *Macrophage infiltration into obese adipose tissues suppresses the induction of UCP1 level in mice*. Am J Physiol Endocrinol Metab, 2016. **310**(8): p. E676-e687.
168. Bergh, A., J.E. Damber, and N. van Rooijen, *Liposome-mediated macrophage depletion: an experimental approach to study the role of testicular macrophages in the rat*. J Endocrinol, 1993. **136**(3): p. 407-13.
169. Blom, A.B., et al., *Synovial lining macrophages mediate osteophyte formation during experimental osteoarthritis*. Osteoarthritis Cartilage, 2004. **12**(8): p. 627-35.
170. Polfliet, M.M., et al., *A method for the selective depletion of perivascular and meningeal macrophages in the central nervous system*. J Neuroimmunol, 2001. **116**(2): p. 188-95.
171. Thepen, T., N. Van Rooijen, and G. Kraal, *Alveolar macrophage elimination in vivo is associated with an increase in pulmonary immune response in mice*. J Exp Med, 1989. **170**(2): p. 499-509.
172. Sárvári, A.K., et al., *Plasticity of Epididymal Adipose Tissue in Response to Diet-Induced Obesity at Single-Nucleus Resolution*. Cell Metab, 2021. **33**(2): p. 437-453.e5.
173. Emont, M.P., et al., *A single-cell atlas of human and mouse white adipose tissue*. Nature, 2022. **603**(7903): p. 926-933.
174. Rondini, E.A., et al., *Single cell functional genomics reveals plasticity of subcutaneous white adipose tissue (WAT) during early postnatal development*. Mol Metab, 2021. **53**: p. 101307.

175. Song, A., et al., *Low- and high-thermogenic brown adipocyte subpopulations coexist in murine adipose tissue*. J Clin Invest, 2020. **130**(1): p. 247-257.
176. Schaum, N., et al., *Single-cell transcriptomics of 20 mouse organs creates a Tabula Muris*. Nature, 2018. **562**(7727): p. 367-372.
177. Kaikaew, K., et al., *Sex difference in the mouse BAT transcriptome reveals a role of progesterone*. Journal of Molecular Endocrinology, 2021. **66**(2): p. 97-113.
178. Dou, Z.F., et al., *Ameliorative effects of glycine in an experimental nonalcoholic steatohepatitis and its correlation between TREM-1 and TREM-2*. Am J Transl Res, 2016. **8**(2): p. 284-97.
179. Hou, J., et al., *TREM2 sustains macrophage-hepatocyte metabolic coordination in nonalcoholic fatty liver disease and sepsis*. J Clin Invest, 2021. **131**(4).
180. Xiong, X., et al., *Landscape of Intercellular Crosstalk in Healthy and NASH Liver Revealed by Single-Cell Secretome Gene Analysis*. Mol Cell, 2019. **75**(3): p. 644-660 e5.
181. Filipello, F., et al., *The Microglial Innate Immune Receptor TREM2 Is Required for Synapse Elimination and Normal Brain Connectivity*. Immunity, 2018. **48**(5): p. 979-991.e8.
182. Hu, M., et al., *High-salt diet downregulates TREM2 expression and blunts efferocytosis of macrophages after acute ischemic stroke*. J Neuroinflammation, 2021. **18**(1): p. 90.
183. Kleinberger, G., et al., *TREM2 mutations implicated in neurodegeneration impair cell surface transport and phagocytosis*. Sci Transl Med, 2014. **6**(243): p. 243ra86.

184. Krasemann, S., et al., *The TREM2-APOE Pathway Drives the Transcriptional Phenotype of Dysfunctional Microglia in Neurodegenerative Diseases*. *Immunity*, 2017. **47**(3): p. 566-581.e9.
185. Nugent, A.A., et al., *TREM2 Regulates Microglial Cholesterol Metabolism upon Chronic Phagocytic Challenge*. *Neuron*, 2020. **105**(5): p. 837-854.e9.
186. Anzai, A., et al., *Regulatory role of dendritic cells in postinfarction healing and left ventricular remodeling*. *Circulation*, 2012. **125**(10): p. 1234-45.
187. Burke, S., et al., *Adipocytes in both brown and white adipose tissue of adult mice are functionally connected via gap junctions: implications for Chagas disease*. *Microbes Infect*, 2014. **16**(11): p. 893-901.
188. Revel, J.P., A.G. Yee, and A.J. Hudspeth, *Gap junctions between electrotonically coupled cells in tissue culture and in brown fat*. *Proc Natl Acad Sci U S A*, 1971. **68**(12): p. 2924-7.
189. Zhu, Y., et al., *Connexin 43 Mediates White Adipose Tissue Beiging by Facilitating the Propagation of Sympathetic Neuronal Signals*. *Cell Metab*, 2016. **24**(3): p. 420-433.
190. Nakamura, Y., et al., *A disintegrin and metalloproteinase 12 prevents heart failure by regulating cardiac hypertrophy and fibrosis*. *Am J Physiol Heart Circ Physiol*, 2020. **318**(2): p. H238-h251.
191. Sun, C., W.L. Berry, and L.E. Olson, *PDGFR $\alpha$  controls the balance of stromal and adipogenic cells during adipose tissue organogenesis*. *Development*, 2017. **144**(1): p. 83-94.

192. Santangelo, C. *Worthington Biochemical Online Tissue Dissociation Guide*. 2011 [cited 2022; Available from: <https://www.worthington-biochem.com/tissuedissociation/basic.html>].
193. Stenn, K.S., et al., *Dispase, a Neutral Protease From Bacillus Polymyxa, Is a Powerful Fibronectinase and Type IV Collagenase*. *Journal of Investigative Dermatology*, 1989. **93**(2): p. 287-290.
194. Oyler-Yaniv, A., et al., *A Tunable Diffusion-Consumption Mechanism of Cytokine Propagation Enables Plasticity in Cell-to-Cell Communication in the Immune System*. *Immunity*, 2017. **46**(4): p. 609-620.
195. Land, W.G., *The Role of Damage-Associated Molecular Patterns (DAMPs) in Human Diseases: Part II: DAMPs as diagnostics, prognostics and therapeutics in clinical medicine*. *Sultan Qaboos Univ Med J*, 2015. **15**(2): p. e157-70.
196. Wang, X., et al., *Metabolism-Associated Molecular Patterns (MAMPs)*. *Trends Endocrinol Metab*, 2020. **31**(10): p. 712-724.
197. Weismann, D. and C.J. Binder, *The innate immune response to products of phospholipid peroxidation*. *Biochim Biophys Acta*, 2012. **1818**(10): p. 2465-75.
198. Bergenstr hle, J., L. Larsson, and J. Lundeberg, *Seamless integration of image and molecular analysis for spatial transcriptomics workflows*. *BMC Genomics*, 2020. **21**(1): p. 482.
199. Cho, C.S., et al., *Microscopic examination of spatial transcriptome using Seq-Scope*. *Cell*, 2021. **184**(13): p. 3559-3572.e22.
200. Rao, A., et al., *Exploring tissue architecture using spatial transcriptomics*. *Nature*, 2021. **596**(7871): p. 211-220.

201. Dries, R., et al., *Advances in spatial transcriptomic data analysis*. *Genome Res*, 2021. **31**(10): p. 1706-1718.
202. Zeng, Z., et al., *Statistical and machine learning methods for spatially resolved transcriptomics data analysis*. *Genome Biology*, 2022. **23**(1): p. 83.

**ABSTRACT****DECONSTRUCTING BROWN ADIPOCYTE NEOGENESIS IN WHITE AND BROWN ADIPOSE TISSUE**

by

**RAYANNE B. BURL****August 2022****Advisor:** Dr. James Granneman**Major:** Molecular Genetics and Genomics**Degree:** Doctor of Philosophy

Global incidence of Type 2 Diabetes (T2D) has reached epidemic proportions, and increasing evidence indicates that dysfunctional adipose tissue is an important contributor to the pathogenesis of T2D. Expanding brown adipocyte (BA) populations within adipose tissues through adrenergic activation improves energy balance and insulin sensitivity. In order to exploit this remodeling of adipose tissue for therapeutic benefit, we need to understand the mechanisms by which adrenergic signaling expand populations of BAs *in vivo*. These studies utilized single-cell RNA-sequencing and transgenic mouse models, in combination with single-molecule fluorescence *in situ* hybridization (smFISH) and immunohistochemical analysis, to study BA neogenesis *in vivo*. scRNA-seq identified distinct PDGFRA<sup>+</sup> adipocyte progenitor subpopulations in all adipose depots that appeared to be differentially poised to enter the adipogenic pathway. These progenitor subtypes occupy distinct tissue locations.  $\beta$ 3-adrenergic receptor (ADRB3) activation triggered the dramatic appearance of proliferating ASCs in mouse epididymal white adipose tissue (eWAT), whose differentiation into BAs could be inferred from a single time point. scRNA-seq identified various immune cell types in eWAT, including a proliferating

macrophage subpopulation that occupies adipogenic niches. In interscapular brown adipose tissue (iBAT), knockout of the  $\beta$ 1-adrenergic receptor (ADRB1) in progenitors did not prevent cold-induced neogenesis. However, pharmacological activation of the ADRB3 on BAs was sufficient to induce neogenesis, suggesting that signals derived from mature BAs indirectly trigger ASC proliferation and differentiation in iBAT as in eWAT. In this regard, cold exposure induced the delayed appearance of multiple macrophage and dendritic cell populations in iBAT whose recruitment strongly correlated with the onset and magnitude of neogenesis across diverse experimental conditions. High resolution immunofluorescence and smFISH demonstrated that cold-induced neogenesis involves dynamic interactions between progenitor subtype ASC1 and recruited immune cells that occur on the micrometer scale in distinct tissue regions. Finally, we acknowledge that tissue digestion method can alter cells captured with scRNA-seq and therefore confound results. It is therefore critical to validate results from scRNA-seq in the intact tissue. This work provides unbiased profiling of BA neogenesis in multiple adipose tissues at the single-cell level, and demonstrates a framework for validating single-cell results with smFISH and immunohistochemistry.

## AUTOBIOGRAPHICAL STATEMENT

**RAYANNE B. BURL**

### EDUCATION

**Wayne State University School of Medicine** Detroit, MI USA  
 Doctor of Philosophy (Molecular Genetics and Genomics) 08/2015 - Present  
 Center for Molecular Medicine and Genetics  
 Mentor: Dr. James Granneman GPA: 4.0

**Kalamazoo College** Kalamazoo, MI USA  
 Bachelor of Arts Major: Biology 08/2009 – 06/2013  
 Senior Individualized Project: Optimizing the Treatment Method of Arterial Tissue to be Used as Acellular Scaffold for Vascular Reconstruction

### SELECTED PUBLICATIONS

1. **RB Burl**, EA Rondini, H Wei, R Pique-Regi, and JG Granneman. *Deconstructing cold-induced brown adipocyte neogenesis in mice.* **eLife**. Jul 2022; 11:e80167.
2. **RB Burl**, VD Ramseyer, EA Rondini, R Pique-Regi, and JG Granneman. *Deconstructing adipogenesis induced by  $\beta$ 3-Adrenergic receptor activation with single-cell expression profiling.* **Cell Metab.** Aug 2018; 28(2), 300-309.
3. EA Rondini, VD Ramseyer, **RB Burl**, R Pique-Regi, and JG Granneman. *Single cell functional genomics reveals plasticity of subcutaneous white adipose tissue (WAT) during early postnatal development.* **Mol Metab.** Jul 2021; 53:101307.
4. Y Son, C Choi, A Saha, JH Park, H Im, YK Cho, JK Seong, **RB Burl**, EA Rondini, JG Granneman, and YH Lee. *Reep6 knockout leads to defective  $\beta$ -adrenergic signaling in adipocytes and promotes obesity-related metabolic dysfunction.* **Metab.: Clin. Exp.** Feb 2022; 130:155159.
5. Y Son, YK Cho, A Saha, HJ Kwon, JH Park, M Kim, YS Jung, SN Kim, C Choi, JK Seong, **RB Burl**, JG Granneman, and YH Lee. *Adipocyte-specific Beclin1 deletion impairs lipolysis and mitochondrial integrity in adipose tissue.* **Mol Metab.** Sep 2020; 39:101005.

### FELLOWSHIP

NIH F31 Fellowship - NIDDK  
 Grant Number: F31DK116536-01A1  
 Award Period: March 2018 – March 2021  
 Title: Deconstructing the brown neogenic zone in classic brown adipose tissue.

### ACCOLADES

May 2018. Wayne State Lipids@wayne Symposium – First Place, Poster Presentation.  
 September 2019. Wayne State Genomics@wayne Symposium – Top 3 Poster Presentation.  
 October 2019. Wayne State Graduate Student Research Day – Second Place, Oral Presentation  
 Recipient – Wayne State OVPR Genomics Voucher Program.